DOI: 10.17277/issn.2414-4606

ISSN 2414-4606
e-ISSN 2541-8513

Advanced Materials & Technologies

No. 3
2018

Tambov State Technical University

Merzhanov Institute of Structural Macrokinetics and Materials Sciences of RAS

CONTENTS

Established in 2016
Issued quarterly

ADVANCED MATERIALS & TECHNOLOGIES
Scientific and Theoretical Journal

The Publisher: Tambov State Technical University, Tambov, Russia
Merzhanov Institute of Structural Macrokinetics and Materials Sciences of Russian Academy of Sciences, Scientific Center in Chernogolovka, Moscow, Russia

The Authors are expected to be aware of, and comply with, best practice in publication ethics.
The Publisher has the Authors' permission to publish the works both in printed and electronic versions of the journal.

By the Resolution of the Presidium of the Higher Attestation Commission of the Ministry of Education and Science of the Russian Federation, AM&T journal has been included in the list of leading peer-reviewed scientific journals and publications to publish main scientific results of dissertations for candidate and doctorate degrees.

The journal is indexed in Chemical Abstract; Russian Index of Scientific Citation; Google Scholar (Google Academy)
Subscription is available on the territory of Russian Federation. "Rospechat" index 80453

Editorial Board
Advanced Materials & Technologies

Editorial staff: N.A. Gunina
Computer design by: O.V. Mochalina

Format 60x90 / 8. Offset paper. Printed sheets 11.25. Published sheets 13.04.
Signed to print 2018.07.31. Number of copies 100. Order 214.
Editorial office tel.: +7 (4752) 63 78 15. Address: 106 Sovetskaya, Tambov, 392000, Russia
Http://journal.tstu.ru. E-mail: amt@amt.tstu.ru

Production of New Materials Using Explosion Energy and Self-Propagating High-Temperature Synthesis

From 14 to 18 May 2018 St. Petersburg hosted the 14th International Symposium on the Explosive Production of New Materials: Science, Technology, Business and Innovation (EPNM-2018).

The symposium was organized by the A.G. Merzhanov Institute of Science Institute of Structural Macrokinetics and Materials Science of Russian Academy of Sciences (ISMAN, Chernogolovka) and Energometall AO (St. Petersburg) with the support of the Russian Foundation for Basic Research (Project 18-08-20027) and the Division of Chemistry and Materials Science of the Russian Academy of Sciences.

More than 120 specialists from Russia, Portugal, Poland, Germany, France, Netherlands, Ukraine, Czech Republic, Slovakia, Armenia, Estonia, USA, Brazil, China and Japan took part in the EPNM-2018.

Based on the results of the materials presented, a collection of materials was prepared for the International Symposium "EPNM-2018" – Proceedings of the XIV International Symposium on Explosive Production of New Materials: Science, Technology, Business, and Innovations [Edited by M. I. Alymov, O. A. Golosova]. Moscow: TORUS PRESS, 2018. 362 p. ISBN 978-5-94588-230-0. At the Symposium, 84 reports were presented, including 46 oral presentations and 38 poster presentations.

At the opening ceremony, the co-chairmen of the Organizing Committee, the ISMAN Director, Corresponding Member of the Russian Academy of Sciences M.I. Alymov addressed the attendees of the Symposium with a welcome speech. Prof. J. Banker (USA), Professor Ricardo Mendes (Portugal), Dr. Zygmunt Szulc (Poland), and others also spoke at the opening ceremony.

The plenary speech of M.I. Alymov covered the results of the research conducted at the institute on explosion welding, self-propagating high-temperature synthesis and electrothermal explosion. The President of Clad Metal Consulting, J. Banker presented the analysis of the formation and development of metalworking by the explosion in the world. He concluded explosive punching failed to compete with other metal-shaping technologies and ceased to exist, while explosion welding firmly holds its niche in commercial production with a global annual volume of about 1 billion US dollars. According to J. Banker, it is necessary to constantly search for new areas of application of this technology. V.S. Vakin presented a detailed report of the 10th practice of explosion welding work at Energometall AO, gave examples of successful cooperation in the manufacture of commercial products, in particular, the company manufactured bimetal for the International Experimental Fusion Reactor under construction at the Cadarache Research Center in the south of France (ITER project).

All reports on recent work in the field of processing and synthesis of materials with the use of explosion and high-temperature synthesis, presented at the symposium, were interesting and informative. For example, A.A. Shterzer (co-authors A.A. Deribas, E.E. Zubkov) described another "explosion" technology – explosive hardening, which is successfully used in the commercial production of railroad switch frogs. The representative of the Research Center "Kurchatov Institute" – CNII KM "Prometey" – I.A. Schastlivaya presented in detail the results of many years of research into the mechanism and growth of defects in bimetallic materials (steel/titanium), depending on the ongoing technological operations and types of loading.

A detailed plenary report on the latest achievements of fundamental and applied science in the field of superplasticity and intensive plastic deformation of high-temperature metallic materials for the production of complex profile products used in the aerospace and aviation industries was made by Corresponding Member of the Russian Academy of Sciences, Director of the Institute of Metal Superplasticity Problems, RAS R. R. Mulyukov.

All reports made by the Symposium speakers are of interest to researchers, engineers and businessmen working in the field of producing new materials by high-energy techniques. It should be noted that in recent years active research on aluminum-steel explosive welding using emulsion explosives and ANFO (mixture of ammonium nitrate with diesel fuel) has been conducted at the University of Coimbra in Portugal (R. Mendes, I. Galvao, G. Carvalho and other). As for the ANFO, the experiments important for practical applications conducted by V. Petr from the Colorado School of Mines (USA) found a significant effect of the density of ammonium nitrate particles on the detonation rate of this explosive. Serious progress has been achieved by the scientists of the Beijing Institute of Technology (Institute of Technology,

Beiling, China) under the leadership of Professor P. Chen. For example, the report presented by Q. Zhou describes interesting results on the synthesis of multi-layer graphene (a few-layer grapheme) by shock wave method, and H. Yin described the preparation of iron nanoparticles in a carbon shell by blasting an explosive mixture with iron tristearate in evacuated vacuum chamber. The studies on the shock wave loading of tungsten carbide in the megabar range conducted by T. Schlotauer from the Technical University of the Freiberg University of Engineering showed a WC → W_2C + diamond transition. The reports made by L. Kecskes from Matsys Inc. Sterling (USA) about the studies carried out jointly with researchers from Georgia (A.B. Peikrishvili, E.Sh. Chagelishvili, G.F. Tavadze, B.A. Godibadze and others) were informative. To produce compacts from high-strength materials, they use the effective method of Hot-Explosive Consolidation (HEC). In Ta–Al, Nb–Al and V–Al powder mixtures, due to high-temperature heating above the start-up temperature of self-propagating high-temperature synthesis (≥ 940 °C for Ta–Al), blasting occurs in the liquid-phase state of the SHS product. The HEC method also produced low-porosity compacts from nanosized W–Ag, W–Cu, W–Ta powder mixtures.

A number of reports were devoted to the study of the high-speed collision of materials, the study of the bond zone in bimetals and the study of the synthesis process using the most modern methods, instruments and equipment. The Japanese researcher A. Mori from Sojo University presented optical images of shaped jets that occur under oblique collision of plates from dissimilar materials. It is characteristic that when copper collides with the AZ31 magnesium alloy, the alloy particles, of which the jet consists, ignite when interacting with air. H. Paul, from the Institute of Metallurgy and Materials Science of the Polish Academy of Sciences studied the zone of connection of various metal pairs (steel / titanium (Gr. 5), steel/ zirconium alloy Zr700, titanium (Gr. 1) / copper, etc.) with the help of transmission electron microscopy and scanning electron microscopy (TEM and SEM) and concluded that there is always a very thin layer of melt in the contact zone. K. Saksl from the Institute of Materials Science of the Slovak Academy of Sciences reported on a new method for the diagnosis of residual stresses in bimetal – a two-dimensional X-ray diffraction method with a synchrotron source and with a focal spot size of 20 μm. With the use of the same synchrotron radiation, in the time-lapse photography mode with a picoseconds exposure, K. Ten from Lavrentyev Institute of Hydrodynamics SB RAS and his colleagues from other institutes of the SB RAS managed to fix the formation and growth of nanodiamonds in a detonation wave.

It should be noted that, in comparison with previous events, the symposium theme expanded and the interdisciplinary nature of the presented studies was very impressive, which was noted at the closing ceremony of the symposium by the speakers. The program of special interest sessions, which was devoted to the results of research in the field of self-propagating high-temperature synthesis, included reports on the theory and modeling of combustion processes, the synthesis of functional and structural materials, protective coatings, layered composite materials, powder materials, as well as the study of new hybrid processes combining SHS and subsequent processing of the produced materials.

Professor A.M. Stolin (ISMAN) presented a report describing the new technological approach and the latest results obtained using the method of free SHS-pressing. The first samples of ceramic plates with dimensions over 100 mm, made from a titanium diboride-based material were demonstrated. S.V. Karpov (Tambov State Technical University) spoke about modern approaches to mathematical modeling of complex non-stationary heat transfer processes in the free compression of hot SHS products.

Several presentations were devoted to the study of the laws of high-temperature synthesis of the so-called ultra-high temperature materials. Professor V.I. Yukhvid (ISMAN) showed wide possibilities of using the SHS-metallurgy method for producing materials based on molybdenum silicide, used as a basis for products capable of operating in oxidizing environment at temperatures higher than 2000 °C. A.Yu. Potanin, the young researcher from MISiS presented the results of the studies on high-temperature synthesis of ultra-high-temperature materials based on ZrB_2, doped with SiC, $MoSi_2$, and HfB_2 in demand for the manufacture of critical products for hypersonic aircraft. Professor V.A. Sherbakov (ISMAN) in his report spoke about important, practically significant results on obtaining dense ultra-high-temperature ceramics based on complex Ta_4ZrC_5–CrB and Ta_4HfC_5–CrB systems.

Traditionally, a significant amount of studies was devoted to SHS materials based on intermetallic compounds. Professor A.G. Knyazeva (Tomsk State University) presented a detailed report on the results of mathematical modeling of high-temperature interaction processes in the synthesis of materials based on the Ti–Al system. A.E. Sychev (ISMAN) made an interesting report on the synthesis of nickel aluminide

with a modifying carbon additive. It was found that platelet (graphene-like) carbon emissions along grain boundaries of the intermetallic compound promote an increase in ductility while maintaining strength. The young scientist E.I. Patsera (the MISiS University) presented the results on the synthesis of microgranules from promising intermetallic CompoNiAl-M_5 alloy for the formation of products of complex shape by using additive 3D-technologies. One can note an interesting report made by the young researcher A.V. Sobachkina (Altai State Technical University), who showed that the gamma-ray treatment of a mechanically activated mixture of Ti + Al powders increases the homogeneity of the TiAl product made by the SHS method and its stability under long-term high-temperature annealing conditions.

At the symposium, a number of reports were presented on the consolidation of porous materials using spark plasma sintering (**SPS**), including in combination with other methods of action on the substance. Thus, the researchers from Armenia and Estonia – S. Aydinyan and T. Minasyan – made interesting reports on the sintering of ZrC+TiC+$MoSi_2$ ceramics and consolidation of Mo+Cu nanopowder by the SPS. Professor E.G. Grigoriev (National Research Nuclear University "MEPhI") presented a comprehensive report on consolidation using high-voltage electric pulses for the production of thin rings of soft magnetic alloy 49K2FA.

V.N. Sanin (ISMAN) presented a report on solving environmental problems through the disposal of man-made waste generated during high-temperature metalworking (rolling, punching, etc.). The possibility of commercial realization of the SHS method for a wide range of cast, complex-alloyed ferroalloys of various practical applications was shown.

At the EPNM-2018 symposium, a competition for the best study of young researchers was held; the International Advisory Committee selected the winners. Three specialists, a researcher from Armenia, Sofiya Aydinyan, (Tallinn Technical University), Sergey Karpov (Tambov State Technical University) and Amadeusz Kurek (Explomet, Poland) won the 3rd prize. The 2nd prize was awarded to Gustavo Carvalho (University of Coimbra, Portugal) and Sheng Zemin (Beijing Institute of Technology, PRC). The 1st prize was awarded to the young researcher Ivan Batayev (Novosibirsk State Technical University). All the winners were awarded memorable souvenir plates with views of St. Petersburg.

Some of the international participants of the Symposium came to Russia for the first time. The organizers provided an exciting social program, with a tour of St. Petersburg, a magnificent city on the Neva. For the participants of EPNM-2018, a boat trip along the Neva with an exit to the Gulf of Finland was organized. The attendees admired the beautiful views of St. Petersburg, took lovely photos and learned

some of the history of St. Petersburg, one of the best cities and the cultural capital of Russia. An excursion to Petergof with a walk along the Upper and Lower Parks, a visit to the grottoes, as well as an excursion to the Grand Palace, which impressed everyone with its splendor, were organized. Peterhof, which is often called the Russian Versailles, proved to be even more exciting than one would expect. After the excursion to Petergof, the participants of the EPNM-2018 attended a master class on matryoshka painting organized in the village of Shuvalovka (the Russian style village). Within an hour more than a hundred people – venerable doctors of science, professors, and young researchers painted their personal matryoshka, with all their diligence and mastery, while listening to the story of the creation of the world-famous Russian doll.

At the closing ceremony, many of the speakers noted the high level of the organization of the event, the warm and friendly atmosphere and the opportunity to communicate, to sum up the results of the studies conducted in the recent period and to outline joint research plans for the future. It was noted that participation of your researchers in such international events is of particular importance. It helps to get talented young researchers involved in promising international scientific research and projects.

Summing up the results of the 14th International Symposium on Explosive Production of New Materials: Science, Technology, Business and Innovation (EPNM-2018), it was emphasized that the methods of processing and synthesizing materials using explosion and high-temperature synthesis are unique inventions of Russian scientists and despite years of research there is still a great scientific and practical potential for future studies aimed at creating new materials with unique properties, which are in great demand for new engineering equipment.

M.I. Alymov
A. A. Shtertser
V.N. Sanin
O.O. Likhanova

Please, visit our website to find out more about the program and have a look at the Proceedings of the symposium:

http://www.ism.ac.ru/events/EPNM2018/scientific-program-ru.html

DOI: 10.17277/amt.2018.03.pp.007-009

Thermodynamic Scale of Dispersive Capacity of Crystalline Bodies

Yu.V. Levinsky[1], M.I. Alymov[1,2]*

[1] *Merzhanov Institute of Structural Macrokinetics and Materials Science, Russian Academy of Sciences, 8, Academician Osipyan St., Chernogolovka, Moscow Region, 142432, Russia;*
[2] *Baikov Institute of Metallurgy and Materials Science of RAS, 49, Leninsky Pr., Moscow, 119334, Russia*

* Corresponding author. Tel.: +7 496 52 46 376. *E-mail*: alymov@ism.ac.ru

Abstract

It is assumed that most of the excess free energy of a dispersed system is its excess free surface energy, and the excess free energy of a compact body is the free energy determined by the density of dislocations of 10^{12} cm^{-2}. A dimensionless thermodynamic criterion for the dispersion of crystalline solids D_L is proposed to be considered as a unit of measurement. A thermodynamic scale of dispersity of crystalline bodies is proposed.

Keywords

Scale of measurement; dispersity; particle size; defects; thermodynamic properties; free energy.

Introduction

The nature and the result of physical-chemical processes are determined by dimensionless criteria composed of dimensional parameters describing the phenomenon under consideration. In hydrodynamics, the Reynolds number, which determines the transition of a laminar flow type to a turbulent flow, plays the most important role. In macrokinetics of isothermal transformation, the key value is the Semenov number, which separates the slow and explosive course of the reaction. The Pilling-Bedward criterion is used to characterize the protective properties of an oxide film.

Disperse systems have a number of characteristic properties that determine their behavior, different from compact bodies, in many chemical and physical processes. Although the particle size is based on this phenomenon, it is convenient to measure the degree of this difference by relative units, normalizing the properties of the disperse system to the properties of a compact one. As a standard comparison state for a compact system, one should choose one in which it has the maximum possible value of the properties being compared under the given conditions. The aim of the paper is to show that dispersive capacity as a property of a system can be measured by numerical values of dimensionless criteria characterizing the degree of difference in specific properties of dispersed and compact bodies.

Results and discussion

We consider the thermodynamic properties of crystalline bodies. The main components of the excess free energy of these bodies are defects of the crystal lattice and surface energy. In a compact body, the ratio of the surface to the mass is small and the value of the surface energy for it can be neglected. Then the standard state of a crystalline compact body can be take its state with the maximum defectiveness of the crystal lattice, which can be characterized by the maximum dislocation density $\rho = 10^{12}$ cm^{-2}. The dislocation density is the total length of the dislocation lines per unit volume of the crystal, i.e. the dislocation density has a dimension of cm/cm^3. The energy per unit dislocation length is equal to $0.5Gb^2$, therefore the maximum excess free energy of a compact crystalline body ΔG_V with a volume V will be equal to:

$$\Delta G_V = 0.5\mu b^2 \rho V , \quad (1)$$

where μ is shear modulus, b is Burgers vector, V is body volume.

If we assume that the maximum distortions of the crystal lattice of dispersed particles and compact bodies are approximately equal, the excess free energy of the dispersed particles is equal to:

$$\Delta G_L = \Delta G_V + \Delta G_S = \Delta G_V + \sigma S\,, \qquad (2)$$

where ΔG_S is excess free surface energy, σ is specific surface energy, S is the surface of all particles occupying the volume V.

If we assume that the dispersed system is a collection of monodisperse spherical particles of diameter L, then

$$S = 6V/L\,.$$

Since it is proposed to normalize the excess free energy of dispersed bodies with respect to the energy of maximally deformed compact bodies, then

$$\frac{\Delta G_L}{\Delta G_V} = \frac{\Delta G_S + \Delta G_V}{\Delta G_V} = \frac{\Delta G_S}{\Delta G_V} + 1 = \frac{12\sigma}{Gb^2 L\rho} + 1\,. \qquad (3)$$

The discussion of the excess free energy of dispersed systems becomes meaningful when it is several times greater than the free energy of compact bodies. Therefore

$$\frac{\Delta G_L}{\Delta G_V} \approx \frac{12\sigma}{Gb^2 L\rho}\,. \qquad (4)$$

In [1–3] The particle size satisfying equality (4) was suggested to be called critical L_{KP}, and the relation

$$\frac{12\sigma}{Gb^2 L\rho} = D_L \qquad (5)$$

to be called dimensionless thermodynamic criterion for the dispersion of critical bodies D_L.

Values of physical properties required for calculation ΔG_S, ΔG_V and L_{KP} of certain metals are given in Table 1.

From Table 1 it follows that, although for all metals $D_L = 1$ corresponds to the particle size (500 ± 250) nm, deviations from the mean value can still be a subject for discussion in determining the difference in the thermodynamic properties of particles of different metals having the same dimensions. These differences can be even greater if we compare the thermodynamic properties of dispersed particles with different types of chemical bonds (metallic, covalent, ionic).

Thus, the thermodynamic properties of dispersed systems are determined not only by the particle size, but also by other physical properties that determine the value D_L. In connection with this, it is advisable to adopt a scale for measuring the thermodynamic properties of dispersed systems, based not on the particle size, but on the value D_L, i.e. by normalizing these properties to a state in which they are the same for compact and dispersed systems. With this approach, it is possible to regulate the value of the thermodynamic properties of dispersed systems by choosing the particle size as the only controlled quantity that makes up D_L, but it is more appropriate to measure the level of change of these properties and to conduct their comparative analysis using the criterion D_L.

It is possible to classify dispersed systems simultaneously by thermodynamic properties, and by the sizes of particles. This is convenient since the boundaries of all four proposed classes roughly coincide, although such a coincidence is not necessary.

The discrepancy in the determination of the dispersive capacity in these two approaches can be demonstrated by the example of dispersed copper and silver particles of the same size. For copper particles with a size of 50 nm, the dispersive capacity $D_L = 7.9$, and for silver particles $D_L = 9.0$ (see Table 1). That is, when the particle sizes are equal in this scale, the silver dispersion is 12 % higher than the copper dispersion, and this discrepancy is independent of the particle size.

This approach can be extended to a comparison of the dispersion of compact bodies with nanoscale elements of the structure. In this case, in formulas (2) – (5), the value of the surface energy at the solid-vacuum interface should be replaced by the surface energy of the boundaries of the elements of the structure.

The proposed classification seems to be relevant and useful, especially if we take into account the intensive development of nanotechnology and nanomaterials in recent times. In the same connection, it is noteworthy that it is expedient to extend the proposed approach to normalizing the properties of nanomaterials to the properties of compact bodies without nanostructural components to a wider range of materials. In particular, the properties of optical, acoustic, semiconductor nanomaterials should be normalized to the properties of materials determined by the wavelengths of the de Broglie wavelengths of characteristic processes; magnetic nanomaterials – to the properties of materials with a certain value of domains or domain walls, etc.

Table 1

Properties of metals and calculated values ΔG_S, ΔG_V and L_{KP} [1, 4, 5]

Metal	Shear modulus, $G \cdot 10^4$, MPa	Burgers vector b, nm	Surface energy, MJ/m^2	Molar volume V, cm^3/mol	ΔG_V, J/mol ($\rho = 10^{12}$ cm^{-2})	ΔG_S, J/mol (L = 500 nm)	L_{KP}, nm ($\rho = 10^{12}$ cm^{-2})
Cu	4.85	0.256	1115	7.11	120	95	420
Ag	3.00	0.289	945	10.27	128	116	712
Au	2.78	0.288	1230	10.20	118	150	640
Mg	1.75	0.321	728	14.00	252	122	484
Ca	0.76	0.394	386	26.20	117	121	392
Al	2.70	0.286	1040	10.00	110	168	564
Ti	3.96	0.295	1744	10.63	183	184	514
Zr	3.60	0.323	1498	13.97	268	251	478
Hf	5.10	0.321	1553	13.47	353	251	354
V	4.66	0.263	1627	8.36	135	163	604
Nb	3.75	0.286	1927	10.76	165	249	753
Ta	6.85	0.286	2388	10.90	305	312	506
Cr	7.40	0.250	1591	7.23	167	138	412
Mo	12.8	0.272	2240	9.39	444	252	282
W	16.0	0.274	2790	9.54	573	319	277
Fe	8.30	0.248	1624	7.09	181	138	379
Co	8.15	0.251	1445	6.70	172	116	340
Ni	7.45	0.249	1440	6.60	152	114	374

Conclusions

It has been shown that dispersive capacity as a property of a system can be measured by numerical values of dimensionless criteria characterizing the degree of difference of specific properties of dispersed and compact bodies.

A new scale for measuring the dispersive capacity of crystalline bodies is proposed. The scale is based on the normalization of thermodynamic properties determined by the excess free energy, dispersed system to the properties of a compact system that does not contain nanoscale structural elements. As the standard state of the latter, the state of maximum saturation with defects in the crystal lattice has been chosen.

This work was conducted in the framework of State Program for ISMAN (*Research project No. 45.2*).

References

1. Levinsly Yu.V. Odin iz bezrazmernyh kriteriev sovmestimosti pokrytij s metallicheskoj osnovoj [One of the dimensionless compatibility criteria for coatings with a metal substrate]. *Pis'ma v ZhTF*, 2003, vol. 29, issue 5, pp. 49-53. (Rus)

2. Levinsly Yu.V. Eshche raz o termodinamicheskom kriterii dispersnosti [Once again on the thermodynamic criterion of dispersive capacity]. *Materialovedenie,* 2004, issue 3, pp. 55-56. (Rus)

3. Levinsly Yu.V. O termodinamicheski obosnovannom kriterii dispersnosti metallicheskih poroshkov [On the thermodynamically valid criteria for the dispersion of metallic powders]. *Materialovedenie*, 2003, no. 7, pp. 15-17. (Rus)

4. Fridel' Zh. *Dislokacii* [Dislocations]. Moscow: Mir, 1967, 623 p. (Rus)

5. Ragulya A.V., Skorohod V.V. *Konsolidirovannye nanostrukturnye materialy* [Consolidated nanostructured materials]. Kiev. Naukova Dumka, 2007, 374 p. (Rus)

6. Levinsly Yu.V., Lebedev M.P. *Teoreticheskie osnovy processov spekaniya metallicheskih poroshkov*. Moscow, Nauchnyj mir, 2014, 372 p. (Rus)

DOI: 10.17277/amt.2018.03.pp.010-012

SHS Metallurgy of Titanium–Chromium Carbide from $CaCrO_4$ / TiO_2 / Al / C System

P.A. Miloserdov*, V.A. Gorshkov, V.I. Yukhvid, O.M. Miloserdova

Merzhanov Institute of Structural Macrokinetics and Materials Science, Russian Academy of Sciences, ul. Akademika Osip'yana, 8, Chernogolovka, Moscow, 142432 Russia

*Corresponding author: Tel.: +7 (946) 52 46 229. *E-mail*: yu_group@ism.ac.ru

Abstract

Regularities of combustion and autowave chemical transformation of highly exothermic mixtures $CaCrO_4$ / Al / C and $CaCrO_4$ / TiO_2 / Al / Ca / C were studied. It was shown that the mixture could burn over a wide range of concentrations of carbon contained in it; the variation of the mixture composition made it possible to produce cast refractory chromium compounds with different composition and structure. The addition of titanium oxide led to a decrease in the combustion temperature and, accordingly, adversely affected the synthesis parameters and quality of the target product. Highly exothermic additive CaO_2 + Al significantly increased the combustion temperature of the mixture and expanded the limits of combustion and phase separation. The product consisting predominantly of the target phase $Ti_{0.8}Cr_{0.2}C$ and inclusions of Cr_2AlC MAX phase and Cr_7C_3 was obtained.

Keywords

Calcium chromate; carbides; cast materials; combustion synthesis; SHS metallurgy; titanium–chromium carbide.

The creation of new materials with a high level of properties is a key problem of modern technology. In this paper, we study the possibility of obtaining carbide ceramics from mixtures based on calcium chromate $CaCrO_4$ by the SHS metallurgy method. Refractory chromium compounds $Cr_{23}C_6$, Cr_7C_3, and Cr_3C_2 possess useful properties for solving technical problems (high hardness, strength, and resistance to corrosion and wear) and are widely used in practice to create protective coating. Composite materials based on titanium chromium carbide possess higher characteristics than on the basis of individual carbides. The solubility of Cr_3C_2 in TiC at 1700 °C is 30 %. At the chromium carbide content of 30 %, the microhardness of titanium carbide (3000 kg/mm^2) increases to 4000 kg/mm^2 [1–3].

We studied two green mixtures. The overall reaction schemes can be represented in the forms:

$$CaCrO_4 + Al + nC = Cr_xC_y + Al_2O_3 + CaO; \quad (1)$$

$$TiO_2 + (70\ \%\ Al / 30\ \%\ Ca) + C = TiC + Al_2O_3 + CaO. \quad (2)$$

Earlier, we showed in [4] that calcium chromate has the capability to replace chromium oxides (Cr_2O_3 and CrO_3) in mixtures to obtain chromium borides. In the present paper, we used calcium chromate to obtain chromium carbides and titanium–chromium carbide. In the mixture (2), a part of aluminum was replaced by calcium for more complete reduction of TiO_2 [5].

A thermodynamic analysis was carried out using the THERMO program [6]. In the system (1), the carbon content was varied to produce various chromium carbides: $Cr_{23}C_6$, Cr_7C_3 and Cr_3C_2. The analysis showed that the adiabatic temperature of the chemical transformation of the mixture T_{ad} exceeds 3000 K, and the products of the chemical transformation of $CaCrO_4 + 2Al + nC$ mixture at this temperature consist of Cr–Al–C melts ("metallic" phase, the desired product) and Al_2O_3–CaO (oxide phase, slag product), as well as the gas mixture of metal vapors (Al, Cr, Ca), suboxide (Al_2O, Al_2O_2), and CO. An increase in the carbon content in the mixture n from 0 to 3.7 % leads to a decrease in T_{ad} and weight fraction

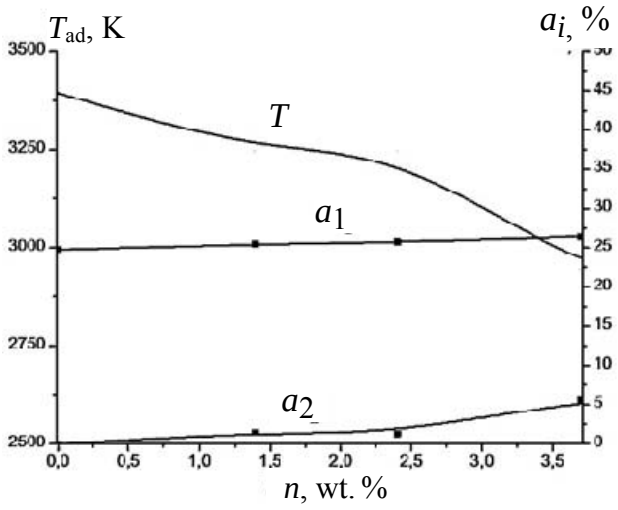

Fig. 1. Influence of the carbon content in the initial mixture on the calculated adiabatic temperature T_{ad} and mass fractions of metallic a_1 and gaseous a_2 chemical conversion products

of the oxide phase and an increase in the content of the metallic and gas phases (Fig. 1).

The experiments on this system showed that within the range n = 0–3.7 %, the mixture retained the ability to burn. Combustion proceeded in the frontal mode with a constant velocity. Combustion products had a molded appearance and were easily divided into two layers: metal (target) and oxide (slag). With an increase in the carbon content in the initial mixture, the burning velocity and relative mass loss decreased during combustion, while the yield of the target product in the ingot increased (Fig. 2).

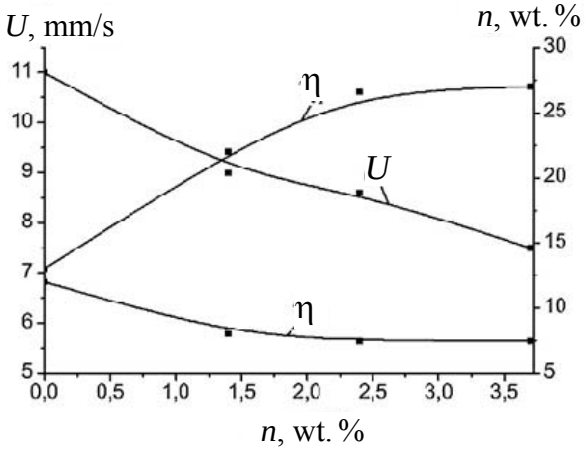

Fig. 2. Burning velocity U, yield of metallic phase η_1, and spread of combustion products (dispersion) η_2 as a function of n
($U = l/t$, where l is the height of the mixture, t is the time of burning; $\eta_1 = m/M_1$, $\eta_2 = [(M_1 - M_2)/M_1]\times 100$ %, M_1 is the mass of the initial mixture, M_2 is the mass of the final combustion products and m is the mass of the metal ingot)

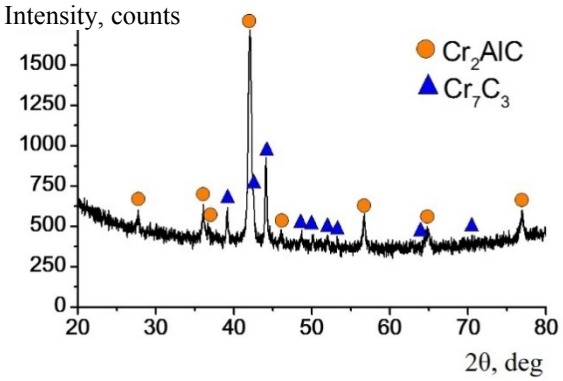

Fig. 3. X-ray diffraction pattern of the product obtained at n = 2.4 %

The results of the analysis show that the target products consist of different chromium carbides including MAX phase Cr_2AlC. At n = 2.4 % (calculated carbon content to prepare Cr_7C_3), Cr_2AlC MAX phase dominates in the product structure that is confirmed by the data of the X-ray diffraction pattern presented in Fig. 3.

To produce titanium–chromium carbide TiC–Cr_3C_2, the content of the mixture (2) α was varied in the mixture (1):

$$\alpha = [M_2/(M_1 + M_2)] \cdot 100\ \%,$$

where M_1 is the mass of the mixture (1), M_2 is the mass of the mixture (2).

The results of the thermodynamic analysis of mixtures, which were calculated from different ratios of mixtures (1) and (2), are shown in Fig. 4. As can be seen, an increase in (α) to 70 % led to a smooth decrease in the combustion temperature. Within the range α = 70–100 %, the combustion temperature

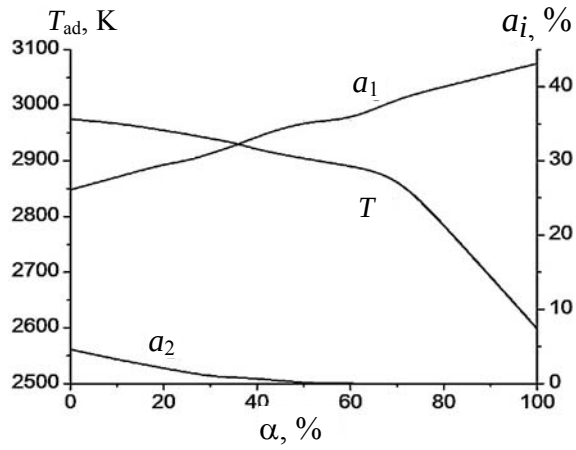

Fig. 4. Effect of α on the calculated adiabatic temperature T_{ad}, mass fractions of metallic a_1 and gaseous a_2 chemical conversion products

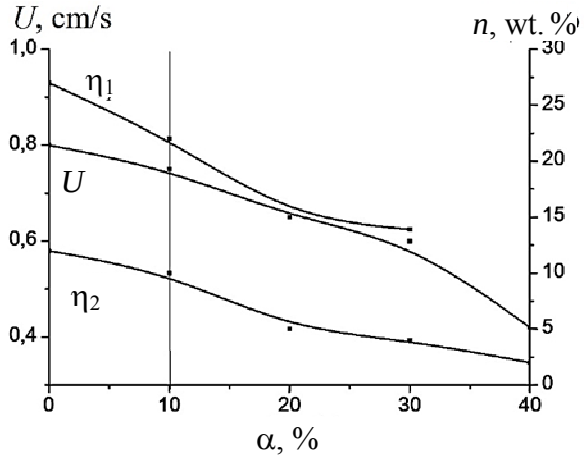

Fig. 5. Burning velocity *U*, yield of metallic phase η_1, and spread of combustion products (dispersion) η_2 as a function of *n*
$U = l/t$, where l is the height of the mixture, t is the time of burning; $\eta_1 = m/M_1$, $\eta_2 = [(M_1 - M_2)/M_1]\times 100$ %, M_1 is the mass of the initial mixture, M_2 is the mass of the final combustion products and m is the mass of the metal ingot

dropped to 2600 K. The quantity of gaseous combustion products decreased to zero at $\alpha = 50$ %. The yield of the desired product a_1 increased with increasing α.

According to the experimental data, the mixtures burned within the range $\alpha = 0$–40 % (Fig. 5). With increasing α, the burning velocity *U*, yield of metallic phase η_1, and spread of combustion products η_2 decreased. At $\alpha = 10$ %, the limit of phase separation takes place. The introduction of highly exothermic additive CaO_2 + Al led to an increase in the phase-separation limit to 30 %.

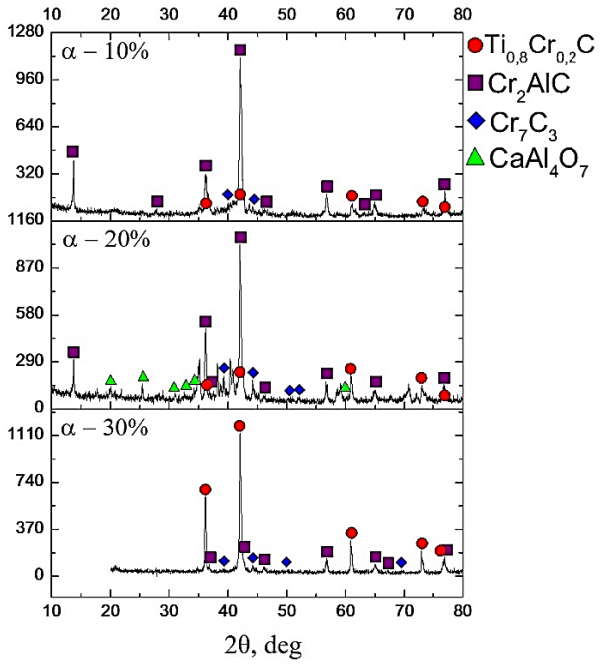

Fig. 6. X-ray diffraction pattern of the product obtained at α = 30 %

The XRD analysis of the products showed that an increase in the fraction of mixture (2) in the charge led to a decrease in the amount of the Cr_2AlC phase and an increase in the amount of the $Ti_{0.8}Cr_{0.2}C$ phase in the combustion product (Fig. 6).

Conclusions

The regularities of combustion and autowave chemical transformation of the highly exothermic composition $CaCrO_4$ / Al / C at various carbon contents are studied. It is shown that the mixtures are capable to burn in a wide range of carbon content.

The study of the $CaCrO_4$ / TiO_2 / Al / Ca /C system showed that the mixture burns in a wide range of α. The combustion temperature of the mixture at $\alpha > 10$ % is insufficient to produce cast product.

The high-exothermic additive CaO_2 + Al allows to expand the combustion limits to $\alpha = 40$ % and the phase separation to $\alpha = 30$%.

X-ray diffraction analysis of the samples showed that with increasing α (TiO_2), the content of the target product $Ti_{0.8}Cr_{0.2}C$ increases, the content of Cr_2AlC MAX phase decreases.

Acknowledgements

The study was supported by RFBR (*project No. 18-08-00804*).

References

1. Kiffer R., Benezovskii F. *Tverdye materialy* [Solid materials]. Moscow, Metallurgiya, 1968. 384 p. (Rus)

2. Rudneva V.V., Galevskii G.V. Issledovanie korrozionnoi stoikosti nanoporoshkov tugoplavkikh boridov i karbidov v rastvorakh elektrolitov [Investigation of the corrosion resistance of nanopowders of refractory borides and carbides in solutions of electrolytes]. *Izv. vuzov. Cvetnaja metallurgija*, 2007, issue 2, pp. 67-70. (Rus)

3. Guilemagy J.M., Espallargas N., Suegama P.H., Benedetti A.V. Comparative study of Cr_3C_2–NiCr coating. *Corrosion science*, 2006, vol. 48, pp. 2998-3013.

4. Miloserdov P.A., Yukhvid V.I., Gorshkov V.A., Ignat'eva T.I., Semenova V.N., Shchukin A.S.. Combustion and autowave chemical transformations of a highly exothermic CaCrO4/Al/B mixture. *Combustion, explosion, and shock waves*, 2017, vol. 53, issue 6, pp. 665-668.

5. Andreev D.E., Yukhvid V.I., Ikornikov D.M., Sanin V.N. Ti–Al–Nb material for high-temperature applications: Combustion synthesis from oxide raw materials. *Key engineering materials*, 2017, vol. 746, pp. 262-266.

6. Shiryaev A. Thermodynamics of SHS processes: An advanced approach. Int. *J. of SHS*, 1995, vol. 4, issue 4, pp. 351-362.

DOI: 10.17277/amt.2018.03.pp.013-016

Explosive Hardening and Its Application in Production of Railroad Switch Frogs

A.A. Deribas[1], A.A. Shtertser[2]*, E.E. Zubkov[3]

[1] *Joint Institute for High Temperatures of Russian Academy of Sciences, Izhorskaya St., 13, Bd.2, Moscow, 125412, Russia;*
[2] *Lavrentyev Institute of Hydrodynamics, Siberian Branch, Russian Academy of Sciences, Lavrentyev avenue, 15, Novosibirsk, 630090, Russia;*
[3] *Joint Stock Company "Novosibirsk Railroad Switch Plant", Aksionov St., 7, Novosibirsk, 630025, Russia*

* Corresponding author: Tel. +7(913) 901 1678. *E-mail*: asterzer@mail.ru

Abstract

The peculiarities of explosive hardening (**EH**) associated with the impact of the shock wave on the metal are considered. Mechanical properties of Hadfield steel after EH are given. It is shown that intermediate layer of dry sand between explosive charge and treated metal provides amplification of the shock wave. This enables EH with the use of powdered explosives with low density and detonation velocity. The industrial technology of EH of railroad switch frogs is described. EH increases the service life of these parts by 20–30 %.

Keywords

Explosive hardening; shock wave; Hadfield steel; railroad switch frog; mechanical properties; hardness.

Introduction

The first patent on explosive hardening (**EH**) of high-manganese steel was issued in 1955 [1]. Since then R&D works has continued in the US, in 1960s they had begun in the former USSR and later in Japan, China and other countries [2–10]. It was found, that strong shock wave generated by explosion can heat the substance up to the melting point, induce phase transitions and twinning (Neumann bands), change microstructure and mechanical properties, such as hardness, plasticity and strength. The effect of EH is associated with an impact of the shock wave on the metal. Strain rates in a shock wave front moving in metal are greater than 10^3 s^{-1} [5]. For a noticeable hardening, the shock wave must be rather strong, i.e. to have an amplitude exceeding the elastic limit of the material. For example, elastic limits of aluminum alloy 2024, deformed (50 %) copper, nickel, structural steel 1020 and titanium are equal to 529, 617, 980, 1215 and 1813 MPa, respectively [5].

Though it has been more than 50 years since research works on EH have started, the interest in this phenomenon still exists and research is ongoing, for example in the search for new explosives suitable for EH [11]. This paper is focused on the description of explosive hardening of Hadfield steel and use of this technology in production of railroad switch frogs at Novosibirsk Railroad Switch Plant.

Experimental

The first series of experiments was carried out using the direct explosive loading (see Fig. 1*a*) of samples made of Hadfield steel with different initial mechanical properties. Plasticized explosive GP-87 used for hardening has had a detonation velocity of 7.2 km/s and a density of 1.6 g/cm^3. The thickness of explosive charge varied from 6 to 15 mm. Table 1 shows the results of experiments, the initial properties of samples are given in the second column.

The second series of experiments was carried out using the indirect explosive loading with an intermediate layer of dry sand between the explosive charge and treated sample (Fig. 1*b*). The objective was to compare the degree of hardening obtained by direct and indirect loading using both plasticized and powdered explosives. These experiments were stimulated by theoretical considerations stated in [12], where it was shown that the pressure in the shock wave reflected from a substrate in a porous layer is greater than the pressure of shock wave generated in direct contact of the same explosive with the same substrate.

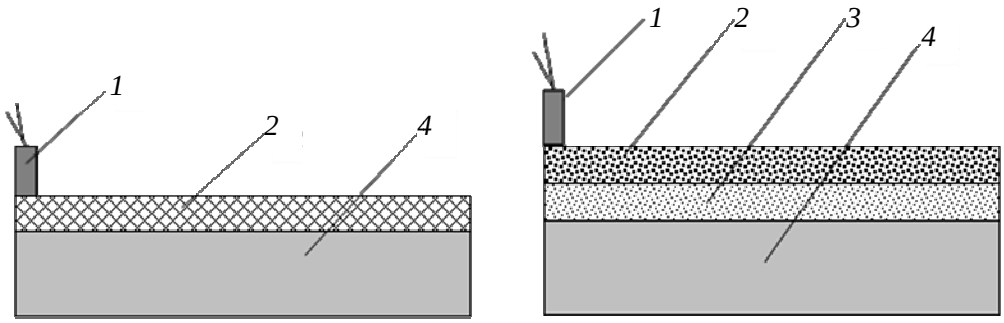

a) *b*)

Fig. 1. Hardening by a contact explosive charge (*a*) and through an intermediate porous layer (*b*):
1 – detonator; *2* – high explosive; *3* – porous layer (dry sand); *4* – sample under treatment

Table 1

Properties of Hadfield steel after explosive hardening

Thickness of GP-87 layer, mm	0	6	9	12	15
Surface hardness, HB	210	321	345	365	375
Tensile strength, MPa	684	832	1008	830	1004
	785	932	1043	1035	1104
	887	997	1117	1079	1174
	964	1078	1181	1133	1238
Yield strength, MPa	432	719	844	814	965
	439	757	856	883	947
	439	773	882	902	981
	452	766	894	941	985
Elongation, %	27	13	11	6	4
	33	15	12	8	7
	42	21	19	14	13
	48	31	23	18	17
Narrowing, %	26	17	17	12	7
	28	21	17	13	12
	33	24	20	16	15
	37	27	26	21	20

This amplification effect has been later confirmed experimentally, and the new method of explosive hardening has been patented [13]. Fig. 2 shows the results of experiments.

Results and discussion

Table 1 shows that Hadfield steel loses plasticity significantly during explosive hardening. For example, when it is hardened to a hardness of 365 HB, a ductility of samples with initial elongation δ = 25–35 % drops to

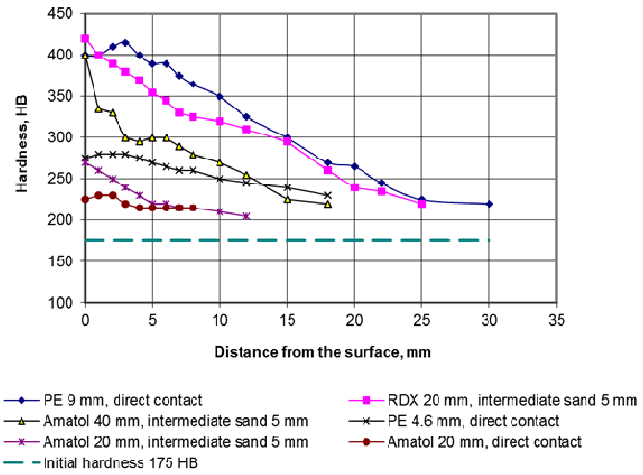

Fig. 2. Dependence of hardness on a distance from the sample surface in explosively hardened high-manganese steel. PE is a plasticized explosive GP-87

δ = 8 %, and that of samples with initial δ = 45–50 % drops to 18 %. In general, explosive hardening of cast high-manganese steel parts intended for operation on the railroad is reasonable, when their initial ductility exceeds 30% in order to avoid the loss of plasticity after hardening and caused by this cracking and chipping of metal during part operation.

In Fig. 2 we can see that explosive hardening using powdery amatol and RDX with the charge thickness of 40 and 20 mm correspondingly, and with an intermediate layer of dry sand (see Fig. 1*b*), provides the same surface hardness as the treatment with 9 mm thick plasticized explosive GP-87 placed in direct contact with the sample (see Fig. 1*a*). Table 2 contains detonation characteristics of above explosives and of plasticized explosive LVV-11-1 used presently in industrial explosive hardening technology. It is obvious that not only high explosives with high density and detonation velocity are suitable for EH, but low-density powdery explosives as well, if to apply a porous interlayer between the explosive charge and treated sample.

Table 2

Detonation characteristics of explosives used for hardening

Explosive	Density, g/cm^3	Detonation velocity, km/s	Detonation pressure, GPa
GP-87	1.60	7.2	21.0
RDX	1.00	6.2	10.0
Amatol	1.00	4.2	5.0
LVV-11-1	1.42	7.4	19.4

Industrial application of explosive hardening

The first steps to the full-scale industrial application of EH were taken in 1960s, when Administration of Novosibirsk Railroad Switch Plant has applied to Lavrentyev Institute of Hydrodynamics with the problem of increasing the service life of the railroad switch frog. The most wear places are on the frog guardrails and frog core wedge (Fig. 3).

Over decades, Lavrentyev Institute of Hydrodynamics, Ural Branch of All-Russian Institute of Railway Transport and Novosibirsk Railroad Switch Plant have conducted the research works, developed the technology, and designed and manufactured explosion chambers. Service tests of hardened frogs were carried out and it has been proven that EH increases their lifetime by at least 20–30 %. Finally, in 1979 the special shop for EH of switch frogs has started working in Novosibirsk Railroad Switch Plant. Subsequently the developed technology was patented [14–16].

Fig. 4 shows the implementation of EH process in explosion chamber. EH increases the surface hardness from 200 HB to 350–380 HB, the depth of a hardened material amounts to 30–35 mm. This prevents the initial crushing of the frog core and guardrails in the operation and therefore its lifetime grows.

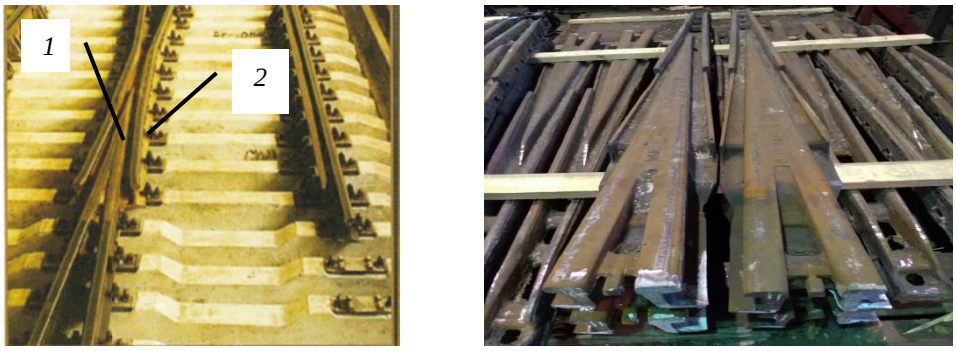

a) *b*)

Fig. 3. Railroad switch frog on the railway track (*a*) and switch frog castings before explosive hardening (*b*):
1 – frog core wedge; *2* – guardrail

a) *b*)

Fig. 4. Explosive chamber in the open state (*a*) and the switch frog on the working table with explosive charge on the hardened surfaces (*b*)

Conclusion

Based on R&D works conducted in Lavrentyev Institute of Hydrodynamics and Ural Branch of All-Russian Institute of Railway Transport, a full-scale production of hardened railway switch frogs was organized at Novosibirsk Railroad Switch Plant. Since 1979, the hardening shop at the Plant has produced more than 350 thousand switch frogs. Presently, the production volume of the said Plant is 10–12 thousand hardened pieces per year. More than 90% of produced R65 frogs (grades 1/11 and 1/9) are explosively hardened. Explosive hardening increases the lifetime of frogs by 20–30 %.

References

1. McLeod N.A. Method of hardening manganese steel. *US Patent* No. 2703297, Mart 1, 1955.
2. Rinehart J.S., Pearson J. *Explosive working of metals*. New York, Pergamon Press, 1963. 351 p.
3. Cowan G.R., Holtzman A.H. Process for hardening metals using explosive means. *US Patent* No. 3218199, Nov. 16, 1965.
4. Deribas A.A., Matveenkov F.I., Sobolenko T.M. Explosive hardening of high-manganese steel. *Combust. Explos. Shock Waves*, 1966, v. 2, issue 3, pp. 53-57.
5. Deribas A.A. *Fizika uprochnenija i svarki vzryvom* [Physics of explosive hardening and welding]. Novosibirsk, Nauka, 1980 (Rus).
6. Chen Y.F., Hong Y.Q. Explosion hardening technology for high manganese steel. *CN Patent* No. 85103847, May 6, 1985.
7. Akira O., Hideaki M. Residual Stress in Long Size Tapered Block of Explosion Hardened High Manganese Austenitic Cast Steel. *J. Soc. Mater. Sci. Jpn*, 1985, vol. 34, issue 384, pp. 1019-1024.
8. Zhang F., Lei T. A study of friction-induced martensitic transformation for austenitic manganese steel. *Wear*, 1997, vol. 212, issue 2, pp. 151-269.
9. Havlichek P., Nesvadba P. Application of explosive hardening on railway infrastructure parts. *Proceed. Conf. "Metal–2011"*. May 18-20, 2011, Brno, Czech Republic, EU. Conf. paper.
10. Zhang F.C., Lv B., Wang T.S., Zhang C.L., Luo H.H., Liu H., Xu A.Y. Explosion hardening of Hadfield steel crossing. *Materials science and technology*, 2010, vol. 26, issue 2, pp. 223-229.
11. Hu X.Y., Shen Z.W., Iiu Y.B., Iiu, T.S. On Elastic-Plastic Explosives for Explosive Hardening. *Advanced materials research*, 2014, vol. 834/836, pp. 165-168.
12. Kostyukov N.A. Rol' poristoj prokladki pri obrabotke materialov vzryvom [The role of porous interlayer in explosive working of materials]. *Proceed. 2nd meeting on explosive working of materials, Sept. 8-10, 1981, Novosibirsk, Russia*. Novosibirsk, Institute of Hydrodynamics, 1982, pp. 275-277 (Rus).
13. Shtertser A.A., Deribas A.A., Gavril'ev I.N., Kostyukov N.A., The method for increase metal hardness by explosion. *RF Patent* No. 1309404, May 20, 1997.
14. Kats R.Z., Putrja N.N., Krasikov K.I., Deribas A.A., Sobolenko T.M., Pryakhin V.A., Vodyanov A.V., Tsarenko A.G., Zubkov E.E. Method of hardening parts. *USSR Patent* No. 1253150, Apr. 22, 1986.
15. Kats R.Z., Putrya N.N., Krasikov K.I., Vodyanov A.V., Tsarenko A.G., Zubkov E.E., Deribas A.A., Sobolenko T.M., Pryakhin V.A. Method of explosive hardening a cast portion of acute angle frogs of railroad switches. *UK patent* No. 2172234, Sept. 17, 1986.
16. Kats R.Z., Putrja N.N., Tsarernko A.G., Leitsinger A.A., Zubkov E.E., Vodyanov A.V., Pryakhin V.A., Zhidkov A.M. Method of hardening of cast part of railway crossings. *RU Patent* No. 2007478, Febr. 15, 1994.

DOI: 10.17277/amt.2018.03.pp.017-021

Destruction of Silica Fiber Materials under Shock Wave and Radiation Loadings

V.P. Efremov [1]*, A.V. Utkin [1,2]

[1] *Joint Institute for High Temperatures of Russian Academy of Sciences, Izhorskaya St., 13, Bd.2, Moscow, 125412, Russia;*
[2] *Institute of Problems of Chemical Physics, Russian Academy of Sciences, 1, Semenov avenue, Chernogolovka, Moscow Region, 142432, Russia*

* Corresponding author. Tel.: +7 495 485 09 63. *E-mail*: dr.efremov@gmail.com

Abstract

The disturbance of the light conductivity in optical fiber transporting intense laser radiation leads to the occurrence of brightly illuminated laser plasma region. Plasma begins to move towards radiation, irreversibly damaging the optical fiber. Depending on the intensity of the laser energy, different rates of propagation of damage along the optical fibers towards the radiation are possible. This is either "combustion" of optical fibers, or "optical detonation". Both of these processes – "combustion" and "optical detonation" of optical fibers – destroy the light conductivity of silica fibers along the entire length. The rate of propagation of "combustion" depends on the energy density and is several meters per second. The detonation-like mode of destruction extends with velocity of several kilometers per second. Shock-wave data of silica fiber materials are necessary for modeling of the of such destruction process. In this paper the experimental study of propagation of the shock wave front in the materials of the optical fibers core in explosive experiments was carried out for the first time. For study of the detonation-like mode of a laser discharge propagation, experimental fibers were produced by the Fiber Optics Research Center of the Russian Academy of Sciences (**FORC RAS**) and an available industrial communication fiber (SMF-28e single-mode fiber from Corning). In the shock wave experiment, a two-wave mode of the propagation of the shock wave is confirmed. Anomalous compressibility behind the front of the shock wave was found in the materials of the optical fiber. The decrease in the sound velocity was about one km/s.

Keywords

Laser-supported detonation; single-mode fiber; laser plasma.

Introduction

Intensive laser radiation can lead to the emergence plasma and propagation of damage in optical fibers. Depending on the intensity of the laser, different velocities of propagation of damage along the optical fibers towards the radiation are possible. This is either "combustion" of optical fibers or "optical detonation" [1, 2]. Both of these processes – "combustion" and "optical detonation" of optical fibers destroy the light conductivity of silica fibers along the entire length. The rate of propagation of "combustion" depends on the energy density and is several meters per second.

The detonation-like mode of destruction extends at velocity of several kilometers per second. The analysis of the limiting possible velocity for such a mode is important both for the safety of optical lines based on silica fibers and for the construction of high-power lasers on fiber optics. In addition, the physical explosion of the optical fiber in the transport reservoirs can lead to the initiation of explosive combustible of gas mixtures (secondary explosion).

In the experiments, we recorded the following parameters:

– the velocity of propagation of the process along the fiber – by streak camera;

– the zone of pressure, plasma glow and the beginning of destruction – by fast camera from the exposure time of 2 ns;

– the acoustic precursor (compression wave) – by fast camera from the exposure time of 2 ns and using the technique of crossed polarizers.

The results of dynamic measurements were published in our early papers [1–6].

The interpretation of experimental results and the construction of numerical models were constrained by

the lack of data on the properties of materials used for the fiber core. In particular, there were no data on the shock-wave properties and the structure of the compression wave front.

In this paper, for the first time, an experimental study has been carried out of the features of the propagation of the shock wave front in materials of optical fibers.

Experimental

For study of the detonation-like mode of a laser discharge propagation, experimental fibers were produced by the Fiber Optics Research Center of the Russian Academy of Sciences (FORC RAS) and an available industrial communication fiber (SMF-28e single-mode fiber from Corning).

Most optical cables are assembled from SMF-28e. This fiber has a stepped profile of the refractive index due to the introduction of the GeO_2 additive (~ 3 mol %) into the core; it has a core diameter of 8.2 μm and a quartz shell diameter of 125 μm. The optical fiber is coated with a polymer shell with a diameter of 240 μm.

The microstructure of damages of fibers after optical detonation was studied with a scanning electron microscope.

The optical fiber parameters are given in Table 1. F1 and F2 are model optical fibers. F2 is a model optical fiber, close in parameters to the Corning SMF-28 industrial fiber.

The experiments were carried out on samples prepared from the blanks for optical fibers in FORC RAS (Fig. 1*a*). The photos of the samples are shown in Fig. 1*b* and Fig. 1*c*. The samples were made in the form of disks with a diameter of 12 mm, a thickness of 2 mm and a core of 4 mm. The average density of the produced disks was $\rho_0 = 2.27$ g/cm^3.

The mass velocity was recorded by an interferometer (VISAR) through a water window. The aluminum foil with 7 μm thick was glued on samples to reflect laser radiation of interferometer. The explosive device used in the experiments is show in Fig. 2. The experimental assembly in the experiments is shown in Fig. 3. The photo of the assembly sequence of the experimental setup is shown in Fig. 4.

Table 1

Parameters of optical silica-based fibers

Fiber	F1	F2	F3(Corning SMF-28^{TM})
Quartz cower diameter, μ	600	125	125
Core diameter, um	9.5	7.7	8.2
Refractive index difference (RID)	0.006	0.013	0.005
Composition SiO_2 : GeO_2 : Al_2O_3	97 : 1 : 2	89 : 11 : 0	96.5 : 3.5 : 0
Mode field diameter at the laser wavelength 1064 nm, um	10.5	6.13	8.9

For F2 fiber with a large decline in the refractive index (RID) in the center – an effective step index; F3 fiber – Corning SMF-28^{TM}

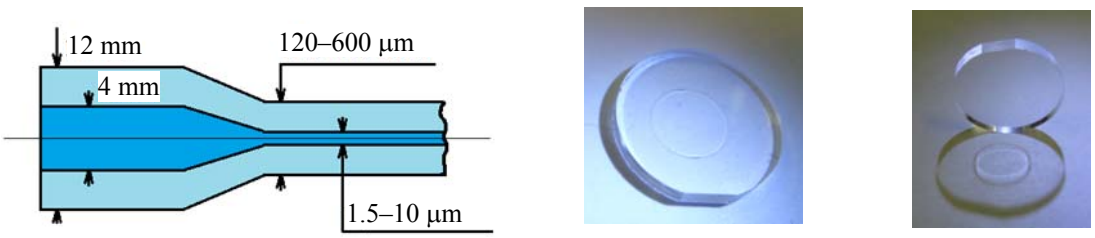

a) *b*) *c*)

Fig. 1. Photos of samples
(Samples were made in the form of disks with a diameter of 12mm, a thickness of 2 mm and a core of 4 mm. The average density of the produced disks $\rho_0 = 2.27$ g/cm^3)

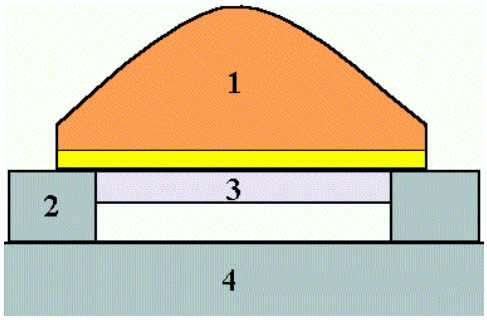

Fig. 2. Explosive device:
1 – explosive lens, A-IX-1/ paraffine, Ø = 100 mm; *2* – focusing ring, steel, $Ø_{ext}$ = 150 mm, *h* = 16 mm; *3* – impactor, D16T, Ø = 90 mm, *h* = 7 mm; 4 – screen, impactor velocity 1.13 km/s

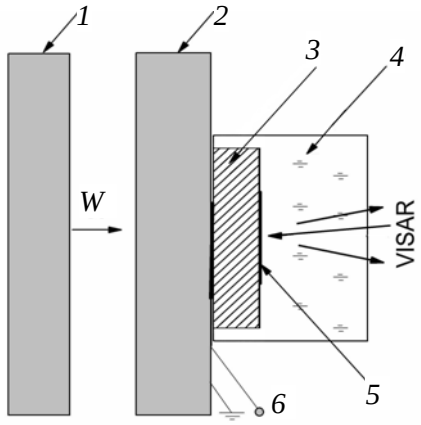

Fig. 3. Experimental assembly:
1 – aluminum impactor; *2* – screen; *3* – sample; *4* – water; *5* – aluminum foil; *6* – polarization sensor

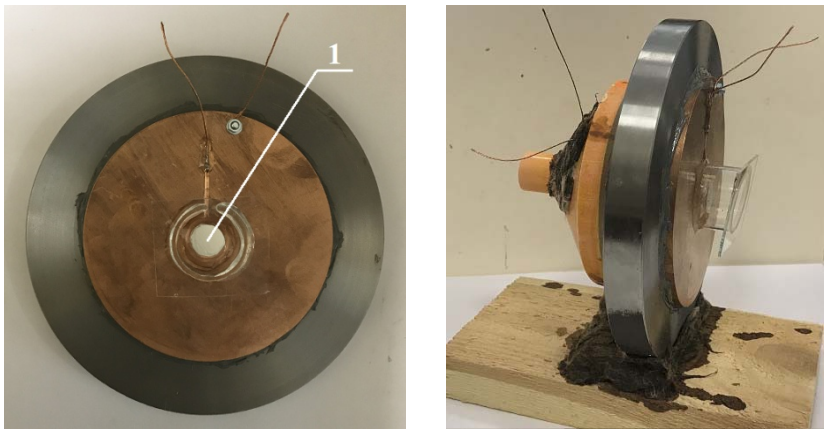

Fig. 4. Photo of experimental assembly (*1* – sample of the fiber core)

The front of the shock wave has a distinctly expressed two-wave structure: a wave with amplitude of about 400 m/s and a diffuse front followed by a second wave with a sharp front (Fig. 5): D_1 – velocity of the first wave (short arrow); D_2 – velocity of the second wave (long arrow).

If two wave configurations are realized, then the waves should scatter. This is precisely what is observed when the thickness of the samples is changed by a factor of two. The first wave is blurred as it spreads, which is due to the anomalous compressibility of fused quartz at a pressure below 2.5–3.0 GPa.

Fig. 6 shows the front parts of the velocity profiles in the *t*/*h* coordinates, where *h* is the thickness of the sample. In these experiments, the compression stress did not exceed the value of the dynamic elastic limit of fused quartz, which is equal to 8.8 GPa [8, 9]. A good coincidence of the wave profiles in these coordinates indicates the self-similarity of the compression wave and makes it possible to find the character of the decrease in the sound velocity with increasing pressure in the region of anomalous compression.

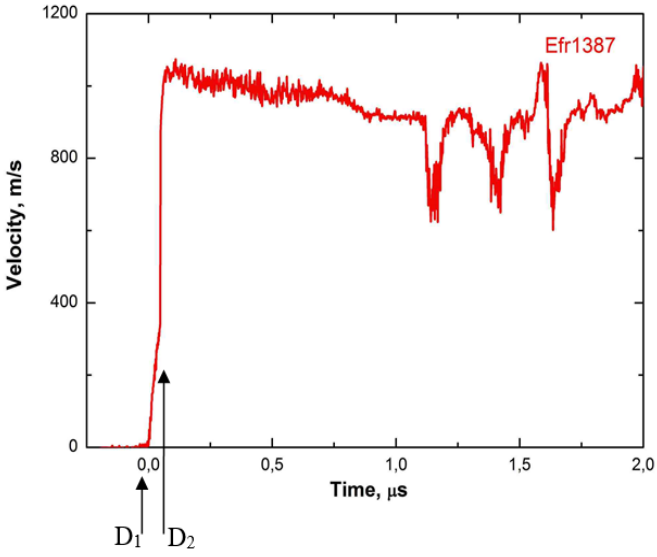

Fig. 5. Mass velocity at the quartz-water interface
(Aluminum impactor *h* = 7 mm, *W* = 1.13 km/s; aluminum screen *h* = 4 mm; sample *h* = 2 mm. The shock wave velocity D_1 =5.47 km/s, D_2 = 4.73 km/s)

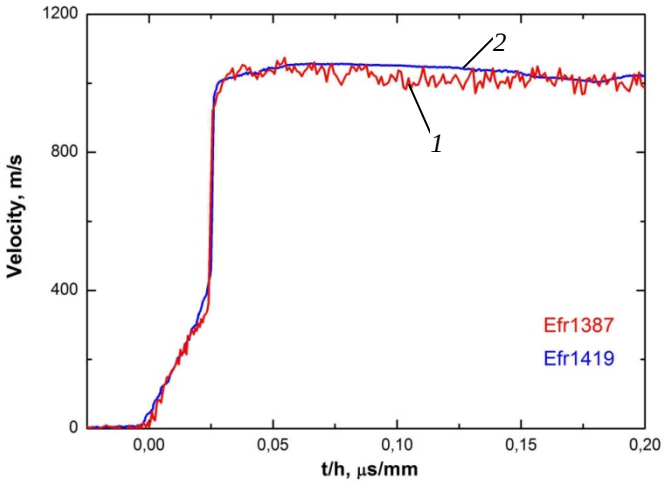

Fig. 6. Aluminum impactor h = 7 mm, W = 1.13 km/s; aluminum screen h = 4 mm; sample 2 mm (red *1*) and 4 mm (blue *2*)

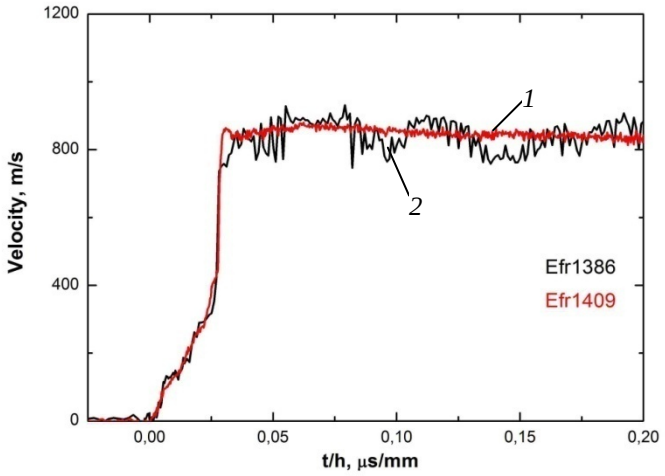

Fig. 7. Aluminum impactor h = 7 mm, W = 1.13 km/s; copper screen h = 5.5 mm; sample 2 mm (red *1*) and 4 mm (black *2*)

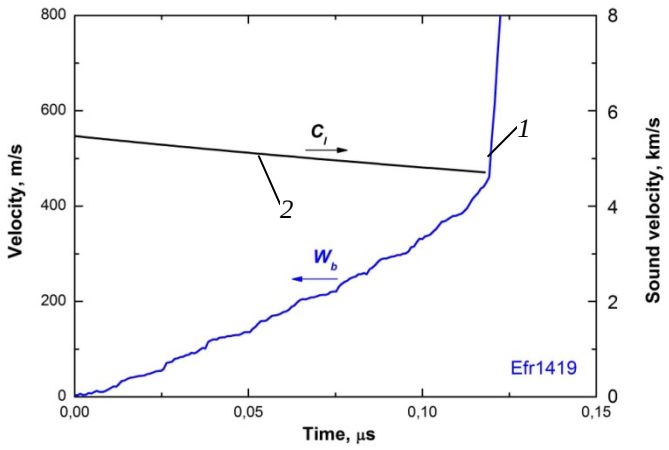

Fig. 8. Aluminum impactor h = 7 mm, W = 1.13 km/s; aluminum screen h = 4 мм; sample thickness 4 mm; velocity profile (blue *1*) and sound velocity (black *2*) in the region of anomalous compression

The similarly way, in Fig. 7 in the t/h coordinates, the front part of the velocity profiles is constructed at a lower shock compression pressure (copper screen). In spite of the strongly oscillating velocity profile 1409, in this case a fairly good coincidence of the wave profiles is also observed. Fig. 8 shows the velocity profiles (blue line *1*) and the sound velocity (black line *2*) in the region of anomalous compression.

Results and discussion

The propagation of the destruction process is caused by the laser plasma in the volume of the material and by a sharp increase in the absorption coefficient of the laser radiation in the layers of material nearby with laser plasma zone. The burning mode with a wave propagation velocity of about 1 m/s is achievable even at a laser radiation intensity (wavelength 1 μm) in the core of the fiber of the order of 0.1 W/μm^2, the detonation mode occurs at a velocity of about ~ 3 km/s at intensities above ~ 20 W/cm^2. The nature of the dependence of the wave velocity on the absorbed laser energy is different in these two modes. In both cases, there is a strong heating of the core material of the fiber, which radiates as a black body. The temperatures of laser heating of the matter can reach 10^4 K. However, the rates of matter heating K_t in the wave fronts differ by three orders of magnitude.

The terms “combustion” and “optical detonation” introduced from chemical media are used here quite arbitrarily. In contrast to the release of internal energy in the front during ordinary combustion and detonation, transition of the transported energy of laser radiation occurs to thermal energy in transparent media.

During combustion, the displacement of the absorption front occurs with a thermal wave, during detonation – with a shock wave. The application of the term and the theory of combustion to optical combustion was shown in [7].

A strong evidence of application of the term “optical detonation” to the process under investigation is hampered by the complex nature of the flow in the front and the dependence of the energy release process on the radius.

The driver of damage to the optical fiber is the formation of laser plasma in the core of the optical fiber, the temperature of which can reach 10^4 K. The channel filled with gas remains after cooling in the core. In the combustion mode, the cavity moves along with the plasma front; depending on the conditions in the core, there can be both a continuous channel and a periodic sequence of bubbles; its formation occurs

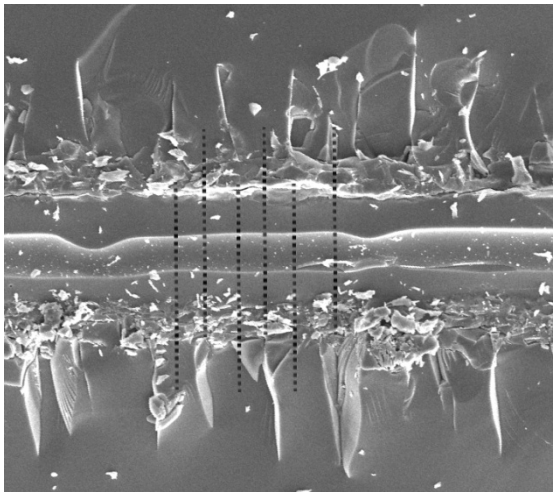

Fig. 9. Photograph of the stored fiber. Detonation region
(Dashed lines indicate the position of the axial planes in which the radial cracks lie. The destruction wave moved from right to left)

under conditions of a flux of matter along the fiber axis and the hydrodynamic instability of the liquid glass-gas interface. In high-speed mode, the plasma front moves only about 200 ns (for our experimental conditions), which is much less than the cooling time of the substance. In this case, the resulting cavity can be described as a central channel extending from the start position to the stopping point.

A fundamental difference in the destruction of optical fibers in the fast mode is the formation of cracks in the quartz shell, occurring at the shell-core interface. The pressure near the plasma front is higher than the strength of the material. The character of the crack formation is varied in different sections of the fast mode. In addition, the cracks formed in the quartz shell cause splitting of the fiber in the longitudinal direction. This allowed us to gain access to the core region of the saved samples, previously removing the polymer coating of the optical fiber by heating on a metal plate with a temperature of about 500 °C during 30 seconds. In the same experiments, where the polymer coating was previously removed, the sample disintegrated into several parts during the passage of the destruction wave. The saved sample of the optical fiber is shown in Fig. 9. It can be seen that along the axis there is an empty channel surrounded by the melted zone, the area of intense crushing and radial cracks.

Conclusion

Earlier the dynamics of the laser destruction of optical fibers were studied [3]. Two wave profiles of the shock wave were detected. These studies were carried out using a fast camera. After the laser destruction process with the help of a scanning electron microscope, the character of the destruction of the saved fragments was studied.

For the first time the experimental study of the propagation of the shock wave front in the materials of the core of optical fibers was carried out in explosive experiments. Two wave profiles of the shock wave were confirmed. Anomalous compressibility behind the front of the shock wave was found. In this area, the decrease in the sound velocity was about one km/s.

Acknowledgements

The authors are grateful to S.L. Semenov, Director of Fiber Optics Research Center of the Russian Academy of Sciences, for supporting the research.

The research was funded by the Program of Fundamental Research of the Presidium of the Russian Academy of Sciences (Program Code I.31P).

References

1. Dianov E.M., Fortov V.E., Bufetov I.A., Efremov V.P., Frolov A.A., Schelev M.Y. and Lozovoi V.I. Detonation-like mode of the destruction of optical fibers under intense laser radiation *J. Exp. Theo. Phys. Lett.*, 2006, vol. 83, issue 2, pp. 75-78.

2. Efremov V.P., Frolov A.A., Dianov E.M., Bufetov I.A., Fortov V.E., Dynamics of laser-induced shock wave in silica *Archives of Metallurgy and Materials*, 2014, vol. 59, issue 4, pp. 1599-1603.

3. Efremov V.P., Fortov V.E., Frolov A.A. Damage of silica-based optical fibers in laser supported detonation *Journal of Physics: XXX International Conference on Interaction of Intense Energy Fluxes with Matter*, 2015, vol. 653, p. 012-013.

4. Efremov V.P., Ivanov M.F., Kiverin A.D., Yakovenko I.S. Mechanisms of direct detonation initiation via thermal explosion of radiatively heated gas-particles layer *Results in Physics*, 2015, vol. 5, pp. 290-296.

5. Efremov V.P., Frolov A. A., and Fortov V.E. Laser Supported Detonation in Silica-based Optical Fibers // 25th ICDERS August 2 – 7, Leeds, UK, 2015, pp. 1-5.

6. Efremov V.P. [Combustion and detonation of transparent dielectrics with external energy supply], *Sbornik materialov Mezhdunarodnoj konferencii «SVS–50», priurochennoj k 50-letnemu yubileyu nauchnogo otkrytiya metoda samorasprostranyayushchegosya vysoko-temperaturnogo sinteza (SVS)*. Chernogolovka, ISMAN, 2017, pp. 99-101. (Rus)

7. Gorbachenko V.I., Dovzhenko A.Yu., Merzhanov A.G., Rumanov E.N., Fortov V.E., Yachmeneva O.E. [Limits of propagation of a slow wave of optical breakdown in an optical fiber]. *Doklady akademii nauk*, 2010, vol. 433, issue 5, pp. 618-620.Wackerle J. Shock-Wave Compression of Quartz *J. Appl. Phys,* 1962, vol. 33, p. 922. (Rus)

8. Wackerle J. Shock-Wave Compression of Quartz, *J. Appl. Phys,* 1962, vol. 33, p. 922.

9. Barker L.M., Hollenbach R.E. Shock-Wave Studies of PMMA, Fused Silica, and Sapphire *J. Appl. Phys,* 1970, vol. 41, p. 4208.

DOI: 10.17277/amt.2018.03.pp.022-025

The Peculiarities of Wave Formation at Explosive Welding Via thin Interlayer

B. Zlobin, V. Kiselev, A. Shtertser*, A. Plastinin

Lavrentyev Institute of Hydrodynamics, Siberian Branch, Russian Academy of Sciences, Lavrentyev avenue, 15, Novosibirsk, 630090, Russia

*Corresponding author: Tel. +7(913) 901 1678. *E-mail*: asterzer@mail.ru

Abstract

During the experiments on explosive welding of low-plasticity steels with thin interlayer of ductile metal between them, it was found that the size of the waves generated in the bonding area can be different, even if the collision conditions and colliding materials are the same. However, the wavelength λ lies in the range between λ_{max} and λ_{min} determined by contact point velocity v_c, collision angle γ, hardness (HV_1, HV_2) and densities (ρ_1, ρ_2) of colliding plates. The formulas for calculation of the allowed range of values for wave lengths and amplitudes are proposed.

Keywords

Explosive welding; interlayer; wave formation; Landau model; wavelength; wave amplitude.

Introduction

Explosive welding is the process in which the high speed flying plate (flyer plate) collides with the resting plate (parent plate) at a certain angle, at that the flyer plate is accelerated by explosion. The wave formation phenomenon related to explosive welding (**EW**) is well known and there are more than a dozen of models devoted to its description [1]. However, there is yet no satisfactory theory for prediction of wave size considering the strength and physical properties of colliding materials, while experiments show that their hardness and density affect the length and amplitude of generated wave [2]. Evidently, the control of wave formation is very important in welding of low-plasticity metals and alloys, when the problem of cracking arises. Experiments show that it is possible to reduce the wave size, when a flyer plate is in advance clad with a thin copper layer [2, 3]. This is an effective way to get bonding without cracking. The experiments have shown the existence of two types of waves (small and large) occurring in the bond zone and differing in wavelength and wave amplitude [3]. The possible existence of two types of waves has previously been discussed in [4], but experimentally proved for the first time in [3].The present paper describes the last research results on the topic of wave formation at EW via thin interlayers.

Experimental. Materials and methods

Prior experiments showed that strength and density of colliding materials significantly affect the wave size [2, 5]. For example, when the hardness of materials differs by more than 10 times, the boundary is waveless [5]. The same was observed when the densities differed by more than 3 times [2]. To study the wave formation in the presence and absence of the interlayer, a series of experiments on EW of hardened steels was carried out using thin interlayers of different ductile materials. Fig. 1 shows the polished section of the weld zone that has appeared in result of EW performed in two steps. First, the 3 mm thick steel plate with a hardness of 460 HV was clad with the 0.3 mm thick copper band with the hardness of 78 HV. Then, the copper layer was removed from the part of the surface of bimetal by milling, and the obtained plate was welded onto a steel plate with a hardness of 320 HV.

The described method enables obtaining two bonding areas in one experiment: steel-steel area, and

steel-interlayer-steel one. The same approach was employed in further experiments on EW of hardened steel plates using copper, aluminum, titanium and mild steel interlayer. Fig. 2 shows wavy interfaces got by EW of two steel plates using the mild steel interlayer. The flyer plate (3.5 mm thick) and parent plate (25 mm thick) were made of hardened 30HGSA steel with a hardness of 334 HV. Interlayer (0.5 mm thick) is made of low-carbon steel with a hardness of 131 HV.

All welded samples were cut and microsections were made from them to measure the size of emerging waves. The welding parameters (v_c, γ) and the measured wave lengths λ and amplitudes a are given in Table 1.

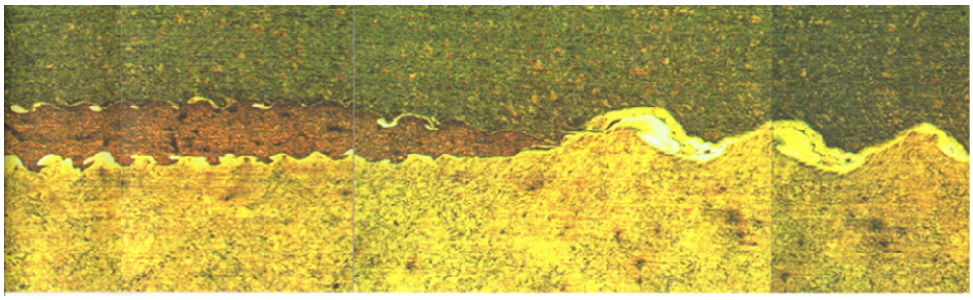

a) *b*)

Fig. 1. Small (*a*) and large (*b*) waves in the bond zone of steel plates welded via copper interlayer (*a*) and directly (*b*) in one experiment at collision point velocity v_c = 2.5 km/s and collision angle $\gamma \approx 10°$

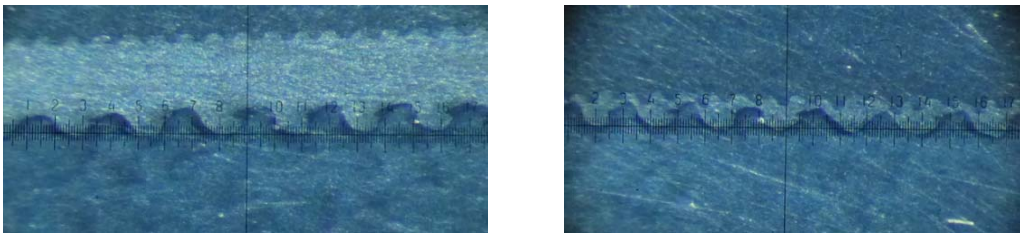

a) *b*)

Fig. 2. Welding two plates of hardened steel:
a – bonding through the interlayer of mild steel, *b* – direct bonding

Table 1

Collision parameters and wave sizes

No.	Flyer plate	Interlayer	Parent plate	$D = v_c$, km/s	γ, °	λ, mm	a, mm
1	2	3	4	5	6	7	8
1	30HGSA, δ = 1.5 mm, 35HRC (334HV)	Cu, δ* = 0.5 mm, 60HB (78HV)	30HGSA, δ_1 = 25 mm, 35HRC (334HV)	2.20	12	0.381	0.056–0.085
2	30HGSA, δ = 3.0 mm, 35HRC (334HV)	Cu, δ* = 0.5 mm, 60HB (78HV)	30HGSA, δ_1 = 25 mm, 35HRC (334HV)	2.25	12	0.449	
3	30HGSA, δ = 4.5 mm, 35HRC (334HV)	Cu, δ* = 0.5 mm, 60HB (78HV)	30HGSA, δ_1 = 25mm, 35HRC (334HV)	2.63	12	0.538	0.035–0.070
4	60G2A, δ = 3 mm, 45HRC (460HV)	Cu, δ* = 0.3 mm, 60HB (78HV)	30HGSA, δ_1 = 25mm, 32–33HRC (320HV)	2.50	9.6	0.24	0.05
	60G2A, δ = 3 mm, 45HRC (460HV)	Cu layer is removed	30HGSA, δ_1 = 25mm, 32–33HRC (320HV)		10.5	0.56	0.1

Continuation of Table 1

1	2	3	4	5	6	7	8
5	St20, δ = 4 mm, 120HB (120HV)	Al, δ* = 1 mm, 30HB (40HV)	St20, δ_1 = 20mm, 120HB (120HV)	2.72	11.2	Can't be measured	
	St20, δ = 4 mm, 120HB (120HV)	Al layer is removed	St20, δ_1 = 20 mm, 120HB (120HV)		12.0	0.64	0.135
6	30HGSA, δ = 3.5 mm, 35HRC (334HV)	VT1-0, δ* = 0.5 mm, 131–163HB (131–162HV)	30HGSA, δ_1 = 25 mm, 35HRC (334HV)	2.58	14.0	0.43	Very small
	30HGSA, δ = 3.5 mm, 35HRC (334HV)	VT1-0 layer is removed	30HGSA, δ_1 = 25 mm, 35HRC (334HV)		14.8	0.81	0.15
7	30HGSA, δ = 3.5 mm, 35HRC (334HV)	St3, δ* = 0.5 mm, 131HB (131HV)	30HGSA, δ_1 = 25 mm, 35HRC (334HV)	2.48	12.8	0.46	0.085
	30HGSA, δ = 3.5 mm, 35HRC (334HV)	St3 layer is removed	30HGSA, δ_1 = 25 mm, 35HRC (334HV)		14.2	0.35	0.075

Notes: 30HGSA (0.28–0.34 C, 0.9–1.2 Si, 0.8–1.1 Mn, 0.8–1.1 Cr, 96 % Fe) is an alloy structural steel; 60G2A (0.57–0.65 C, 0.17–0.37 Si, 0.7–1.0 Mn, 97 % Fe) is a spring structural steel; St20 (0.17–0.24 C, 0.17–0.37 Si, 0.35–0.65 Mn, 98 % Fe) is a structural high quality carbon steel; St3 (0.14–0.22 C, 0.15–0.3 Si, 0.4–0.65 Mn, 97 % Fe) is a mild structural steel of an ordinary quality; VT1-0 (98,61– 99,7 % Ti) is a technical titanium; Cu and Al are the metals of technical purity; δ is the flyer plate thickness, δ^* is the interlayer thickness, δ_1 is the parent plate thickness.

Results and discussion

For the theoretical interpretation of the wave formation phenomenon let's use the approach proposed in [6] and based on Landau model of instability of a stationary flow of a viscous liquid [7]. According to this model, a non-stationary flow in a viscous liquid is characterized by two dimensionless parameters – Reynolds number $R = \rho ul/\eta$ and Strouhal number $S = u\tau/l$, where ρ and η are respectively the density and viscosity of liquid; l – characteristic dimension; u – characteristic velocity and τ – characteristic time of the considered problem.

When as-waves disturbances in a liquid occur spontaneously (not under the action of external periodic force), then S is a function of R, i.e. $S = f(R)$. If we take the period of oscillations T as a characteristic time τ, the contact point velocity v_c as a characteristic velocity u, and the thickness of a cumulative jet δ_j as a characteristic dimension l, then we have

$$S = v_c T / (\delta \cdot \sin^2(\gamma/2)).$$

Here the thickness of a cumulative jet is calculated by the formula $\delta_j = \delta \cdot \sin^2(\gamma/2)$ derived for the collision of a flyer plate with very thick parent plate [8]. Evidently, for the wave disturbances arising in a stationary flow moving with the velocity v_c, there is the relationship $v_c T = \lambda$, because these disturbances are transferred by a flow. Hence we obtain the formula for the wavelength

$$\frac{\lambda}{\delta} = f(R)\sin^2(\gamma/2). \quad (1)$$

Here δ is the flyer plate thickness, ρ_1 and ρ_2 are the densities of flyer and parent plates correspondingly, v_c – the contact point velocity; γ – the collision angle, HV_1 and HV_2 – Vickers hardness of flyer and parent plate respectively. R designates a Reynolds number as it is accepted among specialists in explosive welding [4, 9]

$$R = \frac{(\rho_1 + \rho_2)v_c^2}{2(HV_1 + HV_2)}. \quad (2)$$

Processing the experimental data in the Table 1 howed that there were not only two types of waves described in [3]. It was discovered that the experimental values of wavelength λ fall in the interval between the upper λ_{max} and lower λ_{min} bounderies which depend on the collision angle, contact point velocity, strength and density of colliding materials. These bounds are described by empirical equations

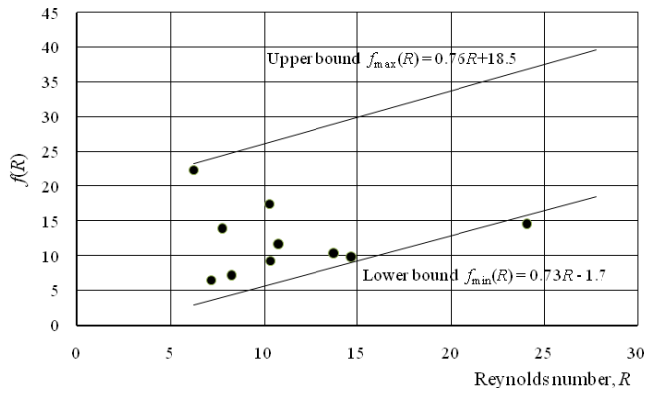

Fig. 3. Dependence of $f(R) = \lambda/(\delta\sin^2(\gamma/2))$ on R

$$\lambda_{max} = f_{max}(R)\,\delta\sin^2(\gamma/2) = \\ = (0.76R + 18.5)\delta\sin^2(\gamma/2); \qquad (3)$$

$$\lambda_{min} = f_{min}(R)\,\delta\sin^2(\gamma/2) = \\ = (0.73R + 1.70)\delta\sin^2(\gamma/2). \qquad (4)$$

Fig. 3 shows $f(R) - R$ diagram on which experimental points and boundaries of the wavelengths area are marked. Experimental points are based on the data of Table 1, while upper $f_{max}(R)$ and lower $f_{min}(R)$ bouderies are built using equations (3), (4).

So, it is impossible to predict exactly the wavelength for a given collision conditions, but a range for λ values can be specified using the equations (2) – (4). As for the wave amplitude, a range of its values has been also found

$$0.14\left(\frac{\rho_{min}}{\rho_{max}}\right)^{2.6} \le \frac{a}{\lambda} \le 0.30\left(\frac{\rho_{min}}{\rho_{max}}\right). \qquad (5)$$

The uncertainty in the wave size can be associated with the uncertainty in the thickness δ_j of cumulative jet arising between the colliding surfaces because it is not solid, but dispersed at $\gamma < 30°$ [10]. Besides, the wave size can be influenced by other reasons associated with acoustic waves travelling in the collided plates.

Conclusion

1. Instead of given in [4] classic formulas for estimation of wave length λ and amplitude *a*, the new modified equations (2) – (5) considering the strength and density of explosively welded materials are proposed.

2. The use of thin ductile interlayer welded previously onto the flyer plate enables to get waves with minimal values of λ and *a*, close to the lower bound of the wave size diapason. This is important when welding low-plasticity metals and alloys.

References

1. Yakovlev I.V., Pai V.V. *Svarka metallov vzryvom* [Explosive welding of metals]. Novosibirsk, Publishing House of Siberian Branch of Russian Academy of Sciences, 2013 (Rus).

2. Zlobin B.S., Shtertser A.A., Kiselev V.V., Plastinin A.V. Bonding and wave formation at the explosive welding of low-plastic materials. In: *Explosive Production of New Materials: Science, Technology, Business, and Innovations.* Ed. by A.A. Deribas, Yu.B. Scheck, and R.I. Mendes. Coimbra, ACIV, 2016. pp. 219-221.

3. Zlobin B.S., Kiselev V.V., Shtertser A.A., Plastinin A.V. Use of emulsion explosives in experimental studies of flows in the bonding zone in explosive welding. *Combust. Explos. Shock Waves*, 2018, vol. 54, issue 2 (In print).

4. Deribas A.A. *Fizika uprochnenija i svarki vzryvom* [Physics of explosive hardening and welding]. Novosibirsk, Nauka, 1980, 221 p. (Rus).

5. Zlobin B., Sil'vestrov V., Shtertser A., Plastinin A., Kiselev V. Enhancement of explosive welding possibilities by the use of emulsion explosive. *Archives of Metallurgy and Materials*. 2014, vol. 59, pp. 1599-1604.

6. Pai V.V., Luk'yanov Ya.L., Kuz'min G.E., Yakovlev I.V. Wave formation in a high-velocity symmetric impact of metal plates. *Combust. Explos. Shock Waves*, 2006. vol. 42, issue 5, pp. 611-616.

7. Landau L.D., Lifshits E.M. *Gidrodinamika* [Hydrodynamics]. Moscow, Nauka, 1988, 736 p. (Rus).

8. Berdychenko A.A., Zlobin B.S., Pervukhin L.B., Shtertser A.A. Possible ignition of particles ejected into the gap in explosive welding of titanium. *Combust. Explos. Shock Waves*, 2003, vol. 39, issue 2, pp. 232-239.

9. Crossland B. *Explosive welding of metals and its application*. Oxford, Clarendon Press, 1982.

10. Shtertser A.A., Zlobin B.S. Flows, strains, and the formation of joints in oblique collision of metal plates. *J. Appl. Mech. Tech. Phys*, 2015, vol. 56, issue 5, pp. 927-935.

DOI: 10.17277/amt.2018.03.pp.026-028

β-SiAlON-Based Ceramic Composites from Combustion-Synthesized Raw Materials by Spark Plasma Sintering

K.L. Smirnov[1]*, E.G. Grigoryev[1], E.V. Nefedova[2]

[1] *Merzhanov Institute of Structural Macrokinetics and Materials Science, Russian Academy of Sciences, 8, Academician Osipyan St., Chernogolovka, Moscow Region, 142432, Russia;*
[2] *National Research Nuclear University MEPhI, 31, Kashirskoe shosse, Moscow, 115409. Russia*

* Corresponding author: Tel. +7 496 524 6267. *E-mail*: kosm@ism.ac.ru

Abstract

Spark plasma sintering of β-SiAlON-based ceramic composites from powders – β-Si_5AlON_7, h-BN, β-SiC, and TiN – prepared by combustion synthesis (**CS**) method was investigated. The process parameters for the CS of ceramic composites containing 0–30 wt. % h-BN, 0–40 wt. % β-SiC, and 0–40 wt. % TiN and exhibiting high relative density (> 95 %) and flexural strength (up to 400 MPa) were optimized.

Keywords

Combustion synthesis; spark plasma sintering; ceramic composites; sialon; boron nitride; titanium nitride; silicon carbide.

Introduction

Solid solutions of general formula $Si_{6-z}Al_zO_zN_{8-z}$ (z = 0.0–4.2) are known for their excellent hardness, strength, and wear/corrosion resistance, which explains their wide use in various engineering applications [1]. The addition of hexagonal boron nitride (**h-BN**), TiN, and SiC to ceramic composites is known to improve their fracture toughness, thermal shock resistance, tribological properties, thermal/electrical conductivity, and machinability. Combustion synthesis (**CS**) is a rapidly developing research area oriented on fast and energy efficient production of high-melting compounds and materials. For example, infiltration-mediated CS in nitrogen is a convenient technique for production of α- and β-SiAlON powders with different phase and elemental composition, particle size, and morphology [2]. Spark plasma sintering (**SPS**) is a newly developed process that uses dc pulses for sample heating. As compared to conventional hot pressing, SPS ensures higher heating rates and very short holding times and has been widely recognized as an effective method for densification of various materials [3]. Therefore, the combination of CS and SPS techniques seems rather promising for R & D of β-SiAlON-based ceramics with widened functionality.

Experimental

Infiltration-mediated CS of β-Si_5AlON_7 and h-BN powders in nitrogen gas was carried out by the following schemes:

$$4.5Si + Al + 0.5SiO_2 + 3.5N_2 \rightarrow \beta\text{-}Si_5AlON_7; \quad (1)$$

$$B + 0.5N_2 \rightarrow BN. \quad (2)$$

Green mixtures also contained some amount of homemade diluents, β-Si_5AlON_7 and h-BN respectively, in order to improve extent of conversion. Combustion was performed in a 2-L reactor at $P(N_2)$ = 8–10 MPa. The CS of β-SiC was carried out by using multistep chemical reactions in the Si–C–N system [4] and TiN fine powders with added NH_4Cl as a gasifying agent [5].

Aliquot amounts of combustion-synthesized raw powders were intermixed in a high-energy planetary steel-ball mill. Ball milling time (800 rpm, ball/mill ratio 10 : 1) was 5 min. Then milled powders were placed into a graphite die and sintered in a Labox 625 SPS facility under vacuum (below 10 Pa). The heating rate was 50 deg/min. The sintered compacts were heated from room temperature to 600 °C without

applied load and then to 1550–1800 °C at a compressive stress of 50 MPa. The compacts were held at a desired temperature for 5 min.

The BET analysis (N_2 sorption) and particle size distribution of used powders was determined with Sorbi-M surface area analyzer and Fritsch Analysette 22 device. The raw powders and sintered compacts were characterized by XRD (DRON-3.0) and SEM (JEOL 6610L). Sample densities were determined by hydrostatic weighing. Flexural strength σ_f was measured for bending a thin disk on a ring base in a testing machine Instron-5966.

Results and discussion

According to XRD results, the raw powders of β-Si_5AlON_7, h-BN, and TiN did not contain impurity phases while β-SiC had trace amounts of Si_3N_4. According to SEM results, all as-synthesized powders appeared largely as agglomerates. Their specific surface was about 1.3 m^2/g for β-Si_5AlON_7 powders, and from 9.8 to 22.8 m^2/g for h-BN, β-SiC, and TiN fine powders. After ball milling, the specific surface increased by a factor of 4–6.

Figures 1 and 2 show relative density ρ_{rel} of sintered samples as a function of temperature *T*. The sintering of pure β-Si_5AlON_7 was accompanied by marked intensification of the consolidation process at temperatures above 1400 °C (curve *1* in Fig. 1) probably due to formation of SiO_2 and Al_2O_3 eutectics. Upon further increase in *T*, relative density of sintered β-Si_5AlON_7 gradually grows up to 87 % (curve *1* in Fig. 2). According to XRD data, pure β-Si_5AlON_7 sintered above 1750 °C exhibits the traces of AlN formed upon thermal decomposition of β-Si_5AlON_7. The addition of h-BN improves the compactibility of sintered powder mixtures. Under compressive stress of 50 MPa at 600 °C, the initial value of ρ_{rel} exceeds 80 % for the compact containing 30 wt. % BN and 60 % for that of pure β-Si_5AlON_7 (Fig. 1). In parallel, an increase in h-BN content suppresses the consolidation processes due to formation of liquid eutectics. At 30 wt. % BN (curve *4* in Fig. 1), the temperature dependence of ρ_{rel} becomes much more aligned. The small flaky h-BN particles are uniformly distributed over the surface of larger β-Si_5AlON_7 particulates. At 30 wt. % BN, the h-BN particles (unwettable with oxide melt) fully separate the β-Si_5AlON_7 particles apart. It is clear that in such systems a contribution from liquid-phase processes to consolidation cannot be important. In case of 10 and 20 wt. % h-BN, the processes associated with formation of liquid eutectics are more or less pronounced, so that high relative density can be attained (curve *3* in Fig. 2). The addition of fine β-SiC and TiN powders worsens the compactibility of sintered powder mixtures under a compressive stress at the initial stage. As a result, the highest value of relative density for sintered ceramic composites containing β-SiC can only be achieved at 1750 °C (curve *2* in Fig. 2). Meanwhile, the addition of TiN powder facilitates the efficiency of sintering above 900 °C and the highest values of ρ_{rel} can be achieved already at 1550 °C (curve *4* in Fig. 2).

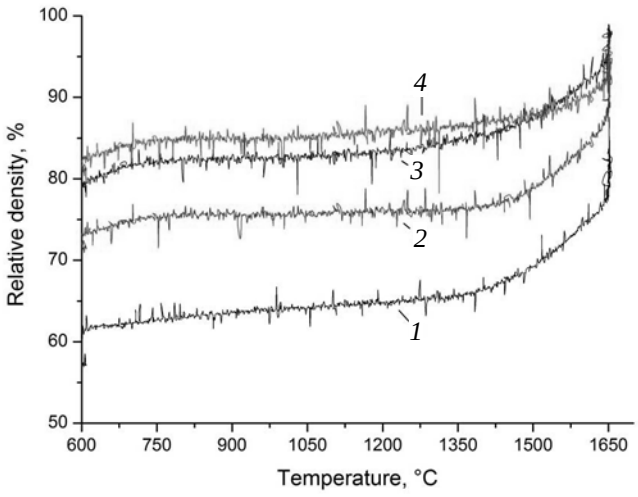

Fig. 1. Relative density ρ_{rel} as a function of temperature *T*:
1 – β-Si_5AlON_7; *2* – β-Si_5AlON_7-BN (10 wt. %) ;
3 – β-Si_5AlON_7-BN (20 wt. %) ; *4* – β-Si_5AlON_7-BN (30 wt. %);
T_{max} = 1650 °C

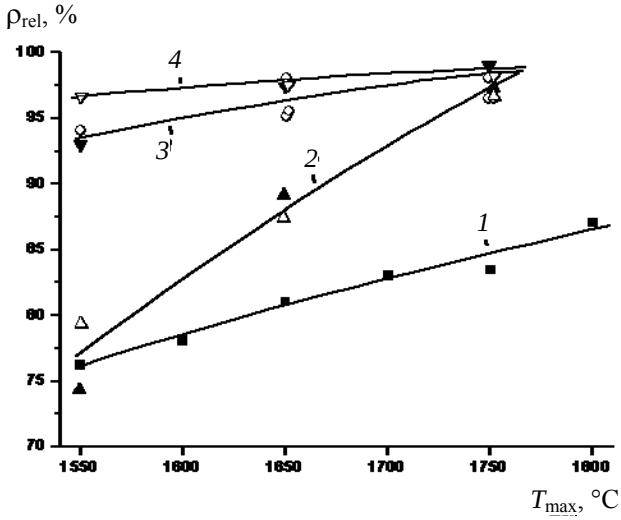

Fig. 2. Relative density ρ_{rel} as a function of T_{max}:
■ – β-Si_5AlON_7 – curve *1*; ○ – β-Si_5AlON_7-BN (10–30 wt. %) – curve *2* ; ▼ – β-Si_5AlON_7-TiN (20 wt. %)-BN (10 wt. %) – curve *3* ; ∇ – β-Si_5AlON_7-TiN (40 wt. %)-BN (10 wt. %) – curve *4*; ▲ – β-Si_5AlON_7-SiC (20 wt. %)-BN (10 wt. %) – curve *2*; Δ – β-Si_5AlON_7-SiC (40 wt. %)-BN (10 wt. %) – curve *2*

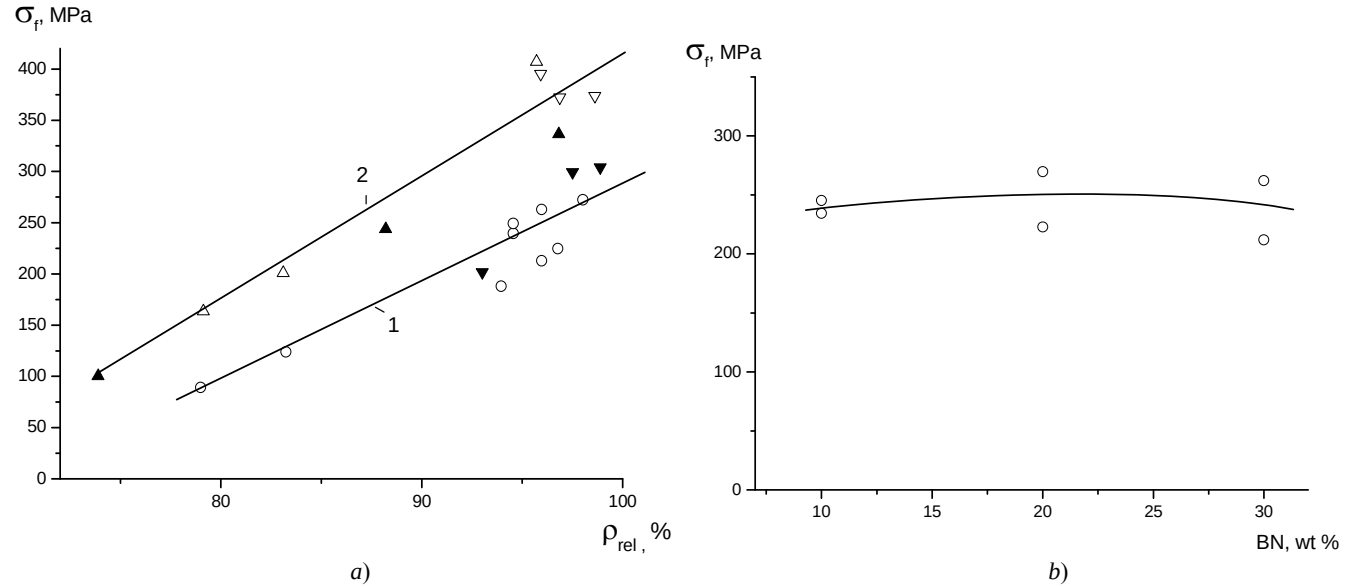

a) *b*)

Fig. 3. Flexural strength σ_f as a function:
a – relative density ρ_{rel} for (○) β-Si_5AlON_7-BN (0–30 wt. %) – curve *1*; ▼ – β-Si_5AlON_7-TiN (20 wt. %)-BN (10 wt. %);
∇ – β-Si_5AlON_7-TiN (40 wt. %)-BN (10 wt. %) – curve *2*; ▲ – β-Si_5AlON_7-SiC (20 wt. %)-BN (10 wt. %);
Δ – β-Si_5AlON_7-SiC (40 wt. %)-BN (10 wt. %) – curve *2*;
b – BN content in β-Si_5AlON_7-BN (10–30 wt. %); ρ_{rel} = 95–98 %

Fig. 3*a* illustrates flexural strength σ_f as a function of ρ_{rel}. Our results well agree with those reported for similar ceramic composites prepared by other techniques [6, 7]. SPS method affords to produce ceramic composites with higher relative density and flexural strength (up to 400 MPa). In our case, the flexural strength of sintered ceramic composites was found to depend on the BN content only slightly (Fig. 3*b*). A marked increase in σ_f (up to 40 %) can be achieved upon replacement of 40 wt. % of relatively coarse β-SiAlON particles in sintered ceramic composites by finer β-SiC and TiN particles (curve *2* in Fig. 3*a*).

Conclusions

High-density β-SiAlON-based ceramic composites can be prepared by fast and energy efficient techniques: CS of raw powder materials and subsequent SPS. Thus obtained ceramics seem promising for fabrication of items for operating in severe conditions of strong thermal shock and in highly corrosive media.

References

1. Ekström T., and Nygren M. SiAlON ceramics. *J. Am. Ceram. Soc.*, 1992, vol. 75, issue 2, pp. 259-276. doi: 10.1111/j.1151-2916.1992.tb08175.x

2. Liu G., Chen K.X., and Li J.T. Combustion Synthesis of SiAlON Ceramic Powders: A Review. *Mater. Manu. Proc.,* 2013, vol. 28, no. 2, pp. 113-125. doi: 10.1080/10426914.2012.718471

3. Munir Z.A., Anselmi-Tamburini U., and Ohyanagi M. The effect of electric field and pressure on the synthesis and consolidation of materials: A review of the spark plasma sintering method. *J. Mater. Sci*., 2006, vol. 41, issue 3, pp. 763-777. doi: 10.1007/s10853-006-6555-2

4. Kata D., Lis J., Pampuch R., and Stroberski L. Preparation of fine powders in the Si–C–N system using SHS method. *Int. J. Self-Propag. High-Temp. Synth.*, 1998, vol. 7, issue 4, pp. 475-486.

5. Zakorzhevskii V.V., Kovalev I.D., and Barinov Yu.N. Self-propagating high-temperature synthesis of titanium nitride with the participation of ammonium chloride. *Inorg. Mater.*, 2017, vol. 53, issue 3, pp. 278-286. doi: 10.1134/S002016851703013X

6. Smirnov K.L. Combustion synthesis of SiAlON-BN hetero-modulus ceramic composites. *Int. J. Self-Propag. High-Temp. Synth.*, 2015, vol. 24, issue 4, pp. 219-225. doi: 10.3103/S1061386215040147

7. Zhang G.-J., Yang J.-F., Ando M., and Ohji T. SiAlON-boron nitride porous composites: In situ synthesis, microstructure, and properties. *Key Eng. Mater.,* 2003, vol. 237, pp. 123-128. doi: 10.4028/www.scientific.net/KEM.237.123

DOI: 10.17277/amt.2018.03.pp.029-036

The SHS of $Y_2Ti_2O_7$-Based Pyrochlore Ceramics

T.V. Barinova*, V.Yu. Barinov, I.D. Kovalev, N.V. Sachkova

Merzhanov Institute of Structural Macrokinetics and Materials Science, Russian Academy of Sciences, 8, Academician Osipyan St., Chernogolovka, Moscow Region, 142432, Russia;

* Corresponding author. Tel.: +7 496 52 463 04. *E-mail*: tbarinova@ism.ac.ru

Abstract

The effect of Fe and ($Al + SiO_2$) additives on the combustion mode, porosity, phase composition and structure of synthesized $Y_2Ti_2O_7$-based pyrochlore ceramic matrices. It is shown that the introduction of Fe powder does not affect the phase composition of the ceramics. The presence of aluminum in the charge led to the formation of phases of $Y_3Al_5O_{12}$ garnet and $YAlO_3$ perovskite. In the presence of the selected additives, combustion of charge billets was in a controlled stationary mode, the ceramic samples retained the shape and dimensions of the charge billet, had a cast structure, but the additives did not significantly reduce the porosity of the resulting ceramics. Ceramics with an open porosity of less than 10 % were obtained by applying an axial force of 0.1–0.3 kN per product after completing the combustion process.

Keywords

SHS ; mineral-like matrices; pyrochlore; high-level wastes.

Introduction

The research is aimed at solving the urgent problem of a closed nuclear fuel cycle – neutralization of high-level wastes (**HLWs**) containing actinides. HLWs with a high content of actinides occur during the fractionation of waste and represent the greatest nuclear threat to the environment. One of the promising approaches to the immobilization of HLWs is their isomorphic inclusion in chemically, mechanically, radiation-resistant mineral-like matrices that prevent the ingress of radionuclides into the environment [1].

This paper is a continuation of studies on the use of the SHS method for the synthesis of mineral-like matrices $Y_2Ti_2O_7$-based pyrochlore composition enriched with zirconium, and intended for immobilization of the actinide-containing fraction of HLWs [2, 3].

In the course of the study, two problems were solved: dispersion of the reaction mass in the combustion process of charge billets at atmospheric pressure and high porosity of by the SHS method ceramics produced without the use of pressing. When burning thermite compounds, the combustion temperature may exceed the melting point of the final products [4]. In this case, combustion is accompanied by a strong spread of the melt and proceeds in an explosive mode. The creation of excess gas pressure (argon, air), a decrease in the caloric content of the mixture due to dilution with oxide additives or introduction of an excess of one of the reagents into the mixture suppress the spread of the melt and transfer the combustion into a controlled stationary regime [5]. In the given combustion conditions, we failed to suppress the dispersion of the reacting mass due to the variation in the composition of the charge, the density and size of the initial billets. Earlier it was shown [3] that with increasing density of charge billets the combustion temperature T_c decreases to 1500–1470 °C. It was possible to produce ceramics that retain the shape of charge billet only with a small load of the burning sample. The combustion in this case was at the limit, as indicated by the layered structure of the product. Therefore, the dilution of the composition of the charge by the introduction of zirconium or titanium oxides to reduce the intensity of the process was not suitable, since the addition of oxides led to a further decrease in T_c. In the proposed study, attempts were made to use iron powder as additives to suppress dispersion. Iron under the investigated conditions did not form chemical compounds with the starting

compounds and combustion products and was included in the ceramic matrix in its free form due to the reduction of Fe_2O_3 iron oxide, used in the preparation of charge compositions as an oxidant. It was expected that due to the low melting point in the combustion conditions, the iron would be in the molten state, increasing the fraction of the liquid phase and contributing to a decrease in porosity. The choice of Fe_2O_3 as an oxidizer for the synthesis of ceramics was associated with the production of matrices having a lower porosity than, for example, MoO_3, under similar conditions [3]. As it is known, ceramics produced by the SHS method have a high porosity. According to the data of [6], high-porous $Y_2Ti_2O_7$-based matrices possess the necessary chemical stability, which significantly exceeds the resistance of glasses. However, it is believed that for the long-term and safe storage of HLWs, the porosity of the synthesized matrices must be reduced. To reduce the porosity, a mixture ($Al + SiO_2$) was introduced into the charge to increase the amount of the liquid phase having a reduced melting point. In addition, the presence of small amounts of aluminum in the composition of the charge should contribute to an increase in T_c due to the interaction with iron and titanium oxides proceeding with considerable heat release [7, 8].

The aim of the study was to investigate the effect of Fe and ($Al + SiO_2$) additives on the combustion regime, porosity, phase composition and structure of synthesized $Y_2Ti_2O_7$-based pyrochlore ceramic matrices enriched with zirconium. Zirconium in pyrochlore was introduced to increase its chemical and radiation resistance [9].

Experimental

Justification of the choice and procedure for calculating the charge compositions for the preparation of $Y_2Ti_{2-x}Zr_xO_7$-based ceramic matrices enriched with zirconium pyrochlore were described in [2, 3].

In the study we used: Ti of PTOM grade, TiO_2 in the form of anatase (c.p.), Y_2O_3 (c.p.), ZrO_2 (c.p.), CaO (c.p.), Fe_2O_3 III (c.p.). The indispensable components of the charge were a mechanical mixture of metal oxides, simulating the composition of real HLWs. The composition of the model mix of waste, %: CeO_2 – 25.0; La_2O_3 – 50.7; ZrO_2 – 19.6; MnO_2 – 3.8; Fe_2O_3 – 0.9. The content of model waste in the batch was 10 wt. %.

On the basis of thermodynamic calculations and experimental data, the following composition of charge (mole) was selected:

$$0.326\ Ti + 0.159Y_2O_3 + 0.102\ ZrO_2 + \\ + 0.028\ CaO + 0.215\ Fe_2O_3 . \quad (1)$$

According to the ratio of Zr and Ti in the composition of the charge, up to 17 % of Ti atoms on Zr should be replaced in the pyrochlore structure, taking into account the introduced HLWs. The starting charge mixture was prepared by mixing in drums with steel balls. Pressing of billets was carried out on a hydraulic press. The charge compositions were pressed in the form of cylinders with a diameter of 30 and 50 mm and an average density of 2.7 g/cm^3. The pressed billets were placed in backfills of coarse-grained quartz, so as to increase the cooling time of the synthesized matrices, to reduce heat losses and to retain the shape in the event of possible melting, and to facilitate the evacuation of gases. The combustion process was initiated from the upper end of the charge billet by local heating through the ignition layer of Ti powder. Further, the combustion process spread like a pattern spontaneously in the form of a combustion wave. After passing the combustion wave, the samples were cooled under natural conditions. The SHS resulted in production of matrixes in the form of cylinders of dark gray color.

The combustion temperature T_c was determined by the thermoelectric method with the help of tungsten-rhenium thermocouples (BP-5/20) with a diameter of 200 μm. Thermocouples were installed in the center of charge billets at a distance of 5 mm from the bottom end. To measure T_c, billets with a diameter and height of 15–18 mm were used. The measurement error was 50 °C [10].

The open porosity was determined by standard methods.

The XRD was carried out on a DRON-3M ($Cu–K_\alpha$ cathode) installation. The investigation of the microstructure and local elemental analysis of the surface of ground samples were carried out using an ultra-high resolution field-emission scanning electron microscope ULTRA plus (Germany, Karl Zeiss).

Results and discussion

Ceramics sample No. 1

The charge composition No. 1 was prepared by adding 5 wt. % of Fe powder to the starting composition (1). After the SHS, no dispersion was observed, the combustion products were produced in the form of cylindrical blocks completely replicating the shape and dimensions of the initial charge billets,

while retaining the angles of the end surfaces. The samples of the products looked dense and slightly porous.

When measuring T_c of the initial charge composition (1) containing 10 % of HLWs, a value of 1500 °C was obtained, and for the composition No. 1, T_c was 1470–1480 °C. From a comparison of the obtained values of T_c, it can be seen that the addition of 5 % iron led to a decrease in T_c by 20–30 °C, which is comparable with the measurement error.

Fig. 1 shows the diffractogram of a ceramic sample No. 1. According to the XRD data (Fig. 1), the combustion product is formed by $Y_2(Ti_{0.85}Zr_{0.15})_2O_7$ pyrochlore phases, $CaTiO_3$ perovskite and metallic Fe. In the structure of pyrochlore, 15 % of Ti atoms on Zr are replaced, which is close to the ratio of the content of these elements in the charge.

The investigation of the microstructure showed that the combustion product had a cast, but porous structure. The pores were very small, and permeated the entire product, leaving practically no dense area. To illustrate Fig. 2*a–c* show photographs of the microstructure of the combustion product at various magnifications. A feature of the product obtained is the presence of two types of iron precipitates – iron, reduced from oxide in the form of fine precipitates with a size of not more than 2 μm, and iron, introduced in the form of a powder. The latter occupies rather extensive areas and is separated from the main mass of the matrix by the boundary formed by iron oxide. Obviously, initially the particles of the powder of the iron used were covered with an oxide film that was not recovered during the synthesis. In Fig. 2*b* in the upper part of the photo a particle of iron separated from the bulk of the ceramic by a dark strip of oxide film is

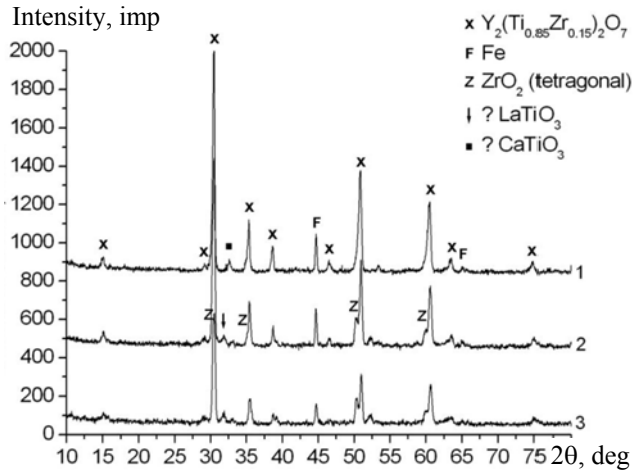

Fig. 1. Diffractograms of ceramics produced by combustion of compositions No. 1, 2, 3

shown. Fig. 2*c* clearly shows three phase components of the oxide phase, which are in close contact. According to the analysis, the oxide phase is based on rounded pyrochlore grains, which form microcrystalline aggregates of gray color (Fig. 2*c*). A feature of the obtained structure is also the absence of pyrochlore grains with a ring structure, which was observed in all our previous studies, regardless of which oxide was chosen as the oxidizer – Fe_2O_3 or MoO_3. There are no interlayers of other phases between the pyrochlore grains in microcrystalline aggregates. It can be seen that the pyrochlore grains, as well as the perovskite grains, differ in color, indicating variations in their composition. Thus, the composition of pyrochlore at point *5* is more enriched in zirconium than at point *6*. Perovskite grains located in close intergrowth with pyrochlore have a light gray color.

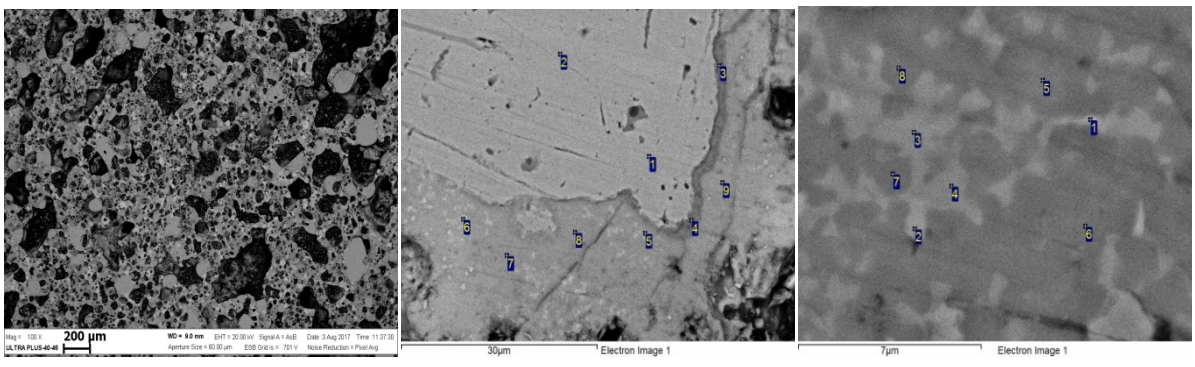

a) *b*) *c*)

Fig. 2. Microstructure of the product of composition No. 1 at different magnifications:
a – × 100; *b* – × 5000; *c* – × 20 000;
b: *1*, *2* – Fe; *3*, *4* – Fe oxide, $CaTiO_3$ perovskite; *5*, *6* – $CaTiO_3$ perovskite; *7 – 9* –$Y_2Ti_2O_7$ pyroclore;
c: *1* – Fe; *2* – $LaTiO_3$ perovskite; *3*, *4* –$CaTiO_3$ perovskite; *5 – 8* – pyroclore

Distribution of elements (at. %) in Fig. 2*b*

Spectrum	O	Al	Si	Ca	Ti	Mn	Fe	Y	Zr	La	Ce
1	3.4	1.8	0.1	0.0	0.5	0.0	93.8	0.0	0.1	0.1	0.1
2	2.8	2.2	0.4	0.1	0.0	0.0	93.5	0.2	0.3	0.2	0.2
3	62.2	0.7	0.1	0.1	1.8	0.2	32.5	1.7	0.4	0.1	0.1
4	60.7	1.0	0.0	0.1	0.6	0.0	36.9	0.4	0.0	0.0	0.1
5	67.1	0.9	0.5	1.8	11.5	0.2	4.1	9.1	0.8	2.8	1.1
6	41.3	1.6	0.7	0.9	5.7	0.0	40.8	5.7	1.3	1.4	0.6
7	66.9	0.6	0.9	0.8	11.8	0.2	2.3	13.5	1.8	0.6	0.5
8	65.1	0.6	0.6	0.8	13.5	0.1	1.6	14.8	1.4	0.8	0.5
9	66.0	0.7	0.8	0.6	13.5	0.0	0.9	14.6	1.7	0.6	0.5

Distribution of elements (at. %) in Fig. 2*c*

Spectrum	O	Ca	Ti	Mn	Fe	Y	Zr	La	Ce
1	36.7	0.3	6.3	0.0	46.0	8.8	1.1	0.5	0.2
2	69.6	1.0	9.2	0.4	5.0	11.4	0.6	1.8	1.1
3	65.2	3.1	11.3	0.2	5.9	9.8	0.5	2.7	1.4
4	66.9	2.2	11.3	0.4	4.4	10.8	0.7	2.1	1.2
5	67.6	0.5	13.1	0.1	1.5	14.3	1.3	1.0	0.8
6	69.2	0.5	12.7	0.0	1.1	14.4	1.0	0.6	0.5
7	66.8	0.9	13.1	0.1	3.5	13.1	0.9	1.0	0.7
8	69.4	0.6	12.8	0.0	1.5	13.6	0.7	1.0	0.6

Both phases are chemically solid solutions of several components, including rare-earth elements (**REEs**) from the model mixture of HLWs. The content of REEs in perovskite phases was much higher than in pyrochlore.

The fine grain size of the phase constituents of ceramics No. 1 and the ceramics studied below does not allow us to establish their exact composition due to the capture of neighboring regions of the matrix by the electronic probe, which makes it difficult to calculate the real formulas of the phases formed.

Ceramics sample No. 2

The structure of titanate pyrochlore is stable with a content of up to 30 % zirconium in its lattice [11], and according to XRD data, 15 % of Ti atoms on Zr are replaced in the structure of pyrochlore as a result of synthesis. To increase the share of substitution, addition of 5 mass.% of ZrO_2 was introduced into the composition of charge No. 1, which should lead to an increase in the chemical and radiation resistance of pyrochlore. Also, 4 % of the mixture ($Al + SiO_2$) was introduced into the charge mix, while the Fe fraction decreased to 2.5 % by weight. The selection of the composition was carried out experimentally.

Fig. 1 shows the diffraction pattern of product No. 2. Five phases can be distinguished in the product: $Y_2(Ti_{0.85}Zr_{0.15})_2O_7$ pyrochlore, $CaTiO_3$ perovskites and $LaTiO_3$, ZrO_2 and Fe. According to the XRD data, the amount of zirconium in the pyrochlore structure due to the additional addition of ZrO_2 did not increase, while ZrO_2 remained in the combustion product as an independent phase.

A study of the structure showed that the product was porous; the pores were larger than in sample No. 1. Iron was represented by two types of excreta: large secretions surrounded by a dark border of iron oxide belonging to the introduced gland and small, not exceeding 2 μm round precipitates belonging to the reduced iron. There were also large iron deposits of regular round shape, around which pores were formed.

The pyrochlore grains had a rounded shape and a weakly expressed annular structure – a dark center and a lighter border region, and separated from each other by phase interlayers of a darker color. The dark-colored phase can belong to the perovskite $YAlO_3$. Perovskite grains contained a higher percentage of rare earth elements than pyrochlore.

Fig. 3*c* shows a section of the ceramic where the region with unreacted Y_2O_3 is visible (point *1*). A dense ring of the gray phase is formed around Y_2O_3. It is possible that the gray ring belongs to the $YAlO_3$ alumium yttrium perovskite, in which a high percentage of rare-earth elements and Si was noted.

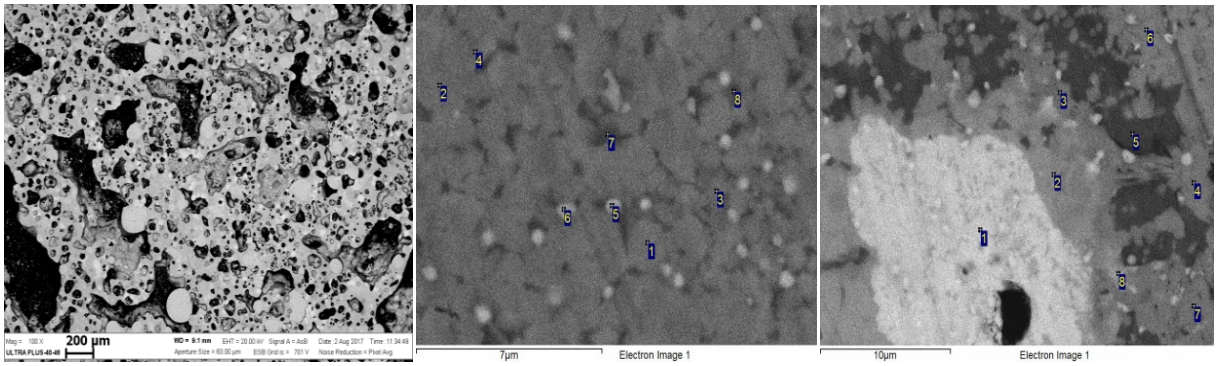

a) *b*) *c*)

Fig. 3. Microstructure of the product of composition No. 2 at different magnifications:
a – × 100; *b* – × 5000; *c* – × 20 000;
b: *1 – 4* –Y_2Ti_2O7 pyrochlore; *5*, *6* – Fe; *7*, *8* –$YAlO_3$ perovskite;
c: *1* – Y_2O_3; *2*, *8* – $YAlO_3$ perovskite; *3*, *4*, *6*, *7* – YAlO3 pyrochlore; *5* – гранат$Y_3Al_5O_{12}$ garnet

Distribution of elements (at. %) in Fig. 3*b*

Spectrum	O	Al	Si	Ca	Ti	Mn	Fe	Y	Zr	La	Ce
1	67.4	2.2	1.1	0.5	9.9	0.0	0.5	13.1	3.9	0.6	0.7
2	66.4	2.2	1.2	0.4	10.7	0.1	0.3	14.1	3.4	0.7	0.5
3	70.0	3.5	1.2	0.5	8.9	0.0	0.7	9.9	4.4	0.3	0.5
4	63.1	2.9	1.4	0.4	11.5	0.1	0.8	14.5	3.3	1.0	0.8
5	53.6	3.7	1.7	0.4	7.1	0.4	18.8	10.1	2.6	0.9	0.6
6	49.0	3.2	1.5	0.4	8.3	0.1	20.6	12.0	2.9	0.9	0.8
7	66.9	6.5	3.6	1.2	6.1	0.2	1.3	8.8	2.2	1.9	1.2
8	65.4	5.5	2.9	1.1	7.0	0.3	2.4	9.4	3.1	1.6	1.1

Distribution of elements (at. %) in Fig. 3*c*

Spectrum	O	Al	Si	Ca	Ti	Mn	Fe	Y	Zr	La	Ce
1	62.7	0.8	1.5	0.3	0.3	0.0	0.8	32.9	0.1	0.3	0.0
2	65.2	2.0	8.7	1.1	2.3	0.2	0.2	16.6	0.8	1.7	1.0
3	64.4	3.1	1.4	0.5	11.4	0.1	1.5	13.9	1.9	0.7	0.7
4	68.2	1.5	1.4	0.3	10.9	0.0	0.1	14.3	2.2	0.6	0.5
5	66.0	16.7	1.2	0.6	1.8	0.2	0.4	12.6	0.5	0.0	0.0
6	66.0	1.8	1.6	0.5	11.2	0.3	0.4	13.2	2.9	1.0	0.9
7	65.6	2.5	2.4	0.4	11.6	0.0	0.6	12.8	1.5	1.5	1.0
8	66.7	2.5	7.5	2.1	3.5	0.3	1.2	10.9	0.9	2.5	1.7

Then comes the ring, consisting of a dark color phase (point *5*), it can belong to the $Y_3Al_5O_{12}$ alumina garnet. The formation of the garnet phase under synthesis conditions is possible at a temperature of 1250–1400 °C according to the following reaction [12]:

$$3YAlO_3 + Al_2O_3 \rightarrow Y_3Al_5O_{12}.$$

Judging from the analysis, the $Y_3Al_5O_{12}$ phase contained the minimum amount of lanthanum and cerium, compared with the phases of perovskites (points *2*, *8*) and pyrochlore (points *3*, *4*, *6*, *7*).

The investigation of the structure showed that the phase of the garnet was distributed in the sample of the ceramic not uniformly, but forms microcrystalline aggregates consisting of intergrown grains without interlayers of other phases between them.

To prove the formation of $Y_3Al_5O_{12}$, the amount of Al in the charge was increased to 4 %. The interpretation of the diffractogram of the synthesized ceramics in this case in Fig. 4 confirmed the formation of the $Y_3Al_5O_{12}$ phase.

Ceramics sample No. 3

This composition of charge differs from the previous one by the absence of Fe powder in the charge. The measurement of T_c for a given composition showed values of 1550–1580 °C.

According to the XRD data (Fig. 1), the phase composition of the obtained product was the same as for composition No. 2. The structure of this product differed from the others in the presence of rare but large pores. Reduced iron in some areas formed large discharge with a size of more than 200 microns,

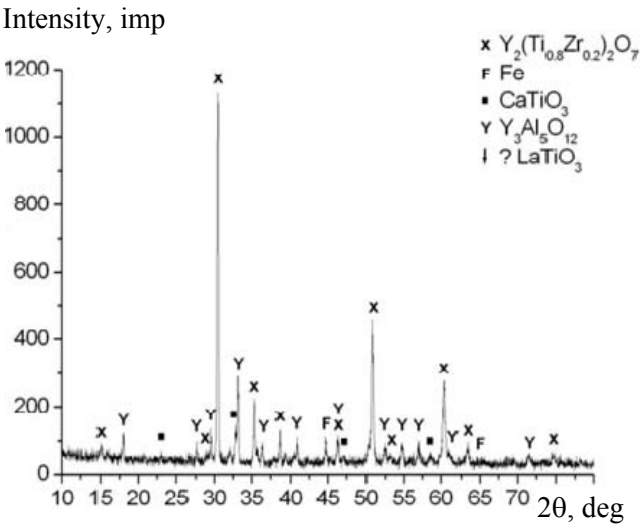

Fig. 4. Diffractogram of the ceramics sample No. 4

indicating a higher T_c in this composition compared with the previous ones (Fig. 5*b*). In Fig. 5*b* the microstructure of the region of the matrix consisting of the following phases is represented: pyrochlore, $LaTiO_3$ perovskite, ZrO_2 and Fe. Probably points *7* and *8* belong to the phase of the grenade. The section of the matrix with a larger magnification is shown in Fig. 5*c*. The maximum amount of lanthanum and cerium is contained in the perovskite phase (points *3* and *4*), the minimum amount in the pyrochlore phase.

In all three compositions, the additives were added in excess of the stoichiometry of the original composition according to equation (1). With an increase in the content of iron oxide composition No. 3 in the charge in the amount necessary for the reaction with aluminum, the $Fe_2Al_2O_4$ phase was formed in the combustion products.

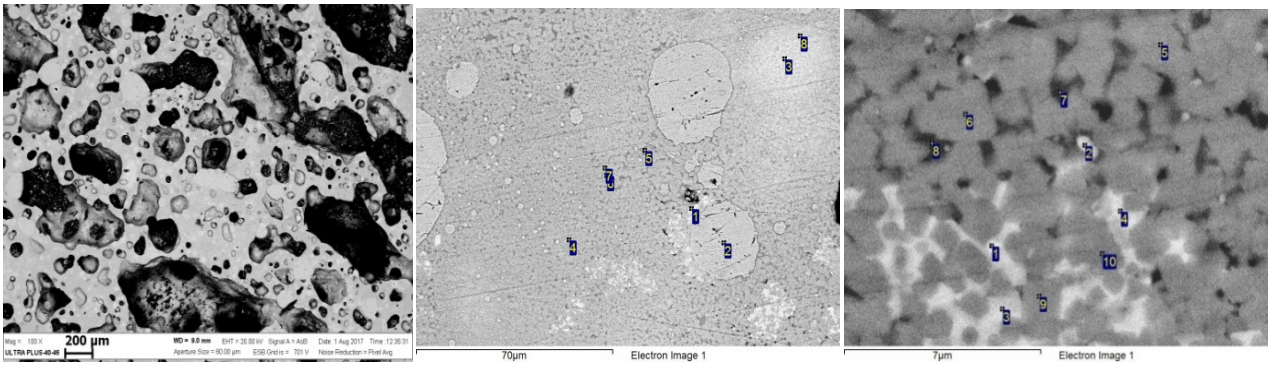

a) *b*) *c*)

Fig. 5. Microstructure of the product of composition No. 3 at different magnifications:
a – × 100; *b* – × 5000; *c* – × 20 000;
b: *1*, *5* – $LaTiO_3$ perovskite; *2* – Fe; *3*, *8* – ZrO_2 region; *4*, *7* – $Y_2Ti_2O_7$ pyrochlore
(point *6* is not identified because it coincides with point *7*);
c: *1*, *2* – Fe; *3*, *4* – $LaTiO_3$ perovskite; *5*, *6*, *9*, *10* – $Y_2Ti_2O_7$ pyrochlore; *7*, *8* – $Y_3Al_5O_{12}$ garnet

Distribution of elements (at. %) in Fig. 5*c*

Spectrum	O	Al	Si	Ca	Ti	Mn	Fe	Y	Zr	La	Ce
1	42.2	2.6	0.8	0.8	9.7		30.3	8.2	1.3	1.9	2.0
2	46.8	3.8	1.9	0.4	9.2		23.2	10.8	2.1	0.8	0.9
3	65.0	2.6	0.5	1.3	13.4	–	0.5	9.2	1.6	3.2	2.6
4	66.2	3.7	0.5	1.4	12.0		1.0	7.2	1.3	3.5	3.1
5	65.2	1.9	1.4	0.5	12.3		0.5	13.4	3.0	0.7	1.1
6	66.5	1.6	1.2	0.4	12.0		0.7	13.4	2.6	0.5	0.8
7	68.8	5.0	3.0	0.6	8.0	0.1	1.2	8.8	1.7	1.5	1.2
8	67.0	6.8	3.7	1.0	7.1	0.1	2.0	7.4	1.6	1.8	1.5
9	64.8	1.2	0.8	0.4	13.5	–	1.0	13.3	2.7	0.9	1.3
10	65.3	1.6	0.7	0.6	13.7		0.4	12.9	2.4	0.9	1.4

It is shown that the open porosity of the first two ceramics was 40 %. Below are the values for the last composition – 30 %. To produce ceramics with low porosity, after complete passage of the synthesis, the hot combustion products were manually sealed. When a single axial force of 0.1–0.3 kN was applied with the help of a piston made of BN, they were significantly compacted. The values of open porosity were less than 10 %. Fig. 6 shows the structure of the ceramic after sealing in a hot state. For comparison: using the SHS compaction method (pressure pressing on the non-heated combustion product was 100 MPa), the open porosities of synthesized pyrochlore-based ceramics were 2.4–4.0 % [13].

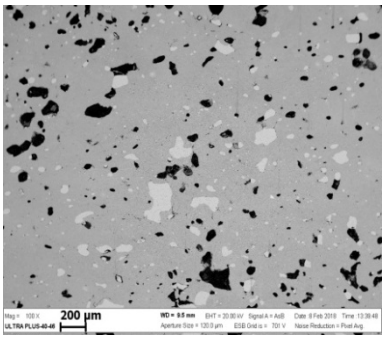

Fig. 6. Microstructure of the ceramic sample after compaction (open porosity 8 %)

Fig. 7. Photo of a typical sample of ceramics

Fig. 7 shows a photo of a typical sample of ceramics produced by SHS without applying pressure.

Conclusion

The effect of Fe additives and mixtures ($Al+SiO_2$) on combustion in the SHS regime in the air of pressed batch blanks on the basis of the composition $CaO + Y_2O_3 + ZrO_2 + Ti + Fe_2O_3$ was studied. It is shown that additives added to the charge contribute to the conversion of the combustion reaction to a controlled stationary regime. The produced samples of ceramics completely retain the shape and dimensions of the initial charge billets. However, the resulting ceramic had a high porosity. It was possible to obtain ceramics with open porosity values of less than 10% only when the load applied to combustion products in the hot state.

Acknowledgments

The research was financially supported by the Russian Foundation for Basic Research (*project no. 16-53-00084*). *The work was performed using a set of modern scientific instruments available for multiple accesses at the ISMAN Center of Shared Services.*

References

1. Stefanovsky S.V., Yudintsev S.V. Titanates, zirconates, aluminates and ferrites as waste forms for actinide immobilization. *Russian Chemical Reviews,* 2016, vol. 85(9), p. 962. doi: org/10.1070/RCR4606

2. Barinova T.V., Podbolotov K.B., Borovinskaya I.P., Shchukin A.S. Self-propagating high-temperature synthesis

of ceramic matrices for immobilization of actinide-containing wastes. *Radiochemistry*, 2014, vol. 56, issue 5, pp. 554-559. doi: 10.1134/S1066362214050178.

3. Barinova T.V., Borovinskaya I.P., Barinov V.Yu., Kovalev I.D., and Podbolotov K.B. SHS of $Y_2Ti_2O_7$-Based Mineral-Like Ceramics: Influence of Green Density, *Int. J. Self-Prop. High-Temp. Synth.*, 2017, vol. 26, issue 2, pp.119-123. doi: 10.3103/S1061386217020030.

4. Tarakanov A. Yu., Shiryaev A. A., Yukhvid V.I. Fazovye prevrashheniya v vysokokalorijnykh geterogennykh sistemakh okisel – vosstanovitel' – nemetall [Phase transformations in high-caloric heterogeneous oxide-reduction-non-metal systems]. *FGV*, 1991, vol. 27, issue 3, pp. 68-74. (Rus)

5. Gorshkov V.A., Sanin V.N., Yukhvid V.I., Modelirovanie kriticheskikh uslovij v rabochej yachejke atomnogo reaktora s pomoshh'yu goreniya vysokoehnergeticheskikh SVS-sistem [Modeling of Critical Conditions in a Fuel Cell of a Nuclear Reactor Based on Combustion of Energetic SHS Systems]. *FGV*, 2014, vol. 50, issue 4, pp.42-4. (Rus)

6. Vinokurov, S.E., Kulyako, Yu.M., Perevalov, S.A., Myasoedov, B.E., Immobilisation of actinides in pyrochlore-type matrices produced by self-propagating high-temperature synthesis, *C. R. Acad. Sci., Ser. Chimie*, 2007, issue. 10, pp.1128-1130. doi: 10.1016/j.crci.2007.04.011

7. Kobyakov V.P., Barinova T.V., Mashkinov L.B., and Sichinava M.A. Heat Release in the Preparation of TiC–Al2O3 Ceramics. *Inorganic Materials*, vol. 48, issue 5, pp. 549-551. doi: 10.1134/S0020168512040061.

8. Chernenko E.V, Afanas'eva L.F., Lebedeva V.A., Rozenband V.I., Vosplamenyaemost' smesej okislov metallov s alyuminiem [The flammability of mixtures of metal oxides with aluminum]. *FGV*, 1988, vol. 24, issue 6, pp.1-3. (Rus)

9. Wang S.X., Begg B.D., Wang L.M., Ewing, R.C., Weber W.J., and Govidan Kutty K.V. Radiation stability of gadolinium zirconate: A waste form for plutonium disposition, *J. Mater. Res*., 1999, vol. 14, no. 12, pp. 4470-4473.

10. Maslov V.M., Borovinskaya I.P., Merzhanov A.G. Ehksperimental'noe opredelenie maksimal'nykh temperatur protsessov samorasprostranyayushhegosya vysokotempera-turnogo sinteza [Experimental determination of the maximum temperatures of processes of self-propagating high-temperature synthesis]. *FGV*, 1978, issue 5, pp. 79-85. (Rus)

11. Yudintsev S.V., Stefanovskii S.V., and Chou S., Phase formations in Ca–Ce–Ti–Zr–(Hf)–O systems and optimization of synthesis conditions for pyrochlore based actinide matrices, *Fiz. Khim. Obrab. Mater.*, 2008, no. 3, pp. 70-80.

12. Nejman A.YA., Tkachenko E.V., Kvichko L.A., Kotok L.A. Usloviya i makromekhanizm tvyordofaznogo sinteza alyuminatov ittriya [Conditions and macromechanism of solid-phase synthesis of yttrium aluminates]. *Zhurnal neorganicheskoj khimii*, 1980, vol.25, issue 9, pp. 2340-2345. (Rus)

13. Barinova T.V., Borovinskaya I.P., Ratnikov V.I., Ignat'eva T.I., Belikova A.F. Samorasprostranyayushhijsya vysokotemperaturnyj sintez (SVS) keramiki na osnove pirokhlora dlya immobilizatsii dolgozhivushhikh vysokoaktivnykh otkhodov [Self-propagating high-temperature synthesis (SHS) of pyrochlore-based ceramics for the immobilization of long-lived high-level waste]. *Radiokhimiya*, 2013, vol. 55, issue 6, pp. 539-543. (Rus)

DOI: 10.17277/amt.2018.03.pp.037-041

Basic Models of Volume Synthesis of Ti-Based Composites

A.G. Knyazeva

Institute of Strength Physics and Material Science of Siberian Branch of Russian Academy of Sciences, 2/4, Academichesky Avenue, Tomsk, 634055, Russia;
National Research Tomsk Polytechnic University, 30, Lenin Avenue, Tomsk, 634050, Russia

* Corresponding author. Tel.: +7 3822 286 831. *E-mail*: anna@ispms.ru

Abstract

The paper demonstrates the capability of the volume synthesis models for the prognosis of final composition. The simplest models for the titanium-based composites synthesis are presented. The melting with the gradual formation of liquid phase in the given temperature interval is taken into account. The controlling for the process is carried out at the expense of the heating rate change, variation of the initial composition of the mixture. The models were realized numerically. It was demonstrated that the irreversible final phase composition was obtained for all situations.

Keywords

Composite synthesis; numerical modeling; detailed kinetics; irreversible composition.

Introduction

SHS–methods can be used in composite synthesis [1–5]. The volume synthesis or the synthesis in the explosion mode obeys some preference in comparison with the mode of layerwise combustion, since, for this mode, the best homogenization of synthesized product is observed and it is possible to control the process of changing the conditions of the thermal contact between the reacting system and the environment and between the reacting system and the heater. This process can be controllable also when the initial mixture composition is varied, the inert particles are used as admixtures; the heating rate and the heating method are changed; the external mechanical loading is applied [6–10]. In various synthesis methods, when thermal explosion mode is realized, the reactions can proceed in various ways depending on the equipment and are accompanied by the high heat release that can decrease due to inert admixtures or non-stoichiometric initial composition. The final composition of the synthesis product turns out irreversible and depends on numerous factors. The qualitative physical regularities were described on the basis of the known classical models [11]. The models of thermal explosion based on the reactive cell concept are very popular [12, 13]. However, the irreversible conditions typical for thermal explosion do not agree with the suggested sequence of chemical stages. To develop the models to predict the irreversible composition of the product, various synthesis conditions were analyzed and a series of models was suggested taking into account the staging of the conversion.

Methods and materials

The titanium-based composites synthesized from non-stoichiometric mixtures Ti + C, B, Si and (Ti +Al) + C, B, Si with titanium excess were chosen for the investigation. For example, in the first case, it is expected that the composites Ti + TiC; $\mathrm{Ti} + \mathrm{TiB_2}$ and $\mathrm{Ti} + \mathrm{Ti_5Si_3}$ will be obtained. The ideal summary reaction schemes for first of them

$$\text{Reagent} \rightarrow \text{Product} \qquad (1)$$

or

$$(x + y)\mathrm{Ti} + y\mathrm{C} \rightarrow y\mathrm{TiC} + x\mathrm{Ti}$$

can be complicated at the cost of taking into account the solid solution Ti + C and non-stoichiometric carbide $\mathrm{Ti}_a\mathrm{C}_b$ formation that corresponds to broad homogeneity area on the state diagram Ti–C.

A more complex reaction scheme will include the reactions with irreversible products [14]:

$$\mathrm{Ti} + \mathrm{C} \rightarrow \mathrm{TiC};$$
$$2\mathrm{Ti} + \mathrm{C} \rightarrow \mathrm{Ti_2C};$$
$$\mathrm{Ti} + \mathrm{TiC} \leftrightarrow \mathrm{Ti_2C};$$
$$\mathrm{Ti} + 2\mathrm{C} \rightarrow \mathrm{TiC_2}; \qquad (2)$$
$$\mathrm{TiC} + \mathrm{Ti_2C} \leftrightarrow \mathrm{Ti_3C_2};$$
$$\mathrm{Ti} + \mathrm{C} + \mathrm{Ti_2C} \rightarrow \mathrm{Ti_3C_2};$$
$$\mathrm{TiC_2} + \mathrm{Ti} \rightarrow 2\mathrm{TiC}.$$

Aluminum addition complicates the reaction scheme. We should add the reactions

$$\mathrm{Ti} + \mathrm{Al} \rightarrow \mathrm{TiAl};$$
$$3\mathrm{Ti} + \mathrm{Al} \rightarrow \mathrm{Ti_3Al};$$
$$\mathrm{Ti} + 3\mathrm{Al} \rightarrow \mathrm{TiAl_3};$$
$$\mathrm{TiAl} + 2\mathrm{Ti} \leftrightarrow \mathrm{Ti_3Al};$$
$$\mathrm{TiAl} + 2\mathrm{Al} \leftrightarrow \mathrm{TiAl_3};$$
$$\mathrm{TiAl_3} + 2\mathrm{Ti} \rightarrow 3\mathrm{TiAl};$$
$$4\mathrm{Al} + 3\mathrm{C} \rightarrow \mathrm{Al_4C_3};$$
$$2\mathrm{Ti} + \mathrm{Al} + \mathrm{C} \rightarrow \mathrm{Ti_2AlC};$$
$$3\mathrm{Ti} + \mathrm{Al} + \mathrm{C} \rightarrow \mathrm{Ti_3AlC};$$
$$\mathrm{TiAl} + \mathrm{TiC} \rightarrow \mathrm{Ti_2AlC}$$

to the previous scheme. The reaction rates depend on concentrations correspondingly to the mass action law. However, it is known that for the reactions with solid substances participation, the diffusion is the limiting stage determining the reaction rates. Because the spatial scale where the diffusion occurs (it is the level of individual grains, particles and interfaces between them) is much smaller than the heat scale, the simplifications are inevitable. We believe that micro scale processes are taken into account in the activation energies evaluation and in kinetic functions. The reaction retardation by a solid product gets the reflection in a special multiplier for each reaction rate

$$f = \exp(-s\eta_s)(\eta_0 + \eta_s)^{-p},$$

where η_s is the part of solid products; s, p are retardation parameters. The part of solid products has been determined in the melting temperature interval for the reacting mixture. The modification of kinetic functions is based on the results [15]. Formal-kinetic parameters have been found based on chemical thermodynamics. Activation energies have been proved using the known data for diffusion coefficients. The qualitative behavior of kinetic equation's system depends on the dynamics of the temperature change determined by the experimental conditions. When the temperature distribution along the specimen, the thickness of chamber walls, and mechanical loading conditions were taken into account, we came to more complex mathematical models. As a result, we obtained the different models of solid-phase reactors [16–21]. All models were realized numerically.

Examples

The simplest model [16] corresponds to the pressing of small size when the temperature distribution can be neglected. In this approximation, only one reaction (1) takes place that corresponds to the summary reaction scheme. We believe that the melting is observed in some temperature interval between the solidus and liquidus temperatures, where the liquid phase part changes with some kinetic law. The pressing was heated by radiant heat from vacuum chamber walls (from the heater). The heating rate was controlled by heater temperature T_W that changes corresponding to given low. For illustration linear low is taken $T_W = T_0 + at$. The heating is switched when wall temperature achieves to given value Activation energy and chemical heat release is $E_a = 2.1 \cdot 10^5$ J/mol; $Q_0 = 1.73 \cdot 10^4$ J/cm^3. Strong retardation of the reaction by reaction product is assumed for $s_0 = 10$. The numerical experiment showed the reaction does not complete during given time that connects with the heat losses by various physical mechanisms and with reaction retardation. The thermal explosion mode is feasible additionally to slow down the conversion. Fig. 1 illustrates the dynamics of the synthesis process. Critical wall temperature T_W^* exists, after which the thermal explosion realizes. For example, for volume part of carbon in the initial powder mixture $\xi = 0.2$, when wall temperature growths to 2480 K, one can see the specimen temperature behavior similar to thermal explosion (Fig. 1*a*) with conversion level near to 0.6 (Fig. 1*b*). Reaction goes basically in liquid phase that exists during long time (Fig. 1*c*). If the wall temperature growths to 2475 K (Fig. 2), the reaction goes slowly without temperature excursion. The part of liquid phase is less then in previous case. For $T_W = 2400$ the reaction proceeds very slowly in solid phase (this is not shown in pictures).

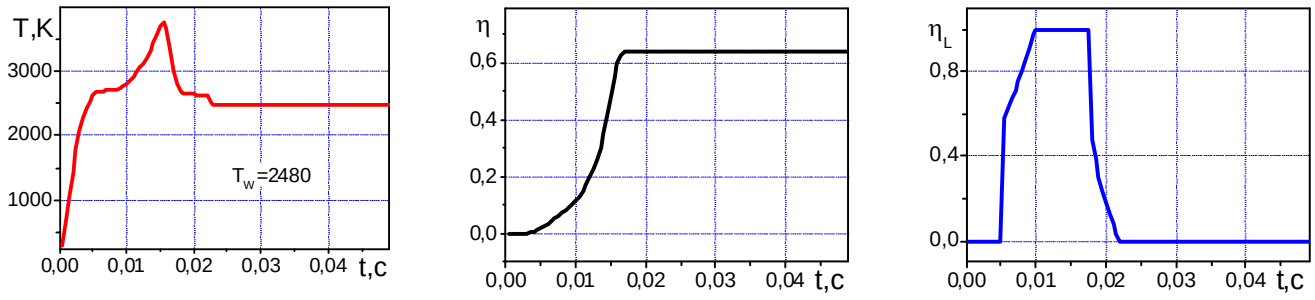

a) *b*) *c*)

Fig. 1. Dynamics of composite T–TiC synthesis:
a – temperature; *b* – conversion level; *c* – part of liquid phase versus the time, T_W = 2480

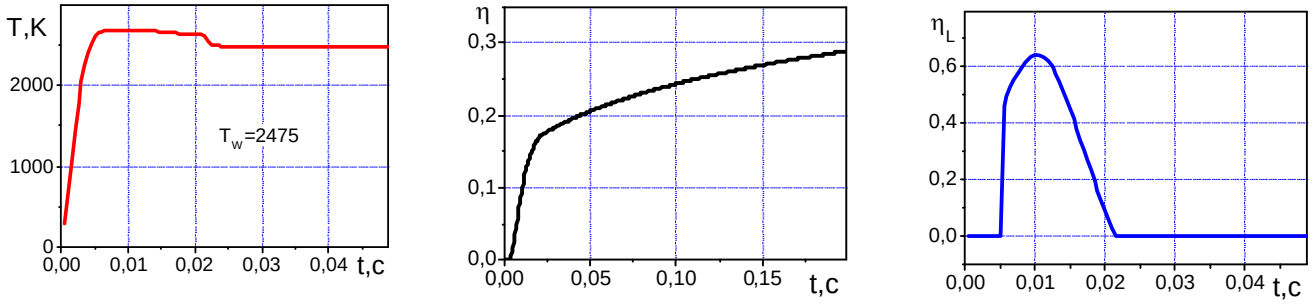

a) *b*) *c*)

Fig. 2. Dynamics of composite T–TiC synthesis:
a – temperature; *b* – conversion level; *c* – part of liquid phase versus the time, T_W = 2475

The final composition varies depending on temperature T_W.

The second example illustrates the capability of the model with detailed reaction scheme (2). In this case we have the heat balance equation in the form similar to [6]. However, the overall chemical heat release includes the heats from nine reactions. The reaction retardation depends on the overall concentration of phases. To find the mass concentrations the kinetic equations are necessary

$$\rho \frac{dy_k}{dt} = \omega_k ,$$

where source terms, kg/(m^{3}s), takes the worm

$$\omega_k = \sum_{i=1}^{9} \nu_{ki} m_k \varphi_i .$$

Here ν_{ki} are stoichiometric coefficient of k species in the reaction i; $y_k = \rho_k / \rho_s$ are mass concentrations, $\rho_k = \eta_k m_k$, $\rho_s = \sum_{(i)} \rho_i m_i$, η_k are molar concentrations. If porosity evolution is taken into account, some kinetic equation should be added to the model [16, 21]. At the initial time moment, we have the initial irreversible composition and initial porosity.

The problem is solved numerically. The Euler's method is used. The result depends on the stages that are taken into account, heating and cooling rates, and on the composition of initial mixture.

Fig. 3 illustrates the dynamics typical for the thermal explosion. Only three reactions are included in calculations: $Ti + C \rightarrow TiC$; $Ti + TiC \rightarrow Ti_2C$; $Ti + C + Ti_2C \rightarrow Ti_3C_2$. It is assumed that external heating is ceased, when chemical reactions accelerate, and then the Newton heat exchange continues with the environment with temperature $T_e = T_W$ reached to this time. The initial composition is $y_{Ti} = 0.8$ and $y_C = 0.2$ that corresponds to equal molar concentrations. It was found, the higher the wall temperature rate, the more the temperature near explosion time. The Liquid phase exists for a short time when the reaction rates are maximal. The final composition is the same for different heating rate. We see the presence in the product TiC, Ti_2C, Ti_3C_2. The last phase concentration is very small. All carbides can be identified in experiment as non-stoichiometric carbides.

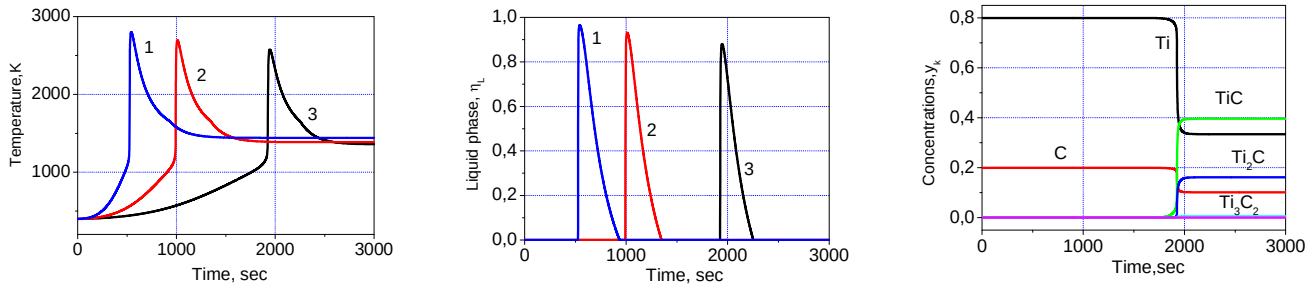

a) *b*) *c*)

Fig. 3. Dynamics of composite synthesis.
a – temperature; *b* – part of liquid phase for different rise rate of wall temperature: *1* – 0.5; *2* – 1.0; *3* – 2.0 K/s;
c – dynamics of phase composition change during volume synthesis for the case 1

If we take the initial composition with large titanium excess, thermal explosion mode is not observed. Reactions start without sharp temperature growths. If then the external heating continues we come to different final irreversible composition for different temperatures. This agrees qualitatively with the regularities observed experimentally.

Conclusions

The simplest models of volume synthesis of composites are presented. A similar approach taking into account the detailed reaction scheme is applicable for more complex situations. For example, composite synthesis can be carried out in a closed volume or in the container with walls of finite thickness. On the one hand, the walls demand the additional heat for heating to given temperature; on the other hand, the walls store the heat supporting the synthesis when the external heating is ceased or chemical heat release is not enough for reaction accomplishment. In this case, closed reactor walls exchange the heat with the heater immediately. The kinetic part of the problem is similar to the previous one. However, a thermal problem is more complex. The dynamics of this process was illustrated in [17] for the Al, Fe_2O_3; Fe; Cr; Ni system. The explicit accounting of the inert admixtures in the reacting composition leads to the specific degenerate mode [18]. For example, a combination of heating and mechanical loading, at the conditions of HIP (Hot Isostatic Pressing) or SPS (Spark Plasma Sintering), makes it possible to obtain a high density product with special properties. In this case, the dynamics of the synthesis depends on a bigger number of parameters. A mathematical model takes into account different methods of heating, including the Joule heating in the volume, the plunger heating, the heating through reactor walls, and symmetrical and non symmetrical conditions of the loading. The synthesis mode depends additionally on geometrical parameters of the reactor. Various modifications of the model were described in [19–21]. Similar conditions can also lead to the irreversible composition of the product. From a mathematical point of view, the suggested model is a stiff set of ordinary equations that need accurate selection of the solution method. After that, the model could be used for the prognosis of the phase composition evolution with the variation of sintering conditions.

Acknowledgments

The research was supported by Russian Science Foundation; Project No 17-19-01425

References

1. Kobashi M., Ichioka D., and Kanetake N. Combustion synthesis of porous TiC/Ti composite by a self-propagating mode. *Materials*, 2010, issue 3, pp. 3939-3947.

2. Bazhin P.M., Stolin A.M., Konstantinov A.S., Kostitsyna E.V., Ignatov A.S. [Ceramic Ti–B Composites synthesized by combustion followed by high-temperature Deformation], *Materials* 2016, 9, issue 12, p. 10-27; available from: http://www.mdpi.com/1996-1944/9/12/1027 (accessed 16.12.2016)

3. Niyomwas S. Synthesis and characterization of TiC and TiC-Al2O3 composite from wood dust by self-propagating high temperature synthesis. *Energy Procedia*, 2011, issue 9, pp. 522 – 531

4. Jimoh A., Sigalas I., Hermann M. In situ synthesis of titanium matrix composite (Ti–TiB–TiC) through sintering of TiH_2–B_4C. *Materials Sciences and Applications*, 2012, issue 3, pp. 30-35.

5. Boyarchenko O.D., Sychev A.E., Umarov L.M., Shchukin A.S., Kovalev I.D., Shchinava M.A.

Structure and properties of a composite material obtained by thermal explosion in a mixture of Ni + Al + + Cr_2O_3. *Combustion, Explosion, and Shock Waves*, 2017, vol. 53, issue 1, pp. 41–48.

6. Barzykin V.V. Thermal explosion under linear heating, *Combustion, Explosion, and Shock Waves*, 1973, vol. 9, issue 1, pp. 29-42.

7. Merzhanov A.G. Combustion and explosion processes in physical chemistry and technology of inorganic materials. *Russian chemical reviews*, 2003, vol. 72, no. 4. pp. 289-310.

8. Evstigneev V.V., Smirnov E.V., Afanasev A.V. et al. Dynamical thermal explosion in mechanically activated powder mixtures, *Polzunovskiy vestinik* [*The bulletin of Polzunov*], 2007, no. 4, pp. 162-167. (Russ.)

9. Levashov E.A., Mukasyan A.S., Rogachev A.S. and Shtansky D.V. Self-propagating high-temperature synthesis of advanced materials and coatings. *International materials reviews*, 2017, vol. 62, no. 4, pp. 203-239.

10. Stolin A.M., Merzhanov A.G. Critical conditions of thermal explosion in the presence of chemical and mechanical heat sources. *Combust. Explos. Shock Waves*, 1971, vol. 7, no. 4, pp. 431-437.

11. Merzhanov A.G., Barzykin B.G., Abramov V.G. Theory of thermal explosion: from Semenov to our days, *Himicheskaya fizika* [*Chemical Physics*]. 1996, vol. 15, no. 6, pp. 3-44. (Russ.)

12. Nekrasov E.A., Maksimov Yu.M., Aldushin A.P. Calculation of critical thermal explosion conditions in hafnium-boron and tantalum carbon systems using state diagrams // *Combust. Explos. Shock Waves*, 1980, vol. 16, no. 3 pp. 342-347.

13. Kovalev O.B., Neronov V.A. Metallochemical analysis of the reaction in a mixture of nickel and aluminum powders. *Combust. Explos. Shock Waves*, 2004, vol. 40, no. 2, pp. 172-179.

14. Knyazeva A.G., Korosteleva E.N., Kryukova O.N., Pribytkov G.A., Chumakov Yu.A. [Physical regularities of titanium-based composite powder synthesis for additive manufacturing technologies]. *Russian Internet Journal of Industrial Engineering*, 2017, vol. 5, no. 4, pp. 3-13 (Russ.) http://journals.i-publ.ru/index.php/IndEng/article/view/2780

15. Aldushin A.P., Martem'yanova T.M., Merzhanov A.G., Khaikin B.I., Shkadinskii K.G. Propagation of the front of an exothermic reaction in condensed mixtures with the interaction of the components through a layer of high-melting product. *Combust. Explos. Shock Waves*, 1972, vol. 8, no. 2, pp. 159-167.

16. Kukta Y., Knyazeva A.G. [Modeling of composite synthesis at the conditions of controlled thermal explosion], *AIP Conference Proceedings*, 2017, vol. 1909, issue 1, 020113. https://aip.scitation.org/doi/abs/10.1063/1.5013794 (Published Online: December 2017)

17. Knyazeva A.G., Travitzky N. [Modeling of exothermic synthesis of composite with oxide inclusions]. *MATEC Web of Conferences*, 2017, vol. 115, pp. 04004. https://doi.org/10.1051/matecconf/201711504004 (Published online: 10 July 2017)

18. Knyazeva A.G., Chashchina A.A. Numerical study of the problem of thermal ignition in a thick-walled container. *Combust. Explos. Shock Waves*, vol. 40, no. 4, pp.432-437

19. Sorokova S.N., Knyazeva A.G., Modeling of intermetallide synthesis on the substrate of cylindrical form. *Physical mesomech*., 2009. vol. 12, no. 5, pp. 77-90.

20. Knyazeva A.G., Sorokova S.N. [Modelling of powder consolidation using electro heating assisted by mechanical loading]. *Journal of Physics: Conference Series,* 2017, vol. 790, no. 1: [012012, 7 p.]. http://iopscience.iop.org/article/10.1088/1742-6596/790/1/012012

21. Knyazeva A.G. and Buyakova S.P. [Mathematical model of three-layer composite synthesis during hot isostatic pressing]. *AIP Conference Proceedings*, 2016, vol. 1783, 020092. https://aip.scitation.org/doi/abs/10.1063/1.4966385 (Published Online: November 2016).

DOI: 10.17277/amt.2018.03.pp.042-044

Solid State Phase Transition of Nanodiamond upon Heating and Irradiation

V.P. Efremov, E.I. Zakatilova*

Joint Institute for High Temperatures of Russian Academy of Sciences, Bd.2, 13, Izhorskaya St., Moscow, 125412, Russia

* Corresponding author. Tel.: +7 495 485 09 63. *E-mail*: ei.zakatilova@mail.ru

Abstract

The data on the destruction of a diamond single crystal and detonation nanodiamond (**DND**) under radiation exposure are analyzed. The irradiation dose at which graphitization occurs in a single crystal of a diamond is determined. The influence of the DND particle size on the nature of damage during irradiation has been established.

An experimental study of the thermal stability of DNDs at atmospheric pressure in a dynamic argon medium in the temperature range from 30 to 1500 °C with a heat treatment rate of 2 and 10 °C/min is carried out. A same part of DND demonstrates high stability above 1500 °C. A investigation with using X-ray diffraction analysis showed that the solid-state phase transition to DND occurs at about 1000 °C. The examination of the stored samples on an electron microscope showed the influence of the heating rate on the parameters of the DND powder. The data on thermal stability were recommended to improve the technique of ion-plasma coating on the surface of steel parts.

Keywords

Detonation nanodiamonds; synchronous thermal analysis; thermal stability; solid state phase transition; radiation damage.

Introduction

The internal structure of nanoparticles differs from the structure of a bulk crystalline substance [1]. This is due to the large influence of the nanoparticle surface on the crystal lattice. Atoms in the surface layer have neighbors only on one side, this leads to a change in the equilibrium and symmetry of forces and masses, causing a change in the interatomic distances. The change in lattice parameters affects the properties of the entire substance as a whole. Thus, for example, the temperature of the graphitization beginning of bulk diamond at atmospheric pressure exceeds 1500 °C, and the beginning of nanodiamond particle graphitization occurs at temperatures below 1000 °C [2]. Due to its small size, the nanomaterial may have properties that are not possible in a bulk state. This circumstance expands the area of application of nanoparticles in various spheres of human activity.

To date, most of the diamond nanoparticles are produced by detonating high explosives. However, the wide use of this material is limited by the ambiguity and contradictoriness of its properties, available the literature data. This is due to the inhomogeneous structure of detonation nanodiamond particles. The particle has a diamond core and an impurity shell, which consists of non-diamond carbon, metallic impurities, and the radical groups C–H, C–N, C–O located on the surface.

Investigation of the nanodiamond particle stability under various external impacts will give a better understanding of the diamond powder behavior and expand its applicability.

The purpose of this paper is to analyze the data on the solid phase transition in nanodiamond under exposed to irradiation, and to study of the effect of the thermal processing.

Radiation stability of diamond

Irradiation of a diamond single crystal has shown that the irradiation dose might cause point defects, an amorphous path in the material, and a graphite phase can appear in the ion track [3]. Thus, when diamond was irradiated with silicon ions with an energy of 1 MeV, a dose of 1×10^{15} Si^{+}/cm^{2} at room temperature,

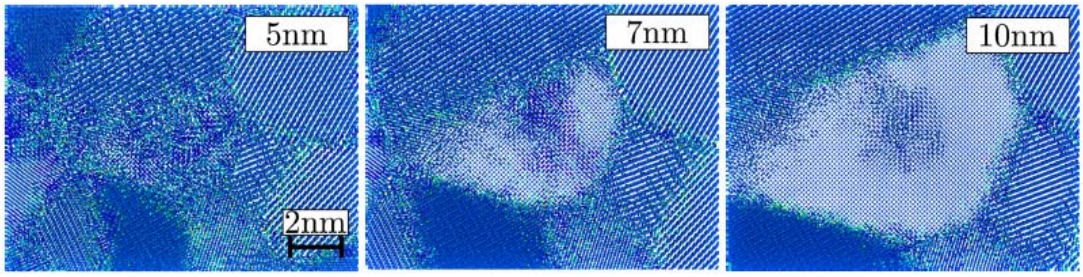

Fig. 1. Molecular dynamics simulation of irradiation of nanodiamond particles by heavy fast ions with an effective stopping energy of 17 keV/nm depending on the particle size [5]

point defects were observed in the sample. Annealing the irradiated sample at a temperature of 1350 °C for 24 hours resulted in the restoration of the defects to an ideal diamond lattice.

Annealing of an irradiated sample of a detonation nanodiamond by fast neutrons led to the release of Wigner energy in the temperature range from 230 to 450 °C. And with an increase in the exposure time of the neutron beam to the sample, the amount of energy released during subsequent annealing in an inert atmosphere increased [4].

When irradiated with silicon ion with the energy of 1 MeV, a dose of 7×10^{15} Si^+/cm^2, an amorphous carbon was formed in the ion track [3]. When the irradiated sample was annealed at a temperature of 1350 °C for 24 hours, graphite was formed from the amorphous phase.

The influence of grain size of nanodiamond on the character of damage during irradiation with fast heavy ions was shown in [5]. When irradiated with heavy ions with effective stopping energy of 17 keV/nm, particles with a size of 5 nm completely became amorphous. After irradiation, particles of 7 nm in size had an amorphous phase surrounded by a diamond. In a particle measuring 10 nm, only a few point defects were observed (Fig. 1).

Thus, the analysis of literature data on the radiation impact on the diamond phase showed that the nanodiamond material is a good sensor in the targets to identify processes occurring in samples exposed to radiation. The content of the saved diamond phase appears to be a function of the type and dose of irradiation.

The conditions of structural-phase transformations depend on the type of action on the substance. It has been experimentally established that irradiation can significantly change the conditions of phase transformations, induce new phases, which affects the performance characteristics and applicability of the material. Before the experimental study of the radiation stability of detonation nanodiamond the theoretical analysis was made of the thermal stability of this material.

Thermal stability of nanodiamond

In this work, the behavior of detonation nanodiamond was analyzed with increasing temperature. Heat treatment was carried out by the method of synchronous thermal analysis in the range from room temperature to 1500 °C with the rates of 2 and 10 °C/min in a dynamic atmosphere of argon.

The initial data of the nanodiamond obtained by the explosion of a mixture of TNT/hexogen (50/50) were given in [6]. After the heat treatment, the stored samples were investigated by X-ray phase analysis and electron microscopy.

The heating the DND sample to 1500 °C at a rate of 10 °C/min resulted in the mass loss was about 16 %. With an increase in the temperature, the radical groups and adsorbed water were removed from the surface of the particles. This process led to a decrease in the mass of the sample by 10–20 % [7].

The X-ray diffraction analysis of the stored samples before and after heat treatment is shown in Fig. 2. From the ratio of the integrated intensities of the base plane of diamond (111) at 2θ = 44° on the X-ray line it was found that the diamond phase decreased with increasing processing temperature (Fig. 2, lines *2 – 5*).

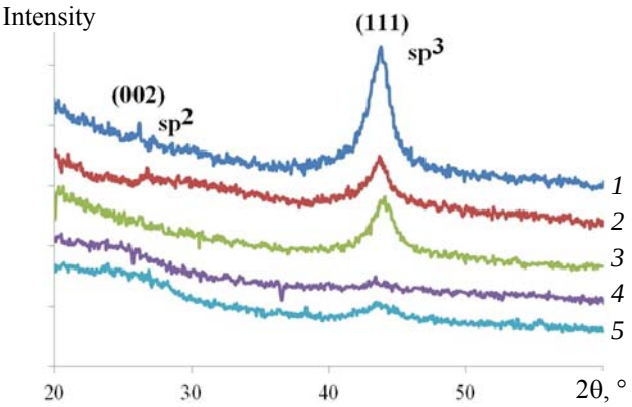

Fig. 2. Diffractograms of DND samples before and after heat treatment:
1 – initial sample; *2* – heated to 600 °C with *v* = 10 °C/min; *3* – heated to 1000 °C with *v* = 10 °C/min; *4* – heated to 1500 °C with *v* = 10°C/min; *5* – heated to 1500 °C with *v* = 2 °C/min (*v* is the rate of heat treatment)

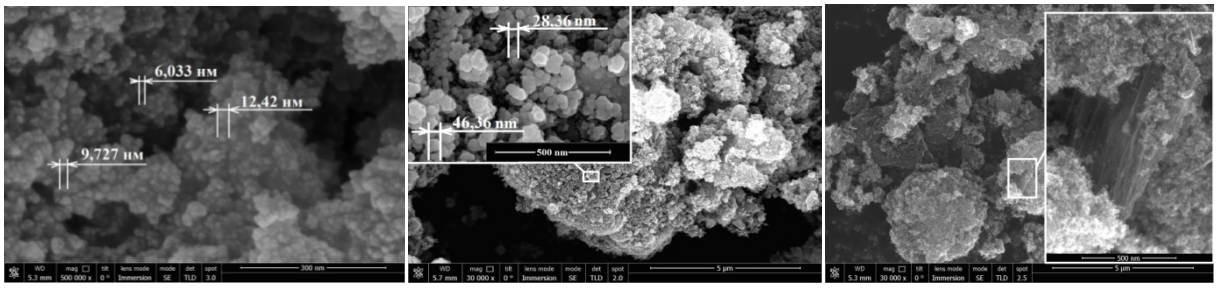

a) *b*) *c*)

Fig. 3. Microstructure of nanodiamond powder:
a – initial sample; *b* – after heat treatment up to 1500 °C at *v* = 10 °C/min; *c* – heated up to 1500 °C at *v* = 2 °C/min

As can be seen from Fig. 2, the graphite peak on the X-ray line from the base plane (002) 2θ = 26° did not increase with increasing temperature. This might mean that the original DND particles underwent destruction, as a result of which they did not go into a crystalline ordered graphite structure with sp^2-bonds, but into an amorphous state, the amount of which cannot be determined by the X-ray method. However, at 1500 °C a halo appeared in the region of Bragg angles 2θ = (20–32)°, which corresponded to a graphite-like X-ray amorphous phase (Fig. 2, lines *4*, *5*). As in the case with graphite, it was a carbon structure consisting of sp^2-bonds in the plane, but the interplanar distance (0.3707 nm) turned out to be larger than that in graphite. Such a structure was stable and, upon further heating, did not go over into ordered graphite. In addition to the X-ray amorphous graphite-like structure, the crystal structure of the diamond was observed in the sample heated to 1500 °C in an amount of 10% of its content (Fig. 2, lines *4*, *5*).

The study of microphotographs of nanodiamond samples before and after heat treatment are shown the influence of the heating rate on the parameters of the powder particles [3].

The initial material of the nanodiamond powder consisted of nanoparticles with sizes of 6–8 nm (Fig. 3*a*). After heating the nanodiamond sample at a heating rate of 10 °C/min to a temperature of 1500 °C, the particles were spherically shaped with sizes of 30–40 nm (Fig. 3*b*) [8]. The characteristic particle size of the powder increased with an increase in the temperature. Perhaps, the individual nanoparticles were "sintered" together. As a result, sintered conglomerates were formed, which can be observed in Fig. 3*b*. When heated at a rate of 2 °C/min, the size of the spherical particles was less than 10 nm and planar formations appeared (Fig. 3*c*), the nature and origin of which requires further investigation.

The data obtained for the thermal stability of nanodiamond particles can be useful for developing new composite materials on their basis and optimizing the process of ion-plasma hardening of the surfaces of steel parts.

The solid phase transition of sp^3 to sp^2 causes a change in the diffraction pattern, which makes this transition promising for diagnosis. The combination of diamond structure and nanosizes and porosity [9] makes it easier to emit radiation from the diagnosed volume. In combination with the studied thermophysical transition conditions, this can be used to diagnose Warm Dense Matter.

References

1. Petrunin V.F. Osobennosti atomnoj struktury ul'tradispersnyh poroshkov i materialov [Features of the atomic structure of ultradisperse powders and materials]. *Zhurn. Vsesoyuz. him. obshchestva im. D.I. Mendeleeva*, 1991, vol. 36, issue 2, pp. 146-150. (Rus)

2. Popov V.A., Egorov A.V., Savilov S.V., Lunin V.V., and at al. Features of the transformation of detonation nanodiamonds into onion-like carbon nanoparticles. *Journal of Surface Investigation. X-ray, Synchrotron and Neutron Techniques*, 2013, vol. 7. pp. 1034-1043.

3. Hickey D.P., Jones K.S., Elliman R.G. Amorphization and graphitization of single-crystal diamond – A transmission electron microscopy study. *Diamond & Related Materials*, 2009, vol. 18, pp. 1353-1359.

4. F. Cataldo, G. Angelini, Z. Révay and other. Wigner energy of nanodiamond bombarded with neutrons or irradiated with γ radiation. *Fullerenes, Nanotubes, and Carbon Nanostructures*, 2014, vol. 22, pp. 861-865.

5. Felipe Valencia, Jose´ D. Mella, Rafael I. Gonza´ lez and other. Confinement effects in irradiation of nanocrystalline diamond. *Carbon*, 2015, vol. 93, pp. 458-464.

6. Efremov V.P., Zakatilova E.I., Maklashova I.V., Shevchenko N.V. Svojstva detonacionnyh nanoalmazov pri povyshennyh temperaturah [Properties of detonation nanodiamonds at elevated temperatures]. *Konstrukcii iz kompozicionnyh materialov*, 2016, vol. 142, issue 2, pp. 48-53. (Rus)

7. Koshcheev A.P. Termodesorbcionnaya mass-spektrometriya v svete resheniya problemy pasportizacii i unifikacii poverhnostnyh svojstv detonacionnyh nanoalmazov [Thermodesorption mass spectrometry in the context of the problem of certification and unification of the surface properties of detonation nanodiamonds]. *Rossijskij Himicheskij Zhurnal*, 2008, vol. LII, issue 5, pp. 88-96. (Rus)

8. Efremov V.P., Zakatilova E.I., Maklashova I.V. and Shevchenko N.V. Thermal stability of detonation-produced micro and nanodiamonds. *Journal of Physics: Conf. Series: Journal of Physics: Conf. Series*, 2018, no. 946, p. 012107.

9. Rosmej O.N., Blazevic A., Korostiy S., Bock R., and at al. Charge state and stopping dynamics of fast heavy ions in dense matter. *Phys. Rev. A.*, 2005, vol. 72, p. 052901.

DOI: 10.17277/amt.2018.03.pp.045-048

Initiation and Combustion of Mechanoactivated Mixtures of Aluminum and Copper Oxide

A.Yu. Dolgoborodov[1 – 4]*, B.D. Yankovsky[1], V.G. Kirilenko[2], A.N. Streletsky[2,3], S.Yu. Ananyev[1,3] , I.V. Kolbanev[2], G.A.Vorobyeva[2], A.A. Shevchenko[2,4]

[1] *Joint Institute for High Temperatures of Russian Academy of Sciences, Izhorskaya St., 13, Bd.2, Moscow, 125412, Russia;*
[2] *Semenov Institute of Chemical Physics RAS, Kosygin St. 4, Moscow, 119991, Russia;*
[3] *Moscow Institute of Physics and Technology (State University), 9, Institutsky per., Dolgoprudny, Moscow Region, 141701, Russia;*
[4] *National Research Nuclear University MEPhI, 31, Kashirskoe Sh., Moscow, Russia*

* Corresponding author. Tel.: +7 495 483 22 95. *E-mail:* aldol@ihed.ras.ru

Abstract

The optimization of parameters of mechanoactivation of powder mixture of Al + CuO for the purpose of realization of the most powerful energy release at chemical interaction of components was performed. Vibration and planetary type of the ball mills were used. The results of mechanoactivation on burning rate were controlled by means of high-speed photography of burning process of samples. Initiation of burning was carried out in the electro spark way with control of the current impulse. The non-stationary mode of propagation of chemical interaction of mixture components was recorded under low level spark. The influence of parameters of mixture porosity and current amplitude of a spark for induction period and the speed of distribution of the reaction front of was defined. The results of the research indicate the prevalence of filtration nature of distribution of chemical interaction.

Keywords

Thermite mixtures; mechanoactivation; burning rate.

Introduction

Thermite mixtures based on metals and solid oxidants allow obtaining a significant exothermic effect during combustion. Al + CuO mixture allows receiving one of the highest exothermic effects per unit of volume (more than 20 kJ/cm^3). However, the burning rate of initial mixtures of micron powders usually does not exceed several tens of mm/s, which limits the field of their application. This is because that development of chemical reactions in solid mixtures takes place on the contact surface of reactants, which in the case of large particles is rather small. To increase this surface, various methods, such as ultrasonic mixing of nanosized powders, electrochemical deposition of submicron metal-oxidizer layers, etc. are used. [1]. One of the relatively new methods for obtaining thermite composition is the preliminary mechanochemical activation of mixtures of micron-sized particles in high-energy intensity ball mills. Initial components in this process are shredded, mixed and acquire new defects of crystal structure, which leads to an increase in the surface area of contact of the reagents at the submicron and nanoscale levels and to the formation of additional reaction spots. Thus, by means of mechanoactivation of oxidizer-metal mixtures it is possible to regulate the rate of energy release for different of specific application. In Russia, the method of preliminary mechanoactivation of solid oxidant-metal fuel mixtures has been actively used since the beginning of the 2000s [2–5], and the resulting materials are called Mechanically Activated Energetic Composites (**MAEC**).

The practical use of exothermic energy release is associated with the implementation of different parameters: the rate or power of heat release, the quality and intensity of light radiation, etc. However, in all cases, the completeness, or the effectiveness of the

chemical interaction, is an important factor. This indicator largely depends on the conditions of application: the physical parameters of the components, the initial parameters of the mixture, the energy and power of initiation, as well as other physical and geometric factors.

In this work, tendencies of manifestations of chemical interaction of MAEC Al/CuO are investigated under different conditions of its realization. An ultimate goal of a research is optimization of mechanoactivation parameters of this mixture for effective application in different conditions.

Before experiments the mixture of Al + CuO powders were subjected to mechanoactivation. Then the mixture was compacted in experimental samples with controlled porosity. The samples were mounted in experimental assemblies and initiation of chemical interaction was made. The characteristics of manifestations of combustion process of samples were an object of research in which mechanoactivation time, the samples porosity, the initiation parameters and the experiment scheme were parameters. High-speed camera, four-channel pyrometer, photoelectronic and electrocontact sensors were used as tools. The characteristics of a luminescence area were speeds of borders and brightness.

Prior to the experiments, a mixture of Al and CuO powders was subject to mechanoactivation under various conditions. The mixture was then compacted into experimental samples with controlled porosity. The samples were mounted in experimental assemblies and produced an electro-spark initiation. The characteristics of the combustion process were the subject of the study, in which the mechanoactivation time, the porosity of the samples, and the energy of the spark initiation were the initial parameters. The speed of the boundaries of the luminous cloud of products and their brightness were measured. High-speed camera, pyrometer, photoelectronic and electro-contact sensors were used as a tool.

Materials and mechanoactivation parameters

As the initial components, micron and nanosized powders were used. Al weight content was from 18 to 25 %. Mixing and activation was carried out in the vibration mill of the Aronov design or in the planetary mill "Activator-2sl" with steel drums and balls. Estimate of the energy intensity of the two types of mills based on the growth of the specific surface area of the test material (MoO_3) is for "Ativator-2sl" at a total power J = 9.7 W/g, and for the Aronov mill J = 3.7 W/g. Weight load of powders was 10–25 g, the mass of balls was 200–300 g. Hexane was added to reduce frictional heating. The starting powders and MAEC were analyzed by X-ray diffraction, electron microscopy and thermo-gravimetric analysis. It is established that the activation of the obtained material resulted in a polydisperse mixture of fairly large conglomerates of flat fragments of Al particles (~ 1–10 μm) with submicron CuO particles. Owing to different strength characteristics of material, dispersion in sizes and a form of particles, conglomerates represented the disordered structures with numerous, but divided, points of contact of components. These points of contact of components, presumably, can serve as primary centers of chemical interaction.

Experiments

Primary analysis of mechanoactivation influence was carried out by means of determination of dependence between ignition delay time and mixture temperature. As a rule, the ignition delay increases with reduction of temperature. It was defined that temperature of ignition of the mixture, activated in different conditions, lies in range from 200 to 350 ºC.

At electro spark initiation of a bulk sample on the horizontal plane (mass from 0.03 g and above) the area of a luminescence is formed. On a set of experimental data, this area should be characterized as the extending stream of the reacting clusters of mixture components in a cloud of the radiating plasma of burning products with a specific resistance of 10^7 Om·mm^2/m. By pyrometric measurements, the brightness temperature of a luminescence area changes from 2400 to 3700 K depending on mixture activation time. Characteristic scattering rate of burning products of local samples and also the burning rate of linear samples (with a linear density from 0.2 g/cm and above) are tens of meters per second. The existence of small air intervals between separated samples does not interfere with distribution of burning and does not influence the burning rate. An increase in the mass of separated samples leads to the growth of the expansion speed of the chemical reaction.

The burning initiation of the compacted mixture sample (porosity of 50–70 %) was carried out in the electrospark way in a glass tube with a diameter of 5.5 mm (Fig. 1). The tube end face on the initiation side, as a rule, was closed. The spark gap between wire electrodes with a diameter of 0.1–0.5 mm was 0.1–1.0 mm. The current through a spark interval was changed in the range of 40–350A. The current impulse duration of a spark was ~ 1 μs on the basis. The moment of sparking was used for synchronization of the high-speed photo recorder Cordin 222-4G. The photo recorder took 16 photos of process in beforehand determined time points.

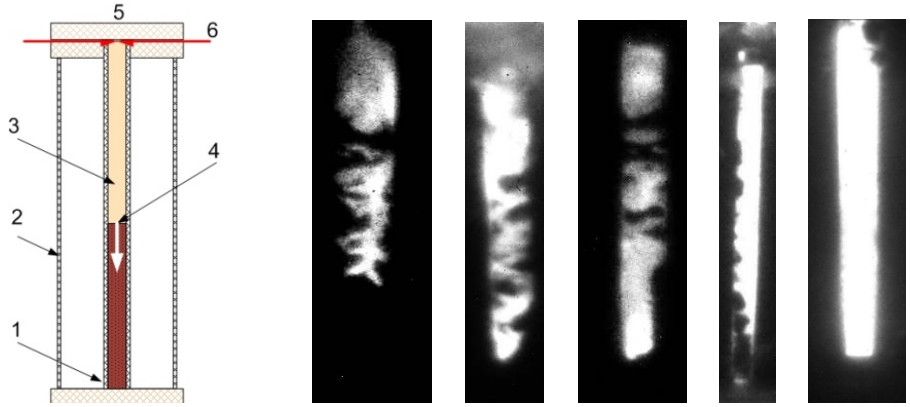

Fig. 1. Initiation with the maximum current through a spark interval:
a – experimental scheme: *1* – dark part of glass tube (no combustion); *2* – glass vessel with water; *3* – light part of tube (combustion); *4* – a boundary between dark and light parts of tube; *5* – spark gap; *6* – electrodes;
b – photos of luminescence inhomogeneity at various spark currents

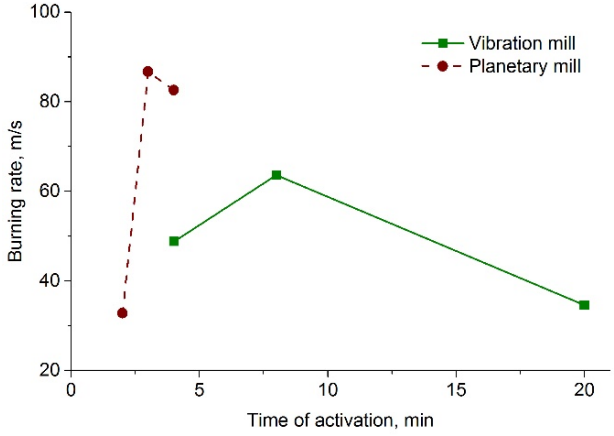

Influence of mechanoactivation time: achievement of the maximum burning rate

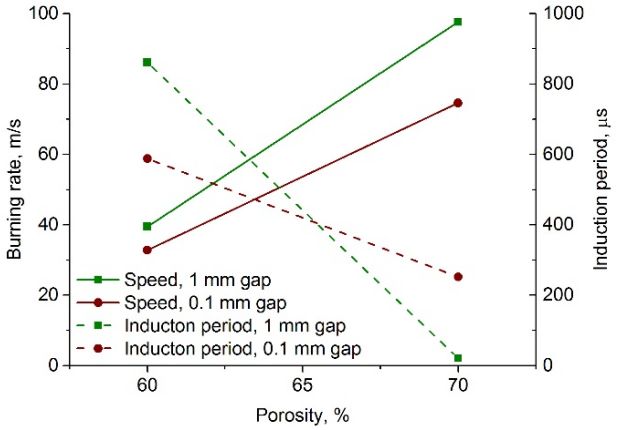

Influence of a sample porosity (planetary mill): considerable reduction of induction period and increase in burning rate

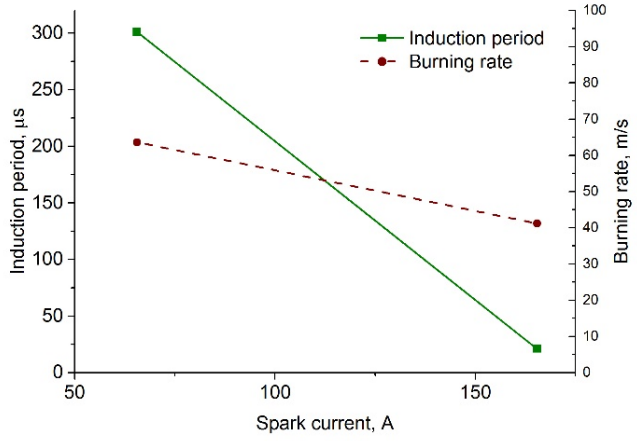

Influence of spark current (vibration mill): considerable reduction of the induction period at insignificant reduction of burning rate (insufficient warming up of cold mix)

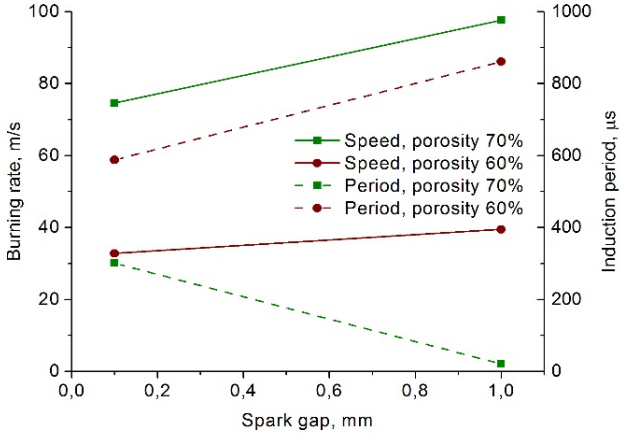

Influence of length of a spark interval (planetary mill): minor changes in the induction period and increase in burning rate (increase in volume of an electrospark energy contribution)

Fig. 2. Set of experimental data

In the photos, a border between dark and light parts of a tube was fixed (Fig. 1). This border was identified with some stage of chemical interaction characterized by a certain temperature. In case of the disordered structure of our mixture, it may concern thermal explosion in the neighborhood of contact points of components. At small currents through an electric spark (< 150 A) the area of burning has pronounced non-uniform character. Zones of a bright luminescence of hot products alternate with dark zones at photos. With increase in spark current, the uniformity of a luminescence increases.

The long luminescence abroad of the section of zones in process of its movement is caused by hashing and interaction of initially not contacting parts of components. Time interval between the moment of initiation and formation of border is usually called the induction period. Movement of this border in time was taken for the speed of burning of mixture in a tube.

Results

By set of experimental data is determined the tendency of change of characteristics of burning depending on parameters of mechanoactivation, compaction and initiation (see Fig. 2). Each tendency is created according to two experiments with identical other conditions.

Analysis of dependences of Fig. 2 reveals the strongest influence of mechanoactivation time, mixture porosity and a spark current amplitude for induction time and the rate of chemical interaction. It assumes the leading role of the filtration mechanism in energy transfer for initiation of chemical interaction in cold sites of mixture.

Conclusions

In general, the results of the work have shown the promise of preliminary mechanochemical activation for the production of fast-burning thermite compositions. For each type of mills, there are optimum conditions of activation at which the greatest reactionary ability, rate and temperature of burning are reached. At excess of this value, there is a partial interaction of components in the activation process and decrease in burning characteristics.

References

1. Energetic Nanomaterials: Synthesis, Characterization, and Application / Ed. by V.E. Zarko and A. Gromov. 2016. Elsevier Inc.

2. Dolgoborodov A.Yu., Gogulya M.F., Makhov M.N., et al. Detonation-like phenomena in Al/S mixture", *Proc. Twenty-Ninth Intern. Pyrotechnics Seminar*, 2002, pp. 557-563.

3. Dolgoborodov A.Yu., Makhov M.N., Kolbanev I.V., Streletskii A.N. Mechanically activated pyrotechnic composition, *RF Patent No. 2235085*, 2004.

4. Dolgoborodov A.Yu. Mechanically activated oxidizer-fuel energetic composites. *Combustion, Explosion, and Shock Waves*. 2015, vol. 51 issue 1, pp. 86-99.

5. Streletskii A.N., Sivak M.V., Dolgoborodov A.Yu. Nature of high reactivity of metal/solid oxidizer nanocomposites prepared by mechanoactivation: a review. *J. Mater. Sci.* 2017, vol. 52, issue 20, pp. 11810-11825.

DOI: 10.17277/amt.2018.03.pp.049-056

The Effect of a Carbon Nanotubes-Based Modifier on the Formation of the Cement Stone Structure

Yu.N. Tolchkov[1*], Z.A. Mikhaleva[1], A.G. Tkachev[1],
O.V. Artamonova[2], M.A. Kashirin[2], M.S. Auad[3]

[1] *Tambov State Technical University, 1, Leningradskaya St., Tambov, 392000, Russia;*
[2] *Voronezh State Technical University, 84, 20-Letiya Oktyabrya St., Voronezh, 394006, Russia;*
[3] *NanoTechCenter Ltd., 51, Sovetskaya St., Tambov, 392000, Russia*

* Corresponding author: Tel: +7 (915) 664 44 88. *E-mail:* Tolschkow@mail.ru

Abstract

The present paper considers the effect of carbon nanotubes, used as the main component of a modifying comprehensive nanoadditive, on the kinetics of cement hydration, the phase composition and the strength characteristics of a cement stone. The increase in the strength characteristics of the cement stone modified by the nanoadditive was found to be due to the acceleration of the cement hydration, the formation of an optimum microstructure, in which, according to X-ray phase analysis, additional formation of low-basic calcium hydrosilicates already takes place during the initial period of hardening. Based on scanning electron microscopy, additional directional crystallization of particles of cement stone neoplasms, mainly with contacts of intergrowth, was elucidated. Accelerated curing kinetics of the nanomodified samples was observed to take place with an increase in the compressive strength of 20–30 % at the age of 28 days.

Keywords

Nanomodifier; carbon nanotubes; X-ray phase analysis; cement hydration kinetics; cement stone.

Introduction

The formation of composites for construction purposes is determined by the following factors: type and characteristics of cement (chemical and mineralogical composition, fineness of grind, presence of mineral and other additives in the cement composition); water/cement ratio value; additional mechanical and chemical activation of cement; mixing conditions and modes; temperature hardening conditions; introduction of special additives to the concrete mixture, including those ones that exert their effect at the micro- and nanostructured levels of cement stone and concrete [1].

During the last period of time (10–20 years) there has been a significant transition in technologies and properties of construction materials; new types of composites – high-tech, high-strength, and low-shrinkage – have appeared.

Simultaneously with the development of construction materials, new classes of additives have been added to the agenda. They are related to deeper mechanisms of structure formation, and can comprise nanoadditives or nanomodifiers [2].

The modification of composites using various nanomodifiers, including carbon-containing ones, seems promising, since their introduction significantly improves the physical and mechanical characteristics at low dosages of additives and allows to directly adjust the material structure of the material through the manifestation of various effects [2–5].

However, due to the high surface energy of nanoparticles when using them as nanomodifier components, they can be prone to agglomeration; the size of agglomerates can reach micrometer scales.

In principle, the nanomodification of composites can be performed in two main ways: 1) nanostructures having preset parameters and sizes are pre-synthesized, and then introduced into the raw mixture; and 2) directed nanoparticle synthesis is realized in the system, due to which the nanomodification of the material structure takes place.

When implementing the second method, the essential difficulties in introducing the nanomodifier and its uniform distribution are minimized as much as possible. If pre-synthesized nanostructures (for example, a dry component mixture) are used, they must be additionally prepared for introducing into the composite structure. The most common way is to prepare an aqueous suspension based on them.

The analysis of works [4, 5] dedicated to this subject shows that the structure and mechanical characteristics of cement composites modified by carbon nanoadditives make it possible to significantly increase the values of physical and mechanical indicators. According to the authors, these changes were achieved due to the formation of a less porous structure in nanomodified samples and a greater amount of calcium hydrosilicates compared with non-modified samples.

The effect of mixing water structured with fulleroid nanoparticles on the cement stone characteristics was considered by Pukharenko and his co-authors [6]. They established that the nanostructuring of mixing water leads to a 1.4–1.7 times decrease in the viscosity of the cement paste. The results indicate a significant qualitative increase in the indices of workability and preservation of the given mobility when maintaining a fixed consumption of cement or reducing it.

In papers [7, 8], mathematical modeling of the changes in the properties of nanomodified composites and the effect of the used carbon nanoadditives on the strength characteristics of the material were studied. The analysis of the microstructure of the nanomodified samples allowed elucidation of the formation of individual crystallites of calcium hydrosilicates located in the zone of close contact of carbon nanoparticles, which contributes to the filling of microvoids and the creation of a single structure. The dependences between the length of carbon nanotubes and the processes associated with the agglomeration of nanoparticles in the bulk of the composite structure were revealed. When "shorter" carbon nanotubes were used, the accumulation of particles was absent or not significantly observed.

The processes of concrete nanomodification using carbon nanotubes have been studied by researchers from St. Petersburg under the leadership of A. Ponomarev. The scientists have developed a modifier on the basis of a water-soluble fullerene, the application of which is directed at construction materials [9, 10]. The modifier possesses the following properties: bulk density of 600–900 $kg \cdot m^{-3}$, and average cluster size of 300 nm. Using this material in cement mixtures (0.15 % of cement mass) leads to a change in mobility in the range from M1 to M5, substantially increasing the strength parameters in the range of 25–40 %.

The analysis of the results of studies [11, 12] showed an increase in the physical and mechanical characteristics of construction composite samples when using a multifunctional additive dispersion based on multiwalled carbon nanotubes at the dosage level of 0.006 % of the binder (gypsum, cement), thereby contributing to an increase in the strength at early stages of hardening (day 7) and being about 55 % in comparison with reference compounds.

Thus, the aim of the present paper is to study the effect of carbon nanotubes used as a modifying comprehensive nanoadditive on the kinetics of cement hydration, the phase composition and the strength characteristics of a cement stone.

Materials and methods

In the present work, the experimental data on employing the above-mentioned comprehensive nanoadditive to modify the cement stone are presented.

“Taunit”-series multiwalled carbon nanotubes (**CNTs**) produced at NanoTechCenter Ltd. (Tambov, Russia) were used as the main component of the additive. The outer and inner diameters of these CNTs are 40 and 5 nm, respectively, their density is 560 $kg \cdot m^{-3}$, and the average length of single nanotubes is 2 microns (Fig. 1).

The nanomodifier used herein represents a colloidal system (Table 1), the synthesis of which was carried out by ultrasonic treatment of the CNTs in an aqueous medium additionally containing surfactants.

The procedure for obtaining modifying additives and optimum formulations was used based on previously developed parameters [13]. The impact of ultrasound to the system was carried out on an IL-100-6/4 ultrasonic device; the optimum dispersion time was 20–30 min, and the amplitude of oscillations was at the frequency of 22 kHz (Table 1). The dispersibility of the CNTs and the stability of the resulting dispersions were monitored on a KFK-3 photocolorimeter at the wavelength of 500 nm. The distribution of the nanomaterials in the aqueous suspension was estimated from the optical density of colloidal solutions [14]. Polyvinylpyrrolidone was the main surfactant contributing to the preservation of the system in the sedimentation-stable state. The optimum ratio of the components (carbon nanomaterials : surfactants on a dry matter basis was 1 : 2).

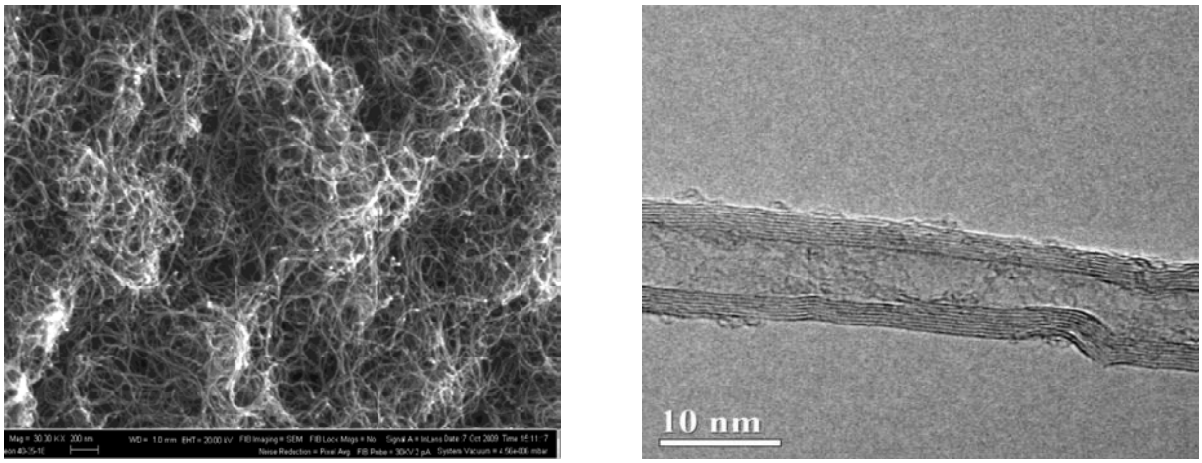

Fig. 1. SEM and TEM images of the "Taunit"-series CNTs

Table 1

Compositions, forms and methods of nanomodifier preparation

Nanomodifier	Composition	Chemical formula of surfactants used	Preparation methods
Colloidal solution (SMM, SM24)	"Taunit"-series CNTs – 0.0001 – 1%, Surfactant – 0.0002 – 2%, Water – the rest	Polyvinylpyrrolidone $(C_6H_9NO)_n$ 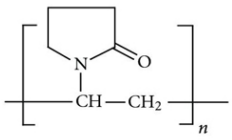 Octylphenol ethoxylate (Triton X-100) $(C_{34}H_{62}O_{11})$ 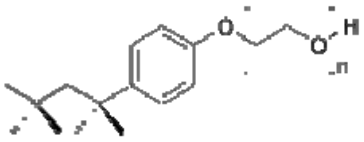 Naphthalene lingosulfonates (S-3 plasticizer) $R_n C_{10}H_{7-n}SO_3M$ 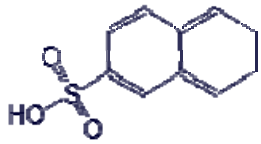 Polycarboxylate esters 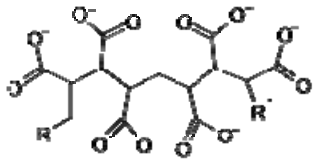	Ultrasonic treatment Sonication time – 20–30 min; Frequency – (22 ± 10) % kHz
Colloidal solution (SMTK)	"Taunit"-series CNTs – 0,0001 – 1 %; Surfactant – 0,1–3 %; Water – the rest	Potassium polytitanate $(K_2O{\cdot}nTiO_2)$ 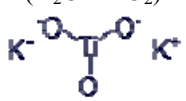	

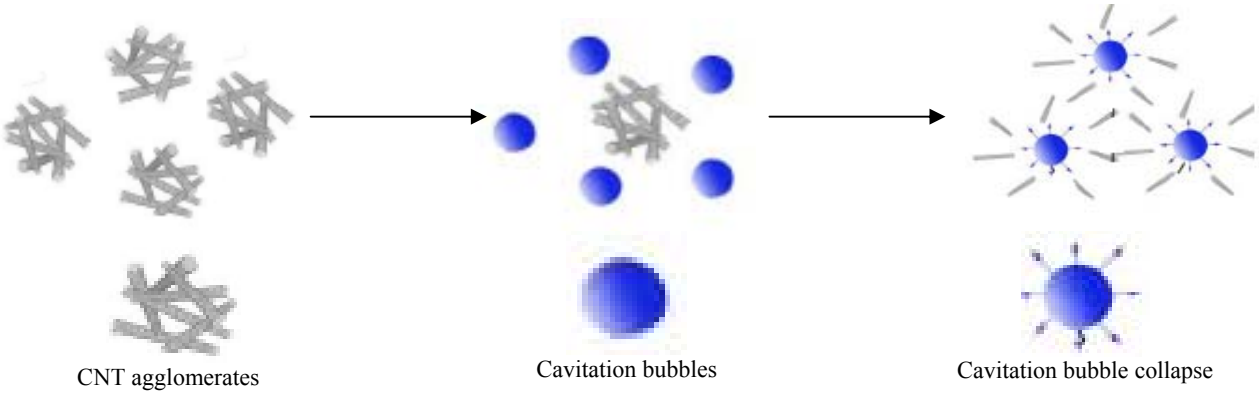

Fig. 2. Interaction between CNTs and surfactants as a result of sonication in an aqueous medium

The use of the surfactants is due to the need for reducing the coagulation effect in the suspension and the decrease in the surface interphase energy, which greatly simplifies the dispersion process (Fig. 2).

The suspensions were stabilized due to the formation of an adsorption layer onto the surface of the CNTs by means of the surfactant medium. This layer prevents CNT convergence, thereby saving the unique properties of nanostructures (adsorption, chemisorptions, topological effect). In this case, the activated water with the CNTs represented mixing water for the cement hardening system. Thus, the problem of uniform distribution of nanostructures in the construction composite was solved. Based on preliminary experimental studies, the optimum concentration dosage of the comprehensive carbon nanoadditive in the cement composition was determined, which was found to be 0.0001–0.0007 % of cement weight [15, 16].

This concentration interval experimentally obtained for the nanomodifier application corresponds to a qualitative change in the physical and mechanical characteristics of the modified composite and promotes the production of a sedimentation-stable CNTs-based suspension with optimum use and storage parameters (not more than three days). It can be assumed that the availability of such a dosage interval is associated with high chemical activity and a large reactively active surface area of the carbon nanomodifiers. It is most likely that conditions, under which chemically active carbon nanostructures retain a part of the required mixing water, are created when increasing the CNTs dosage. In this case, the formation of water deficiency possibly takes place for the mineral hydration of the binder material.

The dosage intervals applied for the nanoadditives have also been confirmed by other authors [17–20].

In the experimental studies, CEM I 42.5 Portland cement (Russian Standard GOST 31108–2003) and the above-mentioned nanoadditives (the dosage of 0.0006 %) were used for the production of a cement paste having a water/cement (**W/C**) ratio of 0.33. The kinetics parameters of the cement hydration process were studied under normal conditions, the duration of the process was 1, 3, 7, 14 and 28 days. The phase composition of the reference and nanomodified cement stones was monitored by X-ray diffractometry (CuKα radiation, $\lambda = 1.5406$ Å, D2 Phaser Bruker diffractometer); the data were processed automatically using the PDWin 4.0 software. The hydration degree was calculated [21] according to the following formula:

$$C_h(\mathrm{C_3S}) = \left(1 - \frac{I_{\mathrm{mod}}}{I_0}\right)100\,\%, \qquad (1)$$

where I_{mod} is the intensity of the diffraction maximum at $d = 2.75$ Å of the $3CaO{\cdot}SiO_2$ (C_3S) phase of samples having different composition and cement hydration time; I_0 is the intensity of the diffraction maximum at $d = 2.75$ Å of the $3CaO{\cdot}SiO_2$ (C_3S) phase of the initial cement.

The compressive strength of the cement stone was determined after 1, 3, 7, 14 and 28 days of hardening under normal conditions. The samples (size $5 \times 5 \times 5$ cm) were tested using an IP-500M-Auto system. To ensure statistical reliability of the physical and mechanical test results, the number of the samples in the series was 9–12. It was determined that the intra-series coefficient of variability of the strength evaluation results did not exceed 7–10 %.

Results and discussion

The generalization of the experimental data shows that in the systems containing the nanomodifying additives the cement hydration process is substantially accelerated (Fig. 3, Table 2): for a daily hardening time, the hydration degree for samples 3 and 4 reaches the values of about 50 %, which in the reference system is achieved only on the 28th day.

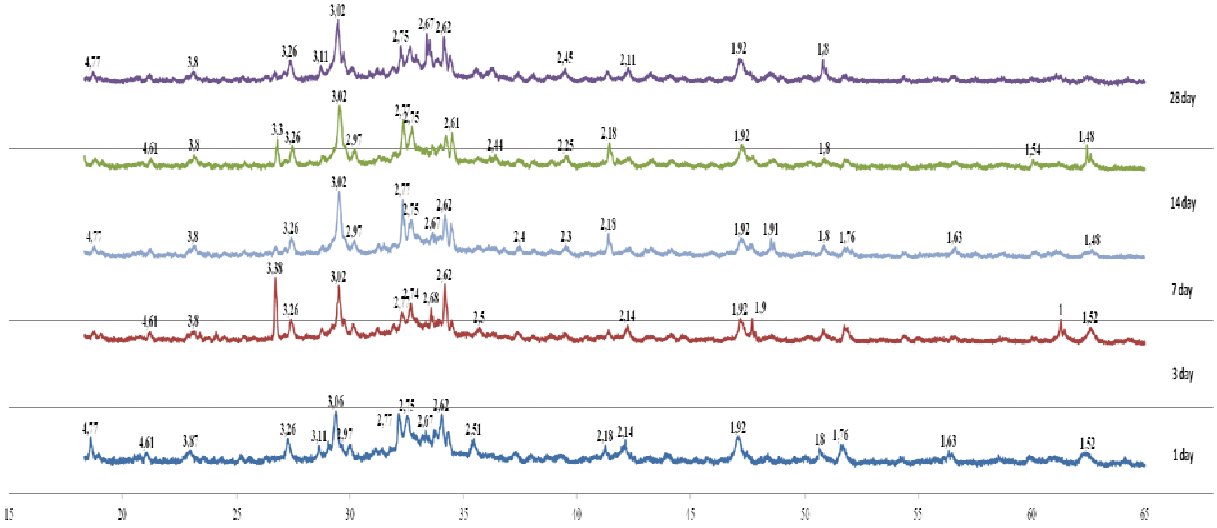

a)

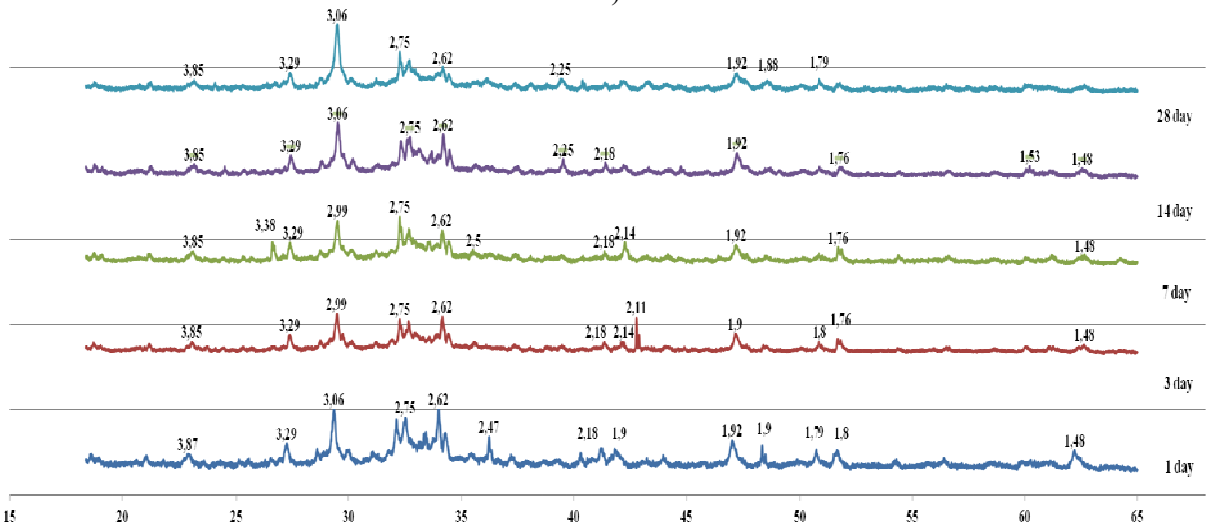

b)

Fig. 3. X-ray diffractometry studies of the cement stone hydration:

a – reference sample: $2CaO{\cdot}SiO_2$ (d = 3.8; 3.38; 2.51; 2.61; 1.9; 1.8); $3CaO{\cdot}SiO_2$ (d = 3.02; 2.75; 2.61; 2.18; 1.76;); $Ca(OH)_2$ (d = 3.11; 2.62; 1.92; 1.79; 1.48;); $2CaO{\cdot}SiO_2{\cdot}H_2O$ (d = 4.77, 4.61; 3.87; 3.26; 2.18); $2CaO{\cdot}SiO_2{\cdot}0.5H_2O$ (d = 2.77; 2.67; 2.5; 1.8; 1.61; 1.52)

b – SM24 nanomodifier: $2CaO{\cdot}SiO_2$ (d = 3.8; 3.38; 2.51; 2.18; 1.9; 1.48); $3CaO{\cdot}SiO_2$ (d = 3.02; 2.75; 2.61; 2.18; 1.76;1.48); $Ca(OH)_2$ (d = 2.62; 1.92; 1.79); $2CaO{\cdot}SiO_2{\cdot}H_2O$ (d = 3.28; 3.87; 3.85; 3.11; 2.18; 2.11); $2CaO{\cdot}SiO_2{\cdot}0.5H_2O$ (d = 3.29; 2.99; 2.67; 2.5; 2.25)

Table 2

Degree of the cement stone hydration when using the nanomodifiers

No.	System	CNT content in nanomodifier, %	Degree of hydration				
			Day 1	Day 3	Day 7	Day 14	Day 28
1	Cement-Water	0	30.0	32.9	34.6	38.5	46.8
2	Cement-Water-SMM	0.0006	53.9	59.2	65.2	63.5	64.0
3	Cement-Water-SMTK		21.4	28.0	60.6	63.1	63.1
4	Cement-Water-SM24		46.8	51.1	51.4	55.0	62.3

From on the results of the X-ray phase analysis of the reference and nanomodified cement stone samples, it can be assumed that the change in the intensity peak ratio on the diffractograms recorded for the modified samples may be due to the blocking action of the nanomodifier, at which part of calcium ions remains in the solution and further does not interact with other substances, possibly leading to the formation of smaller crystals covering vacant pores of the cement stone [22, 23]. The X-ray diffractometry studies of the modified samples allowed to observe the calcium hydrosilicate phases of various compositions ($(CaO)_x \cdot SiO_2 \cdot 8H_2O$, $2CaO \cdot SiO_2 \cdot H_2O$, $CaO \cdot SiO_2 \times \times H_2O$) on all the X-ray patterns. In this case, the diffractometric peaks are wider, thereby indicating the formation of a fine-crystalline structure. When increasing the hardening time, the availability of the ettringite phase can be fixed, confirming the CNT effect on the morphology of the resulting cement stone.

The microstructure of the reference and nanomodified fine-grained concrete samples was elucidated by electron microscopy (Fig. 4).

It was established that an increased interaction of some adhesion contacts and directional crystallization of the neoplasm particles take place in the composite modified with the comprehensive nanomodifier.

When using the CNTs-based nanomodifiers, the composite structure is more densely packed with the particles, thereby making it possible to conclude that the physical and mechanical characteristics of the material increase (Fig. 5) as a result of the formation of an ordered structure and neoplasms with an altered morphology of the crystalline hydrates. This is confirmed by the presence of needle crystals (the size of individual crystals reaches 3–5 microns), which presumably perform discrete nanostructuring of the cement systems, combining the neoplasms into a single conglomerate and acting the reinforcing role

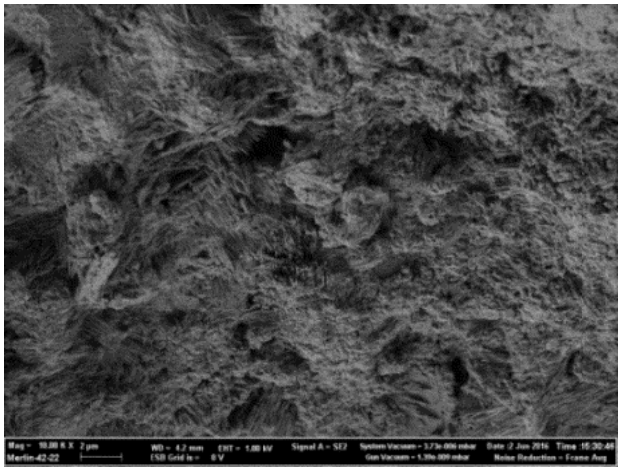

a)

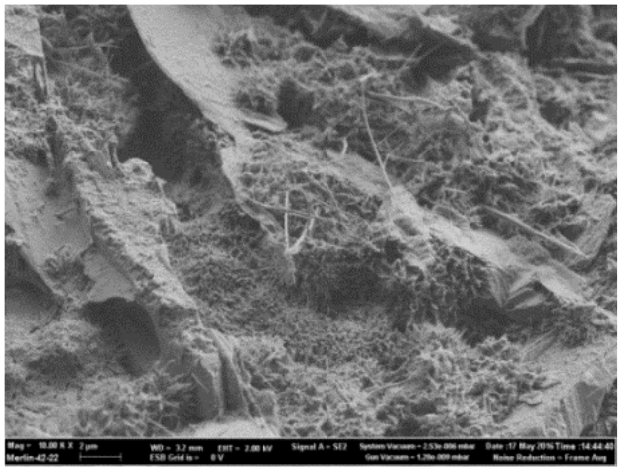

b)

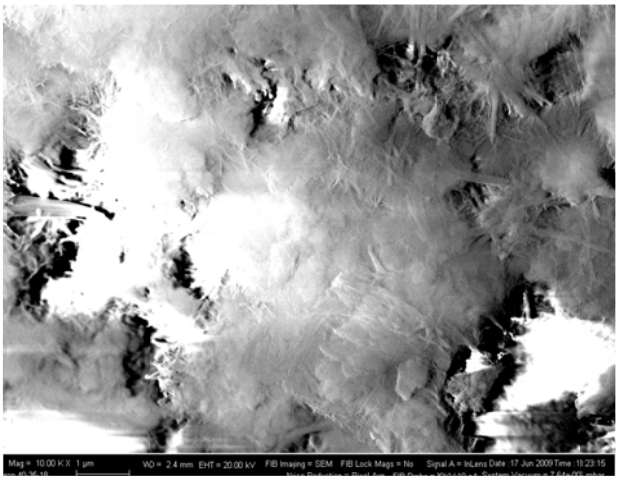

c)

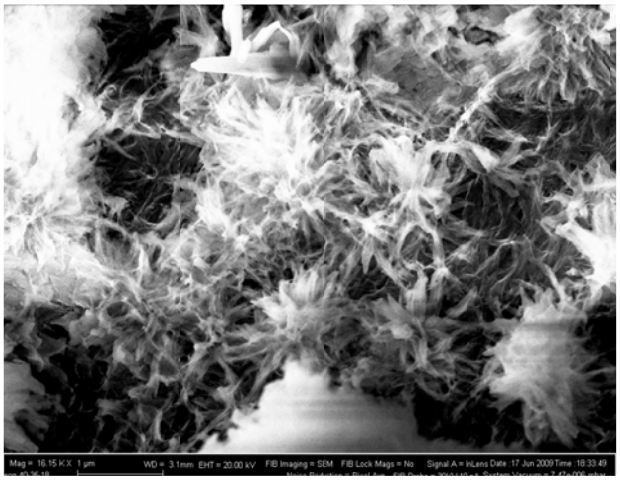

d)

Fig. 4. Microstructure of the nanomodified fine-grained concrete samples:
a, *c* – reference sample (cement-water-sand); *b*, *d* – nanomodified sample (cement-water-sand-SM24)

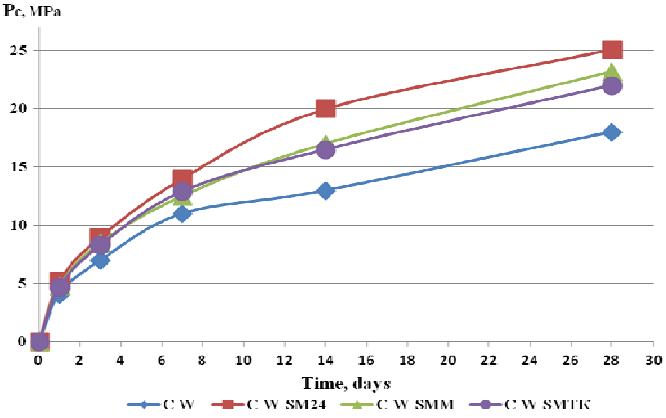

Fig. 5. Kinetics of gaining the strength obtained for the cement stone when using the nanomodifiers:
Systems: C-W (cement-water), C-W-SM24 (cement-water-SM24), C-W-SMM (cement-water-SMM), and C-W-SMTK (cement-water-SMTK)

in the concrete structure. Besides, agglomeration of the nanofiller from a set of spheric nanoparticles can also be observed, which characterizes the degree of activity of the carbon nanoparticles and their surface forces. The formation of the crystalline hydrates on the CNT surface leads to the creation of an extra supramolecular structure that has its direction and CNTs-like surface possessing its own substructure [24–26].

All the nanomodified samples obtained showed an increase 30–50 % in the specific surface area in comparison to the reference composition. It should be noted that the specific surface area values determine the dispersity of the material and geometric characteristics of the pore channels; on the other hand, these factors are key elements for the formation of a qualitative and durable material structure.

When modifying the cement stone structure with the nanoadditives, the nanomodification efficiency can be determined not only by the hydration kinetics change but also by the strength kinetics change (strength gain rate, duration of reaching "release" and achievable limit values of the cement stone strength). The studies carried out demonstrated acceleration in gaining the strength for all the nanomodified samples, as well as an increase of 20–30 % in the compressive strength.

Conclusion

The effect of the CNTs-based comprehensive nanomodifier on the kinetics of cement hydration, phase composition and strength characteristics are considered herein.

It was established that when the nanomodifier is introduced, the cement hydration process is accelerated, and the optimum microstructure of the cement stone is formed. At the same time, scanning electron microscopy confirmed the formation of extra directional crystallization of cement stone neoplasm particles, mainly with intergrowth contacts.

The X-ray diffraction analysis showed a change in the phase composition of the nanomodified samples, with an extra formation of low-base calcium hydrosilicates even at an early stage of hardening.

The studies conducted on the kinetics of gaining the strength of the nanomodified cement stone demonstrated an increase of about 20–30 % in the compressive strength at the age of 28 days for all the samples.

References

1. Artamonova O.V., Chernyshov E.M. Concepts and foundations of technologies for nanomodifying structures of construction composite structures. Part 1: General problems of fundamentality, main directions of research and development. *Construction Materials* [*Stroitelnye materialy*], 2013, issue 9, pp. 82-95 (Rus).

2. Chernyshov E.M., Artamonova O.V., Slavcheva G.S. Concepts and foundations of technologies for nanomodifying structures of construction composite structures. Part 3: Efficient nanomodification of cement hardening systems and cement stone structure (criteria and conditions). *Construction Materials* [*Stroitelnye materialy*], 2015, issue 10, pp. 54-64 (Rus).

3. Scrivener K.L., Kirkpatrick R.J. Innovation in use and research on cementitious material. *Cement and Concrete Research*, 2008, vol. 38(2), pp. 128-136.

4. Konsta-Gdoutos M.S., Metaxa Z.S., Shah S.P. Highly dispersed carbon nanotube reinforced cement based materials. *Cement and Concrete Research*, 2010, issue 40, pp. 1052-1059.

5. Konsta-Gdoutos M.S., Metaxa Z.S., Shah S.P. Multi-scale mechanical and fracture characteristics and early-age strain capacity of high performance carbon nanotube/cement nanocomposites. *Cement and Concrete Composites*, 2010, vol. 32, pp. 110-115.

6. Pukharenko Yu., Aubakirova I., Staroverov V. Structural features of nanomodified cement stone. *Architecture and Engineering*, 2016, vol. 1, issue 1, pp. 66-70.

7. Sobolkina A., Mechtcherine V., Khavrus V., Maier D, Mende M., Ritschel M., Leonhardt A. Dispersion of carbon nanotubes and its influence on the mechanical properties of the cement matrix. *Cement and Concrete Composites*, 2012, vol. 34, pp. 1104-1113.

8. Smilauer V., Hlavacek P., Padevet P. Micromechanical Analysis of Cement Paste with Carbon Nanotubes. *Acta Polytechnica*, 2012, vol. 52, pp. 22-28.

9. Kiski S.S., Ponomarev A.N., Ageev I.V. Chang Cun Modification of the Fine – Aggregate Concrete by High Disperse Silica Fume and Carbon Nanoparticles Containing Modifiers. *Advanced Materials Research*, 2014, vols. 941-944, pp. 430-435.

10. Ponomarev A.N., Egorushkin V.E., Melnikova N.V., Bobenko N.G. On the low-temperature anomalies of specific heat in disordered carbon nanotubes. *Physica E: Low-Dimensional Systems and Nanostructures*, 2015, vol.66, pp. 13-17.

11. Yakovlev G., Keriene J., Gailius A., Girniene I. Cement Based Foam Concrete Reinforced by Carbon Nanotubes. *Materials Science*, 2006, vol. 12 (2), pp. 147-151.

12. Yakovlev G., Pervushin G., Maeva I., Keriene Ja., Pudov I., Shaybadullina A., Buryanov A., Korzhenko A., Senkov S. (2013) Modification of Construction Materials with Multi-Walled Carbon Nanotubes. *Proceedia Engineering*, vol. 57, pp. 407-413. doi: 10.1016/j.proeng.2013.04.053.

13. Tolchkov Yu.N., Mikhaleva Z.A., Tkachev A.G., Popov A.I. Modification of construction materials by carbon nanotubes: Actual development trends. *Nanotechnologies in Construction* [*Nanotekhnologii v stroitelstve*], 2012, issue 6, pp. 57-69 (Rus).

14. Tolchkov Yu.N., Panina T.I., Mikhaleva Z.A., Galunin E.V. Memetov N.R., Tkachev A.G. The effect of surfactants on the distribution of carbon nanomaterials in aqueous dispersions during nanomodification of construction composites. *Chemical Physics and Mesoscopy* [*Khimicheskaya fizika i mezoskopiya*], 2017, vol. 19, issue 2, pp. 292-298 (Rus).

15. Tolchkov Yu.N., Mikhaleva Z.A. [Development of nanomodifying additives based on CNM "TAUNIT" in construction composites]. *Aspects of Noospheric Security in the Priority Areas of Human Activities: Materials of the 2-nd International. Cluster Scientific-Practical Conference.,* Tambov, 2011, pp. 68-69 (Rus).

16. Gabidullin M.G., Zhuzin A.F., Rakhimov R.Z., Tkachev A.G., Mikhaleva Z.A., Tolchkov Yu.N. Ultrasonic treatment – An effective method of dispersing carbon nanotubes in the bulk of a construction composite. *Construction Materials* [*Stroitelnye materialy*], 2013, issue 3, pp. 57-59 (Rus).

17. Staroverov V.D. [The effect of nanostructured mixing water on the properties of cement composites]. *Actual Issues of Modern Construction: Materials of the 60-th Scientific-Technical Conference of Young Researchers*. Saint-Petersburg, 2007, part. I, pp. 178-183 (Rus).

18. Ponomarev A.N., Egorushkin V.E., Melnikova N.V., Bobenko N.G. [Reconstruction of the "phase separation – Ordering" type and specific heat in carbon]. *AIP Conference Proceedings*, 2014, vol.1623, pp. 503-506.

19. Staroverov V.D., Pukharenko Yu.V. [Scientific basis of application of carbon nanoparticles of fulleroid type in cement composites]. *International Nanotechnology Forum* [*Mezhdunarodyi Forum po Nanotekhnologiyam*]. Moscow, 2009, Access: http://rusnanotech09.rusnanoforum.com/Home.aspx. (Rus).

20. Pukharenko Yu., Aubakirova I., Staroverov V. Structural features of nanomodified cement stone. *Architecture and Engineering*, 2016, vol. 1, issue1, pp. 66-70.

21. Paschenko A.A. (Ed.). The theory of cement. Kiev: Builder (Budivelnik), 1991, 168 p. (in Rus).

22. Musso S., Tulliani J.-M., Ferro G., Tagliaferro A. Influence of carbon nanotubes structure on the mechanical behavior of cement composites. *Composites Science and Technology*, 2009, vol. 69, issue 11-12, pp. 1985-1990.

23. Tokarev Y., Ginchitsky E., Sychugov S., Krutikov V., Yakovlev G., Buryanov A., Senkov S. Modification of Gypsum Binders by Using Carbon Nanotubes and Mineral Additives. *Procedia Engineering*, 2017, vol.172, pp. 1161-1168.

24. Tokarev Y., Ginchitsky E., Sychugov S., Krutikov V., Yakovlev G., Buryanov A., Senkov S. Modification of Gypsum Binders by Using Carbon Nanotubes and Mineral Additives. *Procedia Engineering*, 2017, vol. 172, pp. 1161-1168.

25. Gordina, A.F., Tokarev, Yu.V., Maeva, I.S., Keriene, Ya., [Gypsum compositions with ultra- and nanodispersed modifiers] *Nanotechnology for green and sustainable construction* [in Proc. of the Fourth International Conference]. Cairo, Egypt, 2012, pp. 15-21.

DOI: 10.17277/amt.2018.03.pp.057-062

Ensuring a Temperature Conditions in a Reactor for Functionalization of Carbon Nanotubes

D.V. Tarov*, T.P. Dyachkova, E.N. Tugolukov, I.N. Shubin, V.P. Tarov

Tambov State Technical University;
106, Sovetskaya ul., Tambov, 392000, Russia

* Corresponding author. Tel.: +7 915 660 26 53. *E-mail*: *postmaster@kma.tstu.ru*

Abstract

The problem of providing a temperature conditions in a stirrer-equipped capacitive device is considered for the functionalization of carbon nanotubes using titanium stearate in a nanodispersed liquid medium, with a supply of carbon dioxide. The analysis of mixing methods and set-up of the temperature conditions in the reactor was carried out. Based on the differential equations of heat conductivity, a mathematical model of the temperature field of a flow moving in the mode of ideal displacement through a channel of constant cross section formed by the surfaces of the half-tube and the body was developed. The calculation of the temperature field over the current time interval includes multiple solutions of heat conductivity problems with subsequent consideration of all the components of the local heat balance. Based on the results of the calculations, the dependences of changes in the temperature of the nanodispersed medium in the capacitive reactor on the beginning time and the relative half-tube length were plotted.

Keywords

Capacitive reactor; casing; functionalization; carbon nanotubes; temperature field; mathematical model; assumptions; nanodispersed system.

Introduction

Any complex technology passes through a series of stages constituting a kind of life cycle – from the origin of the idea to the immediate application. Forming the reactor shape makes it possible to determine the ways of solving problems, for which the technology of functionalization is developed [1].

The reactor is understood herein as a combination of indicative basic properties and relationships between its elements, which determine its capabilities and mechanisms of its implementation. The reactor is a set of elements and means adapted and technically suitable for protection against negative environmental influences, which are in relationships with each other and form a certain integrity and unity.

In the present work, we will characterize a batch functionalization reactor, the components of which are as follows:

– components reflecting the arrangement of the reactor elements and the nanodispersed (working) medium in space;

– components reflecting the state of the nanodispersed medium, zones of environmental impact, reactor loading/unloading, etc.

Features of functionalization of carbon nanotubes with titanium stearate

The initial (stock) solution of triethanolamine stearate and triethanolamine titanate has a slightly alkaline reaction and is stable at this pH value [2, 3]. This system also acts as a surfactant for dispersion of carbon nanotubes (**CNTs**). When the pH is lowered, which is achieved by saturation of the nanodispersed medium (solution mixture) with carbon dioxide, the system loses stability, and titanium stearate precipitates on the surface of hydrophilic CNTs. The loss of stability of the system is probably due to protonation of the amine group bound to the chelate complex together with the titanium atom. In this case, the stability of the complex decreases, and the titanium ion binds to the stearate anion and carboxyl groups on the CNT surface.

The triethanolamine is transferred to its carbonate and bicarbonate. Theoretically, all the titanium from the initial solution should be deposited over the CNT surface.

In the reactor considered herein, the nanodispersed mixture containing CNTs was saturated with carbon dioxide at the interface of the contacting phases, without gas bubbling. The amount of the liquid (fluid) adsorbed by the gas depends, first of all, on the properties and size of the contact surface [4, 7].

The paper [5] showed the emergence of destructive changes during the CNT covalent functionalization, which can negatively affect the quality of CNTs and the mechanical and electrophysical properties of composites modified with them. In this case, it is possible to ensure conditions for chemical treatment, under which CNTs with a given value of the degree of functionalization retain the structure of graphene layers.

According to the given scheme, CNTs functionalized with titanium stearate with the required parameters can be obtained by strictly observing the temperature conditions, including the heating of the reaction mass and maintenance of its temperature during the process being implemented [6].

Maintenance of the required temperature conditions of the working medium in the reactor depends on the way it is stirred, namely:

– hydrodynamic mixing by means of a pump and bypass contour providing the feeding of the nanodispersed medium from the bottom of the reactor to its upper zone and subsequent film flow of the medium with adsorption of carbon dioxide;

– stirring the nanodispersed medium by means of a stirrer located inside the reactor.

In the first case, the temperature conditions of the nanodispersed medium in the functionalization reactor are maintained by means of a typical external heat exchanger placed in the bypass loop. From outside, the reactor shell is covered with a thermal insulation layer.

In the second case, the temperature conditions of the nanodispersed medium are maintained by heating the vessel through the heat exchange casing. The latter is also covered externally by the above-mentioned layer. Here, using a capacitive cylindrical device of a vertical design with an elliptical bottom, a mixing device and outer casing seems the most rational option.

Construction of a mathematical model of the reactor temperature conditions

The purpose of mathematical modeling of heat transfer in the reactor casing is to determine the operating modes of the device that ensure the implementation of the liquid-phase functionalization of CNTs under industrial conditions.

The problem of optimization of thermal processes in capacitive reactors can be formulated as follows. It is necessary to find the surface of the casing (Fc), the form (vt) and the initial temperature ($t_{0\text{cool}}$) of the coolant in the casing, and the duration of reactor operation cycles requiring supply or removal of a large amount of heat (τ), under which the coolant operating costs are minimal when using the capacitive reactor.

When compiling a mathematical model, differential equations of heat conductivity are used. The choice of this approach is based on the following assumptions [8–10]:

– the most reliable data on thermal processes taking place in capacitive reactors can be obtained based on the mathematical modeling of temperature fields of a d medium, a coolant and structural elements that affect the course of thermal processes;

– the calculation of local heat fluxes (flows) through the structural elements of the capacitive reactor makes it possible to recalculate the temperatures of the product and the coolant on the basis of local thermal balances under different conditions of their motion (these calculations are feasible if the temperature fields inside the above-mentioned reactor elements are known);

– the spatial non-stationary temperature field is described by the differential Fourier–Kirchhoff equation, which describes the field based on the fundamental laws of heat transfer in space, taking into account all the thermal effects that occur in the operation of the capacitive reactor;

– the partition of the thermal process into spatially-temporal discrete regions eliminates the need for setting up a non-linear heat conduction problem. Hereafter the isolated discrete region will be called local.

Let us consider the derivation of an equation describing the temperature situation in the casing, which provides the operating temperature in the nanodispersed medium when supplying carbon dioxide from above. The coolant moves along the channel formed by the outer wall of the reactor vessel and the inner wall of the casing half-tubes. In deriving the equation, the following assumptions are used:

– the temperature of the coolant along the half-tube channel section is constant;

– the coolant represents an incompressible fluid;

– the thermophysical characteristics of the coolant do not depend on the temperature;

– the cross-sectional area of the annular channel is constant.

The assumption of the independence of the coolant thermophysical characteristics on the temperature is due to the insignificant size of the half-tube channel. Let us consider the non-stationary temperature conditions. The coolant flushes the channel walls at two different temperatures varying in time and along the length of the elementary region. The temperature field of the capacitive reactor coated with the half-tube casing presents a combination of the following temperature fields:

– temperature field of the working medium in the reactor;

– temperature field of the coolant flow in the half-tube casing channels;

– the temperature field of the thermally insulated sections of the reactor vessel not covered with the half-tube casing channels;

– the temperature field of the reactor vessel sections in contact with the coolant flow in the half-tube casing;

– the temperature field of the heat-insulated half-tube wall.

When developing a mathematical model, the following assumptions are made:

– the working medium in the device is considered in the ideal mixing mode, its temperature varies only in time;

– the coolant in the half-tube casing channel is considered in the turbulent conditions of ideal displacement, its temperature varies along the channel length and in time;

– the above-mentioned temperature fields are considered as sets of local temperature fields for discretized space-time regions, within each of which the thermal physical characteristics of substances and structural materials, as well as the kinetic characteristics of thermal processes, are considered constant, corresponding to the average temperatures of the components in the considered regions.

For each local region, the following assumptions can be made:

– the temperature field of the working medium in the reactor is determined from the heat balance conditions taking into account all operating heat sources;

– the temperature field of the coolant flow in the half-tube casing channels is simulated by the solution of the corresponding Cauchy problem;

– the temperature field of the heat-insulated sections of the device vessel not covered by the half-tube casing channels is simulated by the problem of stationary thermal conductivity for a hollow two-layered cylinder;

– the temperature field of the device vessel sections in contact with the coolant flow in the half-tube casing is simulated by the problem of stationary thermal conductivity for a hollow single-layered cylinder;

– the temperature field of the heat-insulated half-tube wall is simulated by the problem of stationary thermal conductivity for a hollow two-layer cylinder;

– the longitudinal heat flow in the device vessel wall is simulated by the solution of the corresponding boundary value problem.

The temperature field of a flow moving in the conditions of ideal displacement through a channel of constant cross section formed by two surfaces with different temperatures is described by the following equation

$$\frac{d\,t(x)}{d\,x}+K\,t(x)=S, \tag{1}$$

$$K=\frac{\alpha_1 P_1+\alpha_2 P_2}{Gc},\ S=\frac{\alpha_1 P_1 t_{F1}+\alpha_2 P_2 t_{F2}}{Gc}, \tag{2}$$

where x is the spatial coordinate in the flow direction, $t(x)$ is the current fluid temperature, G is the mass flow rate of the liquid, c is the heat capacity of the liquid, P_i is the perimeter of the i-th channel wall, α_i is the convective heat transfer coefficient from the i-th wall channel to the liquid, t_{Fi} is the temperature of the i-th channel wall, $i = 1, 2$ is the channel surface index.

Under the initial condition of $t(0)=t_0$, the solution of equation (1) has the following form:

$$t(x)=V+(t_0-V)\exp(-K\,x), \tag{3}$$

$$V=\frac{\alpha_1 P_1 t_{F1}+\alpha_2 P_2 t_{F2}}{\alpha_1 P_1+\alpha_2 P_2}. \tag{4}$$

The average temperature of the liquid in the section of length Δx is

$$\bar{t}=\frac{1}{\Delta x}\int_0^{\Delta x} t(x)dx=V+\frac{(t_0-V)}{K\,\Delta x}(1-\exp(-K\,x)). \tag{5}$$

The problem of stationary thermal conductivity for a hollow two-layered unbounded cylinder is as follows:

$$\frac{d^2 t_i(r_i)}{d\,r_i^2}+\frac{1}{r_i}\frac{dt_i(r_i)}{d\,r_i},\qquad i=1,2,\ R_{i-1}\le r_i\le R_i; \tag{6}$$

$$\lambda_1\frac{d\,t_1(R_0)}{d\,r_1}-\alpha_1(t_1(R_0)-t_{c1})=0; \tag{7}$$

$$\lambda_2 \frac{d t_2(R_2)}{d r_2} + \alpha_2 (t_2(R_2) - t_{c2}) = 0; \quad (8)$$

$$t_1(R_1) = t_2(R_1); \qquad \lambda_1 \frac{d t_1(R_1)}{d r_1} = \lambda_2 \frac{d t_2(R_1)}{d r_2}. \quad (9)$$

Here, $t_i(r_i)$ is the temperature field of the i-th layer of the cylinder, °C, as a function of the radial coordinate r_i, m; R_i is the outer radius of the i-th layer of the cylinder, m; λ_i is the thermal conductivity of the material of the i-th layer of the cylinder, W/(m·K); α_1, α_2 are the coefficients of heat transfer from the cylinder surfaces to the internal and external media, res pectively, W/(m^2·K); t_{c1}, t_{c2} are the medium temperatures from the inner and outer sides, respectively, °C.

The solution of the problem (6) – (9) has the form:

$$t_i(r_i) = A_i + B_i \ln(r_i) - \frac{q_i r_i^2}{4\lambda_i}, \quad (10)$$

where

$$B_1 = \frac{t_{c2} - t_{c1} + V}{\ln\left(\frac{R_1}{R_0}\right) + \frac{\lambda_1}{\lambda_2}\ln\left(\frac{R_2}{R_1}\right) + \lambda_1\left(\frac{1}{R_2\alpha_2} + \frac{1}{R_0\alpha_1}\right)}; \quad (11)$$

$$A_1 = t_{c1} + \frac{q_1 R_0}{2}\left(\frac{R_0}{2\lambda_1} - \frac{1}{\alpha_1}\right) - B_1\left(\ln(R_0) - \frac{\lambda_1}{\alpha_1 R_0}\right); \quad (12)$$

$$B_2 = \frac{\lambda_1}{\lambda_2} B_1 + \frac{R_1^2 (q_2 - q_1)}{2\lambda_2}; \quad (13)$$

$$A_2 = t_{c2} + \frac{q_2 R_2}{2}\left(\frac{R_2}{2\lambda_2} + \frac{1}{\alpha_2}\right) - B_2\left(\ln(R_2) + \frac{\lambda_2}{\alpha_2 R_2}\right); \quad (14)$$

$$V = \frac{q_2}{4\lambda_2}\left(R_2^2 - R_1^2\right) - \frac{R_1^2}{2\lambda_2}(q_2 - q_1)\ln\left(\frac{R_2}{R_1}\right) + \frac{q_2 R_2}{2\alpha_2} - \frac{R_1^2}{2\alpha_2 R_2}(q_2 - q_1) + \frac{q_1}{4\lambda_1}\left(R_1^2 - R_0^2\right) + \frac{q_1 R_0}{2\alpha_1}. \quad (15)$$

The problem of stationary thermal conductivity for a hollow single-layered unbounded cylinder is as follows:

$$\frac{d^2 t(r)}{d r^2} + \frac{1}{r}\frac{d t(r)}{d r} = 0, \qquad R_1 \le r \le R_2; \quad (16)$$

$$\lambda \frac{d t(R_1)}{dR} - \alpha_1 (t(R_1) - t_{c1}) = 0; \quad (17)$$

$$\lambda \frac{d t(R_2)}{dR} + \alpha_2 (t(R_2) - t_{c2}) = 0. \quad (18)$$

Here $t(r)$ is the temperature field of the cylinder, °C, as a function of the radial coordinate r, m; R_1, R_2 are the inner and outer radii of the cylinder, respectively, m; λ is the thermal conductivity of the cylinder material, W/(m·K); α_1, α_2 are the coefficients of heat transfer from the cylinder surfaces to the internal and external media, respectively, W/(m^2·K); t_{c1}, t_{c2} are the medium temperatures from the inner and outer sides, respectively, °C.

The solution of the problem (16) – (18) has the form:

$$t(r) = A\ln(r) + B; \quad (19)$$

$$B = t_{c1} + A\left(\frac{\lambda}{\alpha_1 R_1} - \ln(R_1)\right); \quad (20)$$

$$A = \frac{t_{c2} - t_{c1}}{\frac{\lambda}{\alpha_2 R_2} + \frac{\lambda}{\alpha_1 R_1} + \ln\left(\frac{R_2}{R_1}\right)}. \quad (21)$$

The longitudinal heat flow in the vessel wall is determined on the basis of mathematical modeling of the longitudinal temperature distribution in the corresponding structural element.

$$\frac{d^2 T(x)}{d x^2} - k^2 T(x) = 0; \quad (22)$$

$$T(0) = t(0) - \frac{m}{k^2}; \quad (23)$$

$$\frac{d T(L_x)}{d x} = 0; \quad (24)$$

$$k^2 = \alpha_1 + \alpha_2; \; m = \frac{(\alpha_1 t_1 + \alpha_2 t_2)}{\lambda h}; \; T(x) = t(x) - \frac{m}{k^2}. \quad (25)$$

Here, x is the spatial longitudinal coordinate, m; $T(x)$ is the temperature field, °C; t_1, t_2 are the ambient temperatures, °C; λ is the coefficient of thermal conductivity of the structural material W/(m·K); α_1, α_2 are the coefficients of convective heat transfer from the external surfaces of the structural element to the environment, W/(m$_2$·K); L_x is the length of the section considered in the heat flow direction, m; h is the thickness of the structural element, m.

The solution of problem (22) – (24) has the form:

$$T(x) = C_1 \operatorname{ch}(k x) + C_2 \operatorname{sh}(k x), \quad (26)$$

where

$$C_1 = t(0) - \frac{m}{k^2}; \quad (27)$$

$$C_2 = -C_1 \operatorname{th}(k L_x). \quad (28)$$

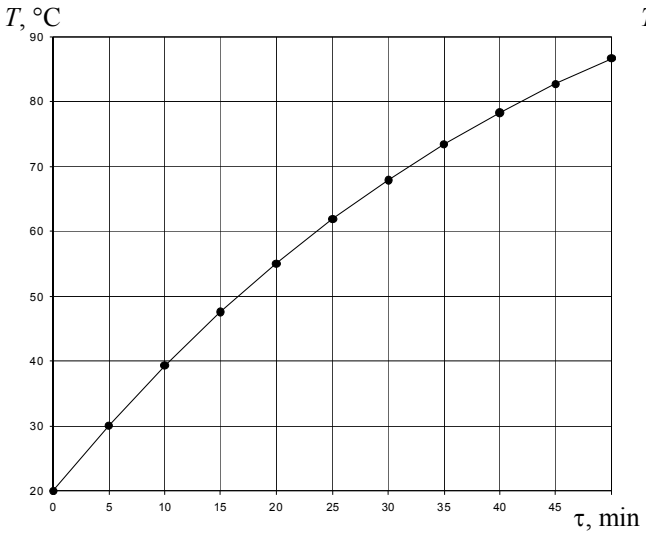

Fig. 1. Temperature changes in the reactor

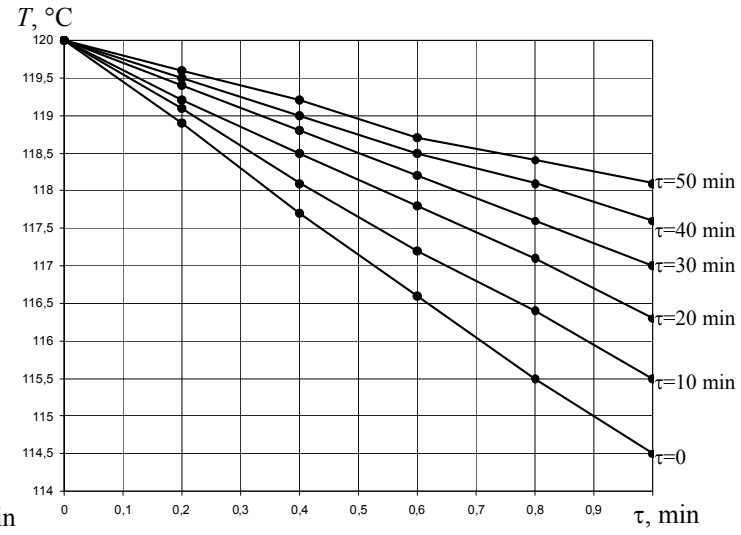

Fig. 2. Change in temperature by the relative length of the half-tube (0–1) as a function of time (0–50 min)

Thus, the calculation of the temperature field of the device for the current time interval includes a multiple solution of the above-mentioned heat conduction problems with subsequent consideration of all the components of the local heat balance. An iterative algorithm involving multiple uses of the solutions of the problems considered is due to the necessity of matching the temperature fields of the interacting components of the system through the appropriate boundary conditions.

In the modeling and design of the capacitive reactor, two main tasks can be distinguished, which include the calculation of the non-stationary temperature field:

– determination of the non-stationary temperature field in the working area according to the geometric dimensions of the reactor, the coolant flow and the initial temperature distribution in all the reactor elements;

– determination of the conditions and design parameters ensuring the functioning of the capacitive reactor. This task is solved most often.

The adequacy of the mathematical model of the capacitive reactor was verified by comparing the calculated data with the results of experiments carried out under laboratory conditions. The deviation of the experimental values from the calculated values does not exceed 10 %. Taking into account the results of the calculation of the non-stationary temperature field in the half-tube casing (number of approaches-4, number of turns in the approach-2), a rector for preparing a nanodispersed suspension was designed to functionalize CNTs having a weight of 300 kg, with the AMT-300 oil used as coolant.

Fig. 1 demonstrates the calculated temperature changes in the reactor resulting from the calculation (abscissa axis – time, min, ordinate axis – temperature, °C).

The graph shown in Fig. 2 indicates a high uniformity in the heating of the nanodispersed medium and a relatively fast beginning of the conditions (the abscissa axis is the relative length of the half-tube approach, and the ordinate axis is the temperature, °C).

At the initial moment of time, the temperature difference was 5.5 °C for the entire half-tube length, whereat after 50 min, at the time of the beginning of the conditions, it was only 1.8 °C due to the heating of the structure.

Conclusions

When using a capacitive device, a large number of operations are carried out for processing liquid products: heating, cooling, aging of liquids; distillation of volatile fractions; chemical transformations; dissolution of granular and bulk materials; mixing of liquids; and partial loading of components. In real production processes, various combinations of these operations take place. As a rule, all of them occur in non-stationary temperature conditions. The design of the half-tube casing makes it possible to control the temperature conditions in the reactor by disconnecting the section (approach) both at full and partial loading of the reactor volume.

References

1. Dyachkova T.P., Tkachev A.G. [*Methods of functionalization and modification of carbon nanotubes*]. Moscow, Spectrum, 2013, 152 p. (Rus)

2. Khokhlov P.A., Melezhik A.V., Tkachev A.G. [Functionalization of carbon nanotubes by organotitanates]. *Vestnik VGU*, 2013, issue 1, p. 52-55. (Rus)

3. Tarov D.V., Gurova T.V., Shubin I.N. [Instrumental registration of the functionalization of carbon nanotubes by titanium stearate]. *Vestnik TGTU*, 2015, vol. 21, issue 2, pp.360-366. (Rus)

4. Kondratyuk I.V., Shubin I.N., Tarov D.V. [Technology for the production of hydrophilic carbon nanotubes]. *Fundamental and applied scientific research: a collection of articles of the international scientific and practical conference. In two parts of Part 1*. Ufa OMEGA SAINS, 2016, pp. 3-5. (Rus)

5. Dyachkova T.P., Rukhov A.V., Tugolukov E.N., Usol'tseva N.V., Khan Yu. A., Chapaksov N.A. Studies on the changes in the structure of carbon nanotubes grapheme layers after functionalization using Raman spectroscopy-based method. *Liquid Crystals and Their Application*, 2017, issue 4, pp. 83-89.

6. Dyachkova T.P., Tugolukov E.N., Anosova I.V., Tkachev A.G. Kinetic Study of Functionalization of Carbon nanomaterials. *Nanotech France 2015: International Nanotechnology Conference*. Pôle Universitaire Léonard de Vinci, La Défense, Paris, France, 2015, p. 57.

7. Tarov D.V., Solodovnikova S.V., Shubin I.N. A line for the preparation of multifunctional oleophilic multi-walled carbon nanotubes. *Increasing the efficiency of resource use in the production of agricultural products – new technologies and technology of a new generation for crop production and livestock: a collection of scientific papers*. Tambov: R.V. Pershin's Publishing House, 2015, pp. 227-230 (Rus)

8. Shubin I.N. et al Technological foundations for the functionalization of multi-walled carbon nanotubes with titanium stearate for subsequent production of composites. *Vestnik TGTU*, 2016, vol. 3, issue 22, pp. 501-509. (Rus)

9. Tugolukov E.N. *Solving the problems of thermal conductivity by the method of finite integral transformations in the automated design of technological equipment of the chemical industry*. Tambov, TSTU Pulishing House. 2006. 116 p. (in Rus)

10.Tugolukov E.N. *Mathematical Modeling of Process Equipment for Multi-Assortment Chemical Production*. Moscow, Mashinostroenie-1, 2004, 100 p. (Rus)

DOI: 10.17277/amt.2018.03.pp.063-069

A New Physical Method of Localization of Nanomechanical Action of Magnetic Nanoparticles Controlled by Low-Frequency Magnetic Field on Mechanically Sensitive Biochemical Systems

A.O. Zhigachev[1], Yu.I. Golovin[1–3]*, N.L. Klyachko[2, 3]

[1] *G.R. Derzhavin Tambov State University, 33, St. Internationalnaya, Tambov, 392000, Russia;*
[2] *Lomonosov Moscow State University, p. 3, 1, Leninskie Gory, GSP-1, Moscow, 119991, Russia;*
[3] *National Research Technological University "MISiS", 4, Leninsky prosp., Moscow, 119991, Russia*

* Corresponding author. Tel.: +7 (4752) 53 26 80. *E-mail*: nano@tsutmb.ru

Abstract

Magnetic/superparamagnetic nanoparticles (**MNPs**) controlled by an external magnetic field (**MF**) have a great potential for various biomedical applications. The MNPs make it possible to provide selective nanomechanical impact at the level of individual molecules of the intended type by means of their magnetomechanical actuation in the low-frequency MF. However, the MNPs introduced into the bloodstream can accumulate in many organs, creating the hazard of unexpected side effects that may occur when activating alternating MF is turned on. In this paper, we propose a new physical method and technology of localization of the MNP impact on the biochemical system, by creating a static gradient localizing MF with a field free point near the center of the magnetic system. Under these conditions, the activating alternating MF stimulates only those MNPs that are in the vicinity of the field free point. Far from it, where the localizing MF is higher than the stimulating alternating MF, the MNPs are "frozen" in static field and are not affected by the weaker activating alternating MF. The shape and size of the impact localization region are studied depending on the characteristics of the localizing and activating MF.

Keywords

Magnetic nanoparticles; non-heating low-frequency magnetic field; localization; magnetomechanical impact.

Introduction

Magnetic nanoparticles (**MNPs**) have long been used as contrast agents in magnetic resonance imaging [1–3] and in anticancer magnetic hyperthermia (**MHT**) [4–7]. The latter is based on the fact that in the radiofrequency (100–700 kHz) magnetic field, MNPs are capable of releasing heat intensively, which leads to the induction of apoptosis and the subsequent ablation of malignant cells. However, the potential of using MNPs in biomedicine is incomparably larger than these two applications. The MNPs are promising in targeted drug delivery technologies as transducers of an external magnetic field that controls the movement of containers with a therapeutic agent into the desired area or triggers a controlled drug release with a given rate [8–11].

In the last decade, a new magnetomechanical approach to control the behavior of MNPs for innovative biomedical technologies has emerged. It uses the conversion of the magnetic field energy to the mechanical motion of single-domain MNPs and is referred to as magnetomechanical activation (**MMA**) [12–15]. For the MMA, a non-heating low-frequency alternating magnetic field (**AMF**) with a frequency of 1–1000 Hz is used, which causes the oscillating translational or rotational motion of the MNPs. The motion of particles can be used for nanoscale deformation of biologically and chemically active macromolecular structures, such as, membranes and enzymes. As a rule, for this purpose, the MNPs are functionalized with the help of molecular-specific ligands. A number of experimental studies have shown that within the MMA, the functionalized MNPs can be

used to control the vital activity of cells in tissue engineering [12,16–18], as well as drugless cancer therapy [19–24] by direct nanomagnetomechanical cell destruction without the use of either chemo- or radiotherapy. However, because of poorly developed theoretical basis, most of the works do not have good physical justification with respect to the choice of parameters of the magnetic field and are of search character.

In a number of works of Golovin et al. attempts have been made to develop the theoretical basis of the MMA [25–28]. For instance, in [26], a characteristic frequency was found theoretically, connecting the main parameters of the MNP, alternating magnetic field and viscous medium according to the following expression $\omega_c = \mu\mu_0 H_a / 6\eta V_{HD}$, where μ is the magnetic moment of the MNP, μ_0 is the magnetic constant, H_a is the AMF amplitude, η is surrounding medium viscosity, V_{HD} is a hydrodynamic volume of the particle. If low-frequency AMF is below ω_c, functionalized MNPs with a radius of the magnetic core more than some critical (~ 5–10 nm for different magnetic materials) blocking Néel relaxation, perform oscillational-rotational movements with a sweep close to 180°, deforming the associated macromolecules. The force generated by MNPs is sufficient to change the state of such macromolecular structures as micellar/vesicular nanocontainers and cytoplasmic cell membranes. In addition, nanoscale deformations of enzymes, membrane receptors, and ion channels can change their activity [29] due to changes in angles and interatomic distances in their active centers. Experimental studies confirm the main conclusions of theoretical studies [30–32].

The success of *in vitro* experiments stimulate the testing of MMA *in vivo* for various purposes. The technological platform based on MMA makes it possible to selectively influence artificial nanocontainers for the purpose of targeted delivery and controlled release of medicines, drugless oncotherapy, regenerative medicine, and unlike the heat field in MHT, the nanomechanical action of the MNPs does not spread spontaneously in the volume of tissue due to thermal conductivity, but it is localized at the molecular or nano-scale. For *in vivo* purposes, functionalized MNPs are usually administered intravenously, since this is the only way to ensure their successful delivery to the target tissue in the internal organs and anchoring on the targeted cell type or even molecular groups. The problem is that a significant quantity of particles are captured by the liver, kidneys, spleen, i.e. chemical modification and vectorization is not enough for the macroscopic localization of the MNPs distribution. Thus, to various extent, all tissues covered by external activating AMF, in which the MNPs were accumulated, are subjected to nanomechanical impact. This creates the risk of side effects.

The physical approaches to the macroscopic impact localization are usually based on the localization of MNPs themselves through a gradient magnetic field created by a sharpened pole of a permanent magnet or electromagnet [33]. However, such localization methods are effective only when MNPs are concentrated in thin limbs, other appendages of the body of small laboratory animals or superficial regions. Focusing of the MNPs in the deep tissues is a very challenging task [34, 35]. Another method of concentrating MNPs in the desired region is described in [36] and it is based on alignment of the magnetic moments of rod-like MNPs in the direction of magnetic field and subsequent pushing of the MNPs by rapidly switching the direction of the magnetic field. The application of such an approach in a living organism can be associated with certain difficulties, since viscous biological structures will prevent the translational movement of the MNPs. In addition, when moving the MNPs in various areas of a living organism, the viscosity will be different, which will lead to their uneven, non-synchronous movement and, leading to MNPs deconcentration.

In connection with the foregoing, the purpose of this research is to develop new physical method and technology for the macroscopic localization of the nanoscale effect of the MNPs, to determine the optimal configuration of the electromagnetic coil system that provides the best spatial resolution, to analyze the dependence of the geometric dimensions of the localization region on the parameters of the localizing magnetic system creating a gradient magnetic field , and to assess the maximum scanning speed of a mechanically sensitive biochemical system.

Methods and approaches

A new method for localizing the nanomechanical action consists in generation of an additional localizing gradient field H_{gr} with a field free point near the center of the magnetic system (Fig. 1). The main idea is that under the influence of an external AMF with an amplitude H_a on MNPs in such a magnetic field system, there exists a region of space with linear size $L \approx 2H_a / \mathrm{grad}(H_{gr})$, in which the MNPs can perform oscillational-rotational motions under the action of an external activating AMF (Fig. 1), nanomechanically affecting associated molecules. Outside this region,

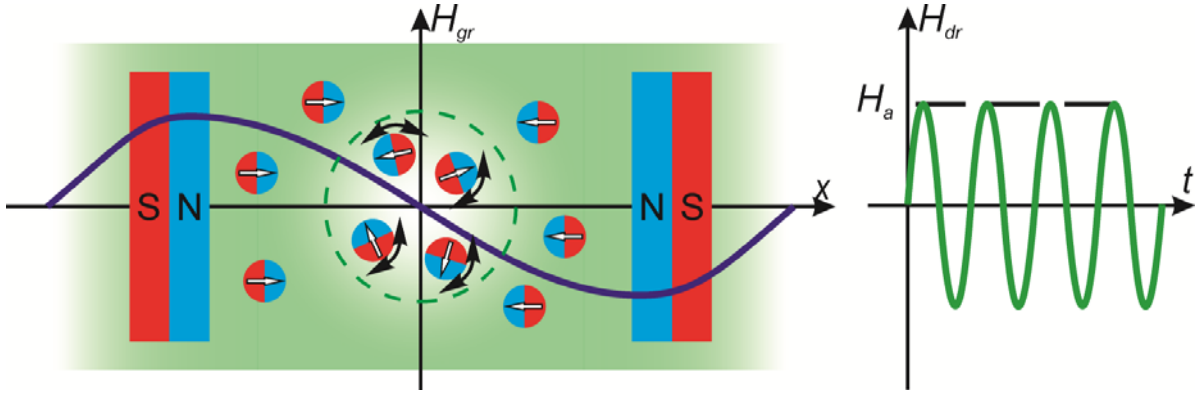

Fig. 1. A diagram illustrating the method developed. The localizing gradient field H_{gr} (on the left) selects the region (green dashed line), outside which MNPs are "frozen" under the action of the activating AMF H_{dr}

the total magnetic field will not change its direction when the magnitude and direction of the activating AMF are changed. Thus, the MNPs will be "frozen" in the constant gradient field H_{gr}, ensuring that cells and tissues outside the impact region are not subjected to unintended effects of the oscillational-rotational motion of the MNPs.

As far as AMF impact localization region (**LR**) position in space is fully specified by field free point coordinates proposed physical localization method involves control over LR positioning. This possibility can be employed by creating additional homogeneous magnetic fields that change the position of the field free point, for example by means of Helmholtz coils (Fig. 2). In such case displacing magnetic field magnitude can be easily tuned by changing coil current. Assuming three orthogonal pairs of coils

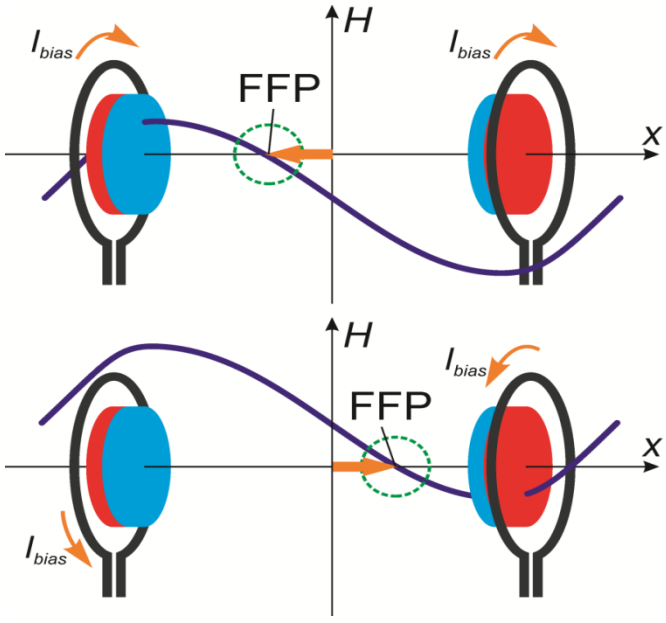

Fig. 2. Displacement of the field free point (FFP) using additional homogeneous field

proposed method creates opportunity for consequent step-by-step scanning of desired region with custom 3D shape.

In order to study the LR size dependence on configuration of the localizing system, three types of model systems that create a constant gradient magnetic field with a field free point using electromagnetic coils were considered:

i) a pair of coils arranged in the Maxwell system;

ii) two orthogonally placed pairs of coils arranged in the Maxwell system;

iii) a pair of concentric coils.

To compare the LR sizes, we selected the following coil parameters: the coil cross section was 5×5 mm^2, the average radius was 15 mm, except for the case of a pair of concentric coils, where the radii were 10 and 20 mm, and the number of turns was 25. The current in the pair of coils i) and iii) was chosen to be 10 A for definiteness, and in two pairs of coils ii) equal to 5 A, to equal electric power of the systems. The control AMF was chosen equal to 0.8 kA/m (~ 1 mT) for definiteness.

In addition, a localizing system consisting of a pair of permanent magnets was examined to determine whether it could be used for simple demonstration experiments. The main parameter of permanent magnets is remnant magnetization, it was chosen equal to 1.2 T, which corresponds to the most common NdFeB magnets.

In this paper, the finite element method was used to model the distribution of the magnetic field.

Results

1. Determination of the optimal configuration of the localizing system

As a result of gradient magnetic field distribution calculation for three model systems described above, the following dimensions of the AMF localization region were found:

i) $1.05 \times 2.04 \times 2.04$ mm^3;
ii) $1.4 \times 1.4 \times 7.5$ mm^3;
iii) $2.77 \times 3.06 \times 3.06$ mm^3.

These findings indicate that under identical conditions the geometry of a pair of Maxwell coils allows obtaining a higher level of localization in comparison with two pairs of coils and a pair of concentric coils. The larger size of the impact LR created by the two pairs of coils is due to the fact that the second pair introduces a magnetic field component directed opposite to the field vectors of the first pair of coils, thereby weakening the gradient of the first pair of coils.

2. Determination of achievable sizes of the localization region using permanent magnets

Proceeding from the obtained distributions of the static gradient MF, the LR dimensions of the AMF action with amplitude of 8 kA/m (~ 10 mT) were determined for the distances between magnets lying in the range from 40 to 90 mm with 10 mm increment. The data obtained is presented in Table 1.

In cross section LR shape is close to ellipse, in three-dimensional space it is ellipsoid-like figure which eccentricity varies depending on the distance between the magnets.

3. Estimation of the maximum scanning speed of a mechanically sensitive biochemical system

Let us estimate the maximum speed of sequential exposure of the target areas of the mechanically sensitive biochemical system by changing the position of the field free point. Suppose, for simplicity, that to change the state of the biochemical system in the region of the action, it is necessary to act by AMF for some number of field periods, while the needed to change position of the field free point can be neglected in comparison with the time of continuous exposure of the LR to the AMF. Then the maximum scanning speed of the mechanically sensitive biochemical system can be expressed approximately as $V_{loc} f / N_{eff}$. Here, the minimum exposure time is assumed to be equal to N_{eff} / f, where N_{eff} is the number of AMF periods leading to perceptible biological response, V_{loc} is the volume of AMF impact LR, and f is the AMF frequency.

To estimate the maximum scanning speed, it was accepted that $N_{eff} = 100$, and the maximum frequency $f = 1000$ Hz, since at such a low frequency the common MNPs of biomedical use under biological conditions willsweep out the maximum angle during their oscillational-rotational movements, exerting a nanomechanical effect on the associated structures. Thus, the maximum scanning speed can be estimated as $10 V_{loc}$ per second, i.e. ~ 2.3 cm^3/s with the AMF impact localization volume ~ $4 \times 8 \times 8$ mm^3.

Table 1

The dimensions of the section of the localization region of the AMF with an amplitude of 8 kA/m as a function of the distance between the magnets with a remanent magnetization of 1.2 T

Distance between magnets, mm	Longitudinal dimension of LR, mm	Transverse dimension of LR, mm	Volume of LR, mm^3
40	1.56	3.02	14.23
50	2.48	4.90	59.54
60	3.80	7.80	231.19
70	5.92	12.02	855.32
80	8.54	19.10	3115.48
90	12.22	29.96	10968.70

Discussion

The method for AMF impact localization can be implemented both with the help of electromagnetic coils in various configurations and with the help of permanent magnets oriented by the same poles towards each other. However, the results obtained show that permanent magnets can be used successfully only for *in vitro* experiments or for small laboratory animals, since only for such a small volume, the size of the LR can be at the level of $4 \times 8 \times 8$ mm^3 for the AMF with an amplitude of 8 kA/m (~ 10 mT). Therefore, when scaling the presented approach to control the MNPs *in vivo* in the body of large mammals or humans, it will be impossible to achieve such values with the help of permanent magnets; to ensure the appropriate size of the impact LR it is necessary to use the Maxwell electromagnetic coils to create large gradients (> 5 T/m) at considerable distances ~ 0.5 m.

In addition, proceeding from the expression for the scanning speed for a mechanically sensitive biochemical system, it can be seen that in general scanning speed depends on the frequency and volume of the LR, i.e. the spatial localization degree. It is undesirable to choose the frequency of the AMF above 1000 Hz, since the MNPs motions become constrained

due to the increasing role of viscous forces, and the biochemical response in this case may weaken or disappear. Consequently, the scanning speed can be increased mainly by decreasing the gradient of the localizing field.

Thus, the transition to electromagnetic coils has one more advantage – the current variation makes it possible to dynamically change the gradient of the localizing MF, and, consequently, the size and volume of the LR.

One more point to highlight is deconcentration of MNPs which obviously will take place in gradient field. This problem affects only particles that are outside the LR because of their static orientation, while inside MNPs movement in one AMF halfcycle is nearly compensated by movement in the consequent one. The simple solution is periodic change of gradient field direction which will alter MNPs movement direction giving zero average particle displacement during number of gradient field cycles.

Conclusion

We proposed and developed new physical method and technology for non-heating low-frequency AMF impact localization on mechanically sensitive biochemical systems by their nanomagnetomechanical actuation and localization spot positioning allowing scanning of custom shape volume in three dimensional space. The mediators of this action – functionalized MNPs of 20–50 nm in size – perform oscillational-rotational motions when exposed to low-frequency AMF and induce deformations in associated macromolecules. By creating an additional gradient field H_{gr}, a region of local impact with linear dimensions $L \approx 2H_a/\text{grad}(H_{gr})$ is distinguished.

It was found that the localizing magnetic system, built with Helmholtz coils, allows achieving a smaller size of the LR, i.e. a better spatial resolution, in comparison with arrangement consisting of a pair of concentric coils. In this case, one pair of coils allows achieving a greater spatial resolution, in comparison with two pairs of Helmholtz coils, creating a gradient field along two perpendicular directions.

The analysis of the AMF impact LR size using model system consisting of a pair of oppositely oriented permanent magnets showed that the linear dimensions of the localization spot vary squared with increasing distance between the magnets. It was found that permanent NdFeB magnets with a remanent magnetization of ~ 1.2 T can provide localization of the AMF action with an amplitude of 8 kA/m in the region of less than $4 \times 8 \times 8$ mm^3, which is sufficient for laboratory experiments *in vitro* or on small laboratory animals *in vivo*.

As follows from simple assumptions, it was established that the maximum scanning speed for sequential processing of the target area of the biochemical system is about $10V_{loc}$ per second, where V_{loc} is the volume of the localization region. For the simplest localization system using permanent magnets, the maximal scanning speed is ~ 2.3 cm^3/s.

Acknowledgments

The research was supported by grants from the Russian Foundation for Basic Research No. 17-42-680803 (modeling and calculations) and No. 17-54-33027 (experimental setup and experiments).

References

1. Huang J., Zhong X., Wang L., Yang L., Mao H. Improving the magnetic resonance imaging contrast and detection methods with engineered magnetic nanoparticles. *Theranostics*, 2012, vol. 2, issue 1, pp. 86-102. doi: 10.7150/thno.4006

2. Kuda-Wedagedara A.N., Allen M.J. Enhancing magnetic resonance imaging with contrast agents for ultra-high field strengths. *Analyst*, 2014, vol. 139, Issue 18, pp. 4401-4410. doi: 10.1039/C4AN00990H

3. Estelrich J., Sánchez-Martín M.J., Busquets M.A. Nanoparticles in magnetic resonance imaging: from simple to dual contrast agents. *International Journal of Nanomedicine*, 2015, vol. 10, pp. 1727-1741. doi: 10.2147/IJN.S76501

4. Mahmoudi K., Bouras A., Bozec D., Ivkov R., Hadjipanayis C. Magnetic hyperthermia therapy for the treatment of glioblastoma: a review of the therapy's history, efficacy, and application in humans. *International* Journal of Hyperthermia, 2018. doi: 10.1080/02656736.2018.1430867

5. Salunkhe A.B., Khot V.M., Pawar S.H. Magnetic hyperthermia with magnetic nanoparticles: a status review. *Current Topics in Medicinal Chemistry*, 2014, vol. 14, issue 6, pp. 572-594.

6. Ling-Yun Z., Jia-Yi L., Wei-Wei O., Dan-Ye L., Li L., Li-Ya L., Jin-Tian T. Magneticmediated hyperthermia for cancer treatment: Research progress and clinical trials. *Chinese Physics B*, 2013, vol. 22, issue 10, p. 108104. doi: 10.1088/1674-1056/22/10/108104

7. Dutz S., Hergt R. Magnetic particle hyperthermia a promising tumour therapy?

Nanotechnology, 2014, vol. 25, issue 45, p. 452001. doi: 10.1088/0957-4484/25/45/452001

8. Arruebo M., Fernández-Pacheco R., Ibarra M.R., Santamaría J. Magnetic nanoparticles for drug delivery. *Nano today*, 2007, vol. 2, issue 3. pp. 22-32. doi: 10.1016/S1748-0132(07)70084-1

9. Mody V.V., Cox A., Shah S., Singh A., Bevins W., Parihar H. Magnetic nanoparticle drug delivery systems for targeting tumor. *Applied Nanoscience*, 2014, vol. 4, issue 4, pp. 385-392. doi: 10.1007/s13204-013-0216-y

10. Mura S., Nicolas J., Couvreur P. Stimuli-responsive nanocarriers for drug delivery. *Nature Materials*, 2013, vol. 12, issue 11, pp. 991-1003. doi: 10.1038/nmat3776

11. Timko B.P., Dvir T., Kohane, D.S. Remotely triggerable drug delivery systems. *Advanced materials*, (2010), vol. 22, issue 44, pp. 4925-4943. doi: 10.1002/adma.201002072

12. Dobson J., Cartmell S.H., Keramane A., El Haj A.J. Principles and design of a novel magnetic force mechanical conditioning bioreactor for tissue engineering, stem cell conditioning, and dynamic in vitro screening. *IEEE transactions on nanobioscience*, 2006, vol. 5, issue 3. pp. 173-177. doi: 10.1109/tnb.2006.880823

13. Pankhurst Q.A., Connolly J., Jones S.K., Dobson J.J. Applications of magnetic nanoparticles in biomedicine. *Journal of Physics D: Applied Physics*, 2003, vol. 36, issue 13, p. R167. doi: 10.1088/0022-3727/36/13/201

14. Nappini S., Bonini M., Bombelli F.B., Pineider F., Sangregorio C., Baglioni P., Nordèn B. Controlled drug release under a low frequency magnetic field: effect of the citrate coating on magnetoliposomes stability. *Soft Matter*, 2011, vol. 7, issue 3, pp. 1025-1037. doi: 10.1039/C0SM00789G

15. Golovin Y.I., Gribanovsky S.L., Golovin D.Y., Klyachko N.L., Majouga A.G., Master A.M., Sokolsky M., Kabanov A.V. Towards nanomedicines of the future: Remote magneto-mechanical actuation of nanomedicines by alternating magnetic fields. *Journal of Controlled Release*, 2015, vol. 219, pp. 43-60. doi: 10.1016/j.jconrel.2015.09.038

16. Dobson J. Remote control of cellular behaviour with magnetic nanoparticles. *Nature Nanotechnology*, 2008, Vol. 3, Issue 3, pp. 139-143. doi: 10.1038/nnano.2008.39

17. Hu B., Dobson J., El Haj A.J. Control of Smooth Muscle α-actin (SMA) up-regulation in HBMSCs using remote magnetic particle mechano-activation. *Nanomedicine: Nanotechnology, Biology and Medicine*, 2014, vol. 10, issue 1, pp. 45-55. doi: 10.1016/j.nano.2013.06.014

18. Kanczler J.M., Sur H.S., Magnay J., Green D., Oreffo R.O., Dobson J.P., El Haj A.J. Controlled differentiation of human bone marrow stromal cells using magnetic nanoparticle technology. *Tissue engineering Part A*, 2010, vol. 16, issue 10, pp. 3241-3250. doi: 10.1089/ten.tea.2009.0638

19. Choi D.S., Hopkins X., Kringel R., Park J., Jeon I.T., Kim Y.K. Magnetically driven spinning nanowires as effective materials for eradicating living cells. *Journal of Applied Physics*, 2012, vol. 111, issue 7, p. 07B329. doi: 10.1063/1.3678437

20. Contreras M.F., Sougrat R., Zaher A., Ravasi T., Kosel J. Non-chemotoxic induction of cancer cell death using magnetic nanowires. *International Journal of Nanomedicine*, 2015, vol. 10, p. 2141. doi: 10.2147/IJN.S77081

21. Creixell M., Bohorquez A.C., Torres-Lugo M., Rinaldi C. EGFR-targeted magnetic nanoparticle heaters kill cancer cells without a perceptible temperature rise. *ACS Nano*, 2011, vol. 5, issue 9, pp. 7124-7129. doi: 10.1021/nn201822b

22. Hu S.H., Gao X. Nanocomposites with spatially separated functionalities for combined imaging and magnetolytic therapy. *Journal of the American Chemical Society*, 2010, vol. 132, issue 21, pp. 7234-7237. doi: 10.1021/ja102489q

23. Kim D.H., Rozhkova E.A., Ulasov I.V., Bader S.D., Rajh T., Lesniak M.S., Novosad V. Biofunctionalized magnetic-vortex microdiscs for targeted cancer-cell destruction. Nature *Materials*, 2010, vol. 9, issue 2, pp. 165-171. doi: 10.1038/nmat2591

24. Zhang E., Kircher M.F., Koch M., Eliasson L., Goldberg S.N., Renström E. Dynamic magnetic fields remote-control apoptosis via nanoparticle rotation. *ACS Nano*, 2014, vol. 8, issue 4, pp. 3192-3201. doi: 10.1021/nn406302j

25. Golovin Y.I., Klyachko N.L., Golovin D.Y., Efremova M.V., Samodurov A.A., Sokolski-Papkov M., Kabanov A.V. A new approach to the control of biochemical reactions in a magnetic nanosuspension using a low-frequency magnetic field. *Technical Physics Letters*, 2013, vol. 39, issue 3, pp. 240-243. doi: 10.1134/s106378501303005x

26. Golovin Y.I., Klyachko N.L., Sokolsky-Papkov M., Kabanov A.V. Single-domain magnetic nanoparticles as force generators for the nanomechanical control of biochemical reactions by low-frequency magnetic fields. *Bulletin of the Russian Academy of Sciences: Physics*, 2013, vol. 77, issue 11, pp. 1350-1359. doi: 10.3103/s1062873813110130

27. Golovin Y.I., Gribanovskii S.L., Golovin D.Y., Klyachko N.L., Kabanov A.V. Single-domain magnetic nanoparticles in an alternating magnetic field as mediators of local deformation of the surrounding macromolecules. *Physics of the Solid State*, 2014, vol. 56, issue 7, pp. 1342-1351. doi: 10.1134/S1063783414070142

28. Golovin Y.I., Klyachko N.L., Majouga A.G., Sokolsky M., Kabanov A.V. Theranostic multimodal potential of magnetic nanoparticles actuated by non-heating low frequency magnetic field in the new-generation nanomedicine. *Journal of Nanoparticle Research*, 2017, vol. 19, issue 2, p. 63. doi: 10.1007/s11051-017-3746-5

29. Golovin Y.I., Gribanovsky S.L., Golovin D.Y., Zhigachev A.O., Klyachko N.L., Majouga A.G., Sokolsky M., Kabanov A.V. The dynamics of magnetic nanoparticles exposed to non-heating alternating magnetic field in biochemical applications: theoretical study. *Journal of Nanoparticle Research*, 2017, vol. 19, issue 2, p. 59, doi: 10.1007/s11051-017-3753-6

30. Klyachko N.L, Sokolsky-Papkov M., Pothayee N., Efremova M.V., Gulin D.A., Pothayee N., Kuznetsov A.A., Majouga A.G., Riffle J.S., Golovin Y.I., Kabanov A.V. Changing the enzyme reaction rate in magnetic nanosuspensions by a non-heating magnetic field. *Angewandte Chemie International Edition,* 2012, vol. 51, issue 48, pp. 12016-12019. doi: 10.1002/anie.201205905

31. Majouga A., Sokolsky-Papkov M., Kuznetsov A., Lebedev D., Efremova M., Beloglazkina E., Rudakovskaya P.G., Veselov M., Zyk N., Golovin Y.I., Klyachko N.L., Kabanov A.V. Enzyme-functionalized gold-coated magnetite nanoparticles as novel hybrid nanomaterials: Synthesis, purification and control of enzyme function by low-frequency magnetic field. *Colloids and Surfaces B: Biointerfaces*, 2015, vol. 125, pp. 104-109. doi: 10.1016/j.colsurfb.2014.11.012

32. Master A.M., Williams P.M., Pothayee Nik., Pothayee Nip., Zhang R., Vishwasrao H.M., Golovin Y.I., Riffle J.S., Sokolsky M., Kabanov A.V. Remote actuation of magnetic nanoparticles for cancer cell selective treatment through cytoskeletal disruption. *Scientific Reports*, 2016, vol. 6, p. 33560. doi: 10.1038/srep33560

33. Kralj S., Potrc T., Kocbek P., Marchesan S., Makovec D. Design and fabrication of magnetically responsive nanocarriers for drug delivery. *Current medicinal chemistry*, 2017, vol. 24, issue 5, pp. 454-469.

34. Al-Jamal K.T., Bai J., Wang J.T. W., Protti A., Southern P., Bogart L., Heidari H., Li X., Cakebread A., Asker D., Al-Jamal W.T., Shah A., Bals S., Sosabowski J., Pankhurst Q.A. Magnetic drug targeting: preclinical in vivo studies, mathematical modeling, and extrapolation to humans. *Nano letters*, 2016, vol. 16, issue 9, pp. 5652-5660. doi: 10.1021/acs.nanolett.6b02261

35. Shapiro B., Kulkarni S., Nacev A., Muro S., Stepanov P.Y., Weinberg, I.N. Open challenges in magnetic drug targeting. *Wiley Interdisciplinary Reviews: Nanomedicine and Nanobiotechnology*, 2015, vol. 7, issue 3, pp. 446-457. doi: 10.1002/wnan.1311

36. Nacev A., Weinberg I.N., Stepanov P.Y., Kupfer S., Mair L.O., Urdaneta M.G., Shimoji M., Fricke S.T., Shapiro B. Dynamic inversion enables external magnets to concentrate ferromagnetic rods to a central target. *Nano letters*, 2014, vol. 15, issue 1, pp. 359-364. doi: 10.1021/nl503654t

DOI: 10.17277/amt.2018.03.pp.070-082

Assessment and Modeling of Bond Strength of Corroded Reinforcement in Concrete Structures

V.P. Yartsev*, A.N. Nikolyukin, T.M. Pluzhnikova

Tambov State Technical University;
112D, Michurinskaya St., Tambov, 392032, Russia

* Corresponding author. Tel.: +7 4752 63 03 80. *E-mail*: kzis@nnn.tstu.ru

Abstract

One of the most serious causes of the loss of load-bearing capacity of reinforced concrete structures is bond failure between reinforcement and concrete as a result of structural degradation (corrosion) of metal parts. As a consequence, there is a need to study the behavior of corroded reinforcement in reinforced concrete parts.

The purpose of this study is to develop an analytical description of the ultimate bond strength of a reinforcing bar in reinforced concrete structures subject to different levels of corrosion. The modeling technique considered in this research is based on artificial neural networks.

Keywords

Analytical model; bond strength; corrosion; experimental database; reinforcement; concrete; artificial neural networks.

Introduction

One of the most important problems in the modern practice of design and operation of buildings is to predict the life of structures made of modern (new) materials exposed to various external factors. However, some factors can have a negative impact on many materials. Bonds between reinforcement and concrete can be damaged due to the negative impact of external factors. Extensive experimental studies concerning the changes in the bond strength in reinforced concrete under the influence of individual factors have been described in the literature so far. However, a model that takes into account the influence of individual factors or their complex impact on any material has not been developed yet.

Factors influencing the bond strength between reinforcement and concrete include the type of the reinforcing bar, the concentration of corrosive substances, the concrete quality, thickness, etc.

When considering the theory of reinforced concrete structures, it is noteworthy that reinforced concrete ceases to work as a single composite when the maximum stress in the reinforcement is reached. However, the structure during operation is exposed to various impacts that lead to the formation of cracks around the bar, which weakens the bond between the reinforcement and concrete. In addition, the influence of some factors (aggressive media, corrosion of the material, etc.) leads to a decrease in the strength characteristics of the composite materials and the formation of normal cracks in the structure. Under load, an increase in the crack opening width, resulting in additional zones of stress concentration, is observed.

Industrial buildings are most exposed to the negative impact of external factors, as they are influenced by aggressive environments and loads of various kinds, leading to the accumulation of defects in the design. Studies have shown that some effects can have a positive influence on the design. For example, a low level of corrosion of the metal bar leads to a slight increase in the bond strength between the reinforcement and concrete, resulting from the increased pressure on the concrete mass in the stage without cracks. However, once the crack occurs, the bond strength begins to decrease as the corrosion level increases.

In most studies related to durability, the focus is on protecting structural reinforced concrete parts from

the effects of degrading factors, or restoring the structure. Studies on experimental monitoring of the behavior of the reinforcement bond mainly lack analytical modeling. However, in the literature there are some scientific works in which the influence of various factors on the bond strength was estimated and modeled using theoretical or finite elements [1–5]. Having analyzed the available literature, it can be noted that a practical and general model for the estimation of the bond strength has not been developed yet.

In recent years, soft computing technologies have been successful implemented to predict some key properties of concrete and reinforced concrete [6–8].

For example, Mermerdas [9] used programming of gene expression to develop a setting shrinkage model. In Duan's research [10], the applicability of artificial neural networks (**NN**) for predicting the compressive strength of the concrete used was presented. About 150 experimental data obtained from public sources were used to build the NN model. The results of the study of reinforced concrete structures using soft computing have been described in the literature. This method made it possible to study the corrosion density of reinforced concrete slab [13], the bond of concrete floor layers [11] and the load-bearing capacity of the anchor in the concrete block [14]. Regarding the application of soft computing for the calculation of the concrete surface bonding, the information provided in the literature is not sufficient. These studies were mainly focused on the prediction of the bond strength between steel bars and concrete [16, 17]. For example, Dahou [16] used an artificial neural network to model the relations between conventional ribbed steel bars and concrete. The NN models were implemented using a database of 112 results of experimental tests on concrete bond to reinforcement by the method of pullout testing.

Artificial neural networks and fuzzy logic were used by Golafshani [17] to study bond strength between steel bars and concrete. When constructing the NN, the experimental data of 180 different test samples was used. However, according to many authors, no scientific approach to using soft computing to predict the bond strength between corroded steel bars and concrete has been developed yet.

This study presents analytical models created on the basis of artificial neural networks (NN) to predict the tensile strength of concrete bond τ_b. To do this, pullout tests were carried out on the concrete cubes. The data obtained experimentally were used for training and testing of the proposed models. As a result, the statistical efficiency of the NN-based model to predict bond strength between the corroded reinforcement and concrete was evaluated and compared.

Literature Review

It was the German researchers Zaliger R. and Bach G. who estimated the bond strength between concrete and reinforcement for the first time.

Initially, the experiments were aimed at testing the strength of reinforcement anchoring in concrete for the end reinforcements of bends, loops and hooks. However, this method made it possible to investigate anchoring of modern profiles with high-strength concretes [18]. At the same time, bonding was considered as a power characteristic, depending on many factors, the specific value of which was estimated by scientists ambiguously. Nevertheless, in the middle of the twentieth century, Ya.V. Stolyarov believed that bonding directly depends on the bond capacity of the cement gel and the friction that occurs between the materials under the action of radial pressure from concrete shrinkage.

In his studies, Ya.V. Stolyarov identified two groups of factors. The first group refers to a number of factors that affect the slip resistance of reinforcement in concrete [19]. These include the bonding of the projections with concrete, the shrinkage friction and bonding of reinforcement with concrete. The second group quantifies the factors of the first group without affecting the bond. It includes the class and age of concrete.

The stress-strain state in stress redistribution zones is very ambiguous and depends on all factors in the aggregate. However, D.A. Abrams in his work found that the stress-strain state (**SSS**) in the areas of shear stresses of the bond varies significantly under load.

Since the bond is affected by a huge number of factors, it became necessary to apply a phenomenological approach of mathematical analysis of experimental data on the basis of simplifying assumptions.

T. Garay, M.Z.P. Brice and A. Bichara found out that it was quite time-consuming to experimentally determine the value of normal stresses in the reinforcement σ_s in the redistribution area by measuring it in the contact zone [20]. As a result, the application of this characteristic to assess the bond strength τ_b in the contact zone was limited.

On the basis of Abrams's research, in 1913, Ya.V. Stolyarov constructed a curve for the dependence of the bond stress τ_b on "strain slip" for a bar with a variable profile. However, in 1941, S.E. Freifeld spoke about the relation between the bond stress and mutual displacements of the reinforcement relative to the concrete for the first time.

M.M. Kholmansky conducted tests and found the value of the mutual displacement of the reinforcement relative to concrete [21]. The studies were observations of reinforcement displacements relative to concrete during pre-stressing and pulling out the reinforcement from the end-supported prisms.

In order to reduce the calculation complexity and improve the accuracy of the results obtained in the study of bond at certain permissible limits of displacements in the joint, the most commonly used elastic-plastic bond law (Prandtl diagram). The Prandtl diagram is close to the normal bond law, which was experimentally established by M.M. Kholmyansky and his students (Fig. 1) [22]. To simplify the calculations, equation 1 was derived, which determined the average stress values over the entire anchorage zone of the sample.

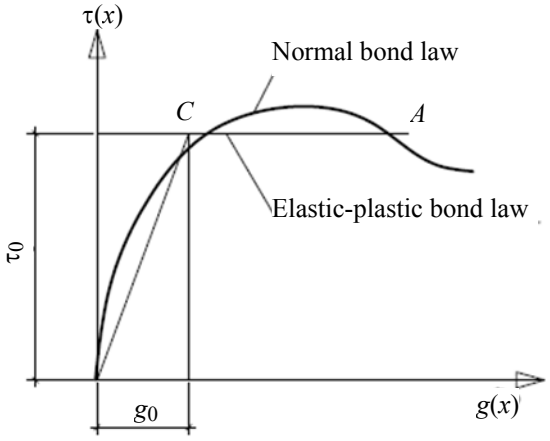

Fig. 1. "τ – *g*" diagram: elastic-plastic and normal laws of bond

$$\tau_b = \frac{N_{max}}{A\,l}, \quad (1)$$

where N_{max} is ultimate load (N) in the pullout test (kN); A is reinforcement perimeter ($A = \pi\, d$, where d is bar diameter (mm)), l is depth of setting (m).

The reason for an increased interest in the issue of bond in the USSR in 1950–1960 was the active introduction of pre-stressed reinforced structures. As a result, fundamental experimental and theoretical studies on the problem of bond were conducted under the guidance of M.M. Kholmyansky [23–31] and A.A. Oatul [32–40].

However, M.M. Kholmyansky and H. Trost had significant disagreements in the interpretation of the law of bond between reinforcement and concrete.

It was found that the interaction of the bar strands concrete under the load of the reinforcement is characterized by screw motion in the concrete. In the preliminary reduction stage, considerable displacements up to 1 mm were observed. In this case, the displacement g is a conditional characteristic with respect to the bond under the load of profiled reinforcing bars.

Longitudinal forces, arising in the strands, press its protrusions to the "concrete nut" (Fig. 2). In this case, there is a correlation between friction from the transverse pressure of the bar on concrete in the contact zone and the periodic profile of the reinforcement.

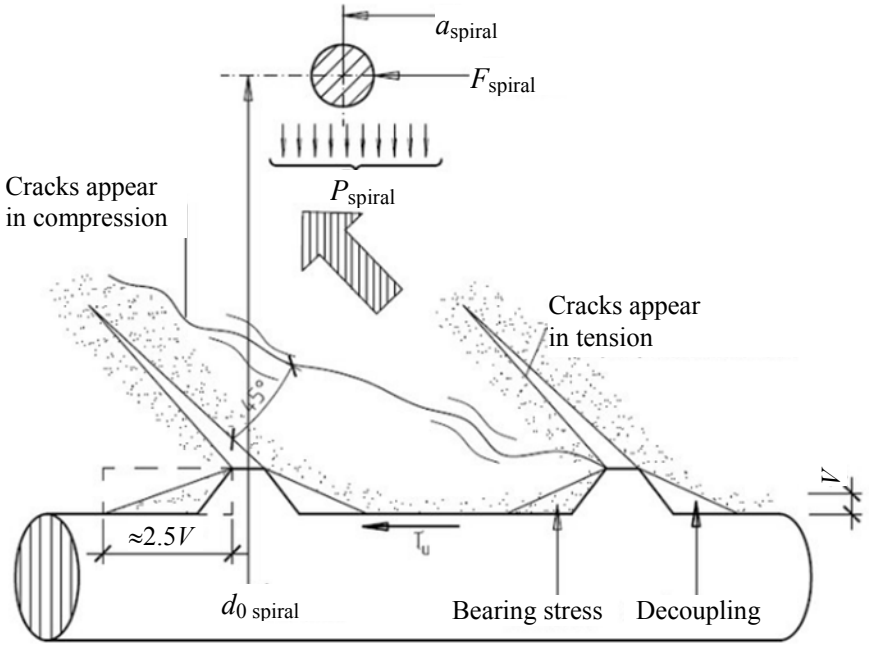

Fig. 2. Destruction of concrete console

The phenomenological method in determining τ_b has a number of shortcomings:

– constrained deformations are not taken into account;

– it is impossible to determine the SSS at contact zones in the development of cracking and plastic deformations;

– deformation of the concrete shell along the entire length of the anchoring is possible.

The above-mentioned shortcomings were eliminated with the development of computational models, the principle of which was based on the theory of creep and elasticity theory.

The application of numerical calculation methods and a computer in conjunction with the bond simulation allowed obtaining reliable and detailed results without carrying out laborious experiments.

To study reinforcement bond with concrete in a beam under pure bending conditions, A.S. Scordelis and D. Ngo used the finite element method for the first time. It was found that the interaction of reinforcement with concrete depends on the contact of the final element, which determines the physical and mechanical properties. In addition, there was a correlation between the development of cracks, both normal and inclined to the longitudinal axis of the beam, and the value of the external load. This method has been widely used both abroad and in the USSR.

Another method based on finding the SSS of concrete in the area adjacent to the periodic profile reinforcement was proposed by N.S. Karpenko and G.N. Sudakov. For calculation, a concrete area of cylindrical shape was used in the contact zone with the reinforcement. The interaction of the computational domain with external factors was elastic bonds. To determine the nature of the combined action of the reinforcement and concrete, conditions were set on the inner surface of the design cylinder. When solving this problem, it was expedient to use a variational-difference method, which allowed predicting the development of cracks and determining the concrete SSS during cracking.

Since the unified theory of bonding did not exist for a long time, P.P. Nazarenko proposed a "generalized law of friction of steel reinforcement with concrete".

Currently, the problem associated with the bond between the reinforcement and concrete, is quite relevant. This topic is of fundamental importance for the design of reinforced concrete structures and the improvement of calculation techniques. One possible way to solve this problem is to use soft computing.

Effect of concrete strength on bond

As it was noted by M.M. Kholmyansky, the value of the bearing stress when pulling out the anchors reached 5–20 times of the cubic strength. In turn, N.M. Mulin determined the value of the ultimate stress under the reinforcement projections, which amounted to 15–20 R_b. However, the role of strength in the reinforcement bond has not been studied completely [12].

Based on the conducted experiments on pulling seven-wire strands from prisms, A.I. Semenov noted a significant increase in the maximum pulling load P_{max} in the process of increasing the strength from 12.5 to 25 MPa. However, if the strength increased from 25 to 45 MPa, then the increase in P_{max} was observed only for samples whose length of stress transfer section is $l_p = 20d$, where d is the nominal diameter of the bar, and if $l_p = (40–60)d$, the bar breaks. In addition, Yu.M. Redko and E.F. Panyukov determined that the anchoring conditions did not depend on the change in the concrete strength from 25 to 70 MPa during the pre-stressing of the cable rope.

In their studies, Al Khalili, E.W. Bennet, J.A. Uijl established a directly proportional dependence of the bond strength on the concrete strength.

N. Trost determined the dependence of the reinforcement strength of the periodic profile on the concrete strength. The bar bond is proportional to the square root of the concrete strength.

The concrete strength affects the length of the stress transfer section and the mechanism of bonding in general, if its value does not exceed 30 MPa. If the concrete strength is more than 30 MPa, it does not affect the bond. In this case, the bond depends on the rigidity of the concrete cage and the intensity of the indirect reinforcement.

Experimental data

To carry out theoretical studies, experimental results were used when testing 250 samples. The examples are presented in Table 1. The ultimate bond strength between reinforcement and concrete was calculated by equation (1).

Many researchers believed that the stress distribution in the early stages of pulling out is uneven, but it becomes almost homogeneous in the limiting state. Therefore, the expression of the limiting adhesion force in equation 1 can be considered as the average bonding stress between concrete and reinforcement. This method of calculating the value τ_b (equation (1)) provides a practical approach for determining the bond strength between concrete and reinforcement, but it

Table 1

Examples of experimental data used to construct a model

No.	Cube compressive strength of concrete R_b, MPa	Surface dimensions of a concrete sample, mm	Rebar profile	Diameter of the bar, mm	Depth of bar anchoring, mm	Corrosion level, %	Maximum tangential stress, MPa
1	23	45	2	14	50	3.81	1.3
2	51	15	2	14	50	0	19.6
3	51	15	2	14	50	0	14.3
4	51	15	2	14	50	0	20
5	51	30	2	14	50	0	20.9
6	51	30	2	14	50	0	21.7
7	51	30	2	14	50	0	21
8	51	45	2	14	50	0	21.2
9	51	45	2	14	50	0	27.4
10	51	45	2	14	50	0	27.8
11	51	15	2	14	50	1.33	18.5
12	51	15	2	14	50	7.48	3.5
13	51	15	2	14	50	4.47	6.3
14	51	15	2	14	50	0.77	22.3
15	51	15	2	14	50	0.8	22.4
16	51	15	2	14	50	0.9	21.7
17	51	15	2	14	50	0.94	21.5
18	22.13	44	1	12	80	0.27	2.65
19	22.13	44	1	12	80	0.29	3.23
20	22.13	44	1	12	80	0.92	5.79
21	22.13	44	1	12	80	1.13	5.84
22	22.13	44	1	12	80	0.78	7.41
23	22.13	44	1	12	80	1.47	8.63
24	22.13	44	1	12	80	1.85	7.3
25	22.13	44	1	12	80	1.5	7.96
26	22.13	44	1	12	80	1.99	9.29
27	22.13	44	1	12	80	1.04	10.26
28	22.13	44	1	12	80	2.75	5.97
231	29	145	2	25	160	1.31	10.59
232	29	145	2	25	160	2.22	5.61
233	29	145	2	25	160	3.16	12.72
234	29	145	2	25	160	0.79	9.06
235	23	15	2	14	50	4.32	12
236	23	15	2	14	50	4.33	12
237	28	79.4	2	19	177.8	0	6.32
238	28	79.4	2	19	178.8	0	5.79
239	28	79.4	2	19	179.8	0.72	7.67
240	28	79.4	2	19	180.8	0.72	7.13
241	28	79.4	2	19	181.8	0.98	8.41
242	28	79.4	2	19	182.8	1.23	4.91
243	28	79.4	2	19	183.8	1.44	3.1
244	28	79.4	2	19	184.8	1.7	3.79
245	28	79.4	2	19	185.8	2.21	3.7
246	28	79.4	2	19	186.8	2.88	2.09
247	28	79.4	2	19	187.8	5.19	1.41
248	27.2	40	2	22.3	500	0	6.96
249	28.4	40	2	22.3	500	2.5	2.89
250	24.4	40	2	22.3	500	11.9	2.27
251	27.7	40	2	22.3	500	28.9	2.38

does not reflect the actual state of the structure, since it does not take into account factors such as the formation of stress cracks, local collapse, support reactions, etc.

Six critical parameters were used in the model. The input variables were compression strength, concrete sample size, reinforcing bar profile, reinforcement diameter, embedment depth, corrosion level, maximum bond strength.

These prognostic parameters were used to develop the model as an estimate of the ultimate bond strength between corroded reinforcement and concrete. The ranges of each variable are presented in [41–49]. For example, the steel bar diameter, the embedment depth, the dimensions of the upper face of the concrete cube, and the level of corrosion were in the range 12–25 mm, 80–500 mm, 40–147.5 mm and 0–80 %, respectively. The tests used A240-A400 valves. The size of the samples was 150×150×150 mm. After the effect of various factors on the specimens, the bond strength between the core and concrete was determined by testing the pulling cubes (Fig.3).

In all the studies used in the preparation of the database, corrosion induction was achieved with the help of similar electrochemical systems. A schematic depiction of a typical accelerated corrosion plant is shown in Fig. 4. To induce different levels of corrosion on the reinforcement, potentiometers were used to control the intensity of the current. The current in this case served as a catalyst, namely, it accelerated the corrosion process of the reinforcing bar. All systems had cathode (counterelectrode) and anode (reinforcing) connections for the corrosion process. All samples were immersed in NaCl solution. To avoid corrosion of the open bar during the test, a coating was used for the reinforcing bar and the upper surface of the concrete.

Electrochemical systems sometimes consist of different components. In this case, the degree of corrosion is measured as the weight loss of reinforcing bar weights. In all studies, the calculated (theoretical) weight loss of the reinforcing bars due to corrosion was evaluated using the Faraday law. Then the actual (experimental) level of corrosion or the percentage loss of sample weight was calculated.

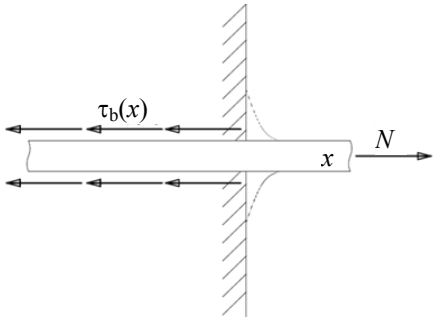

Fig. 3. Pullout testing of samples

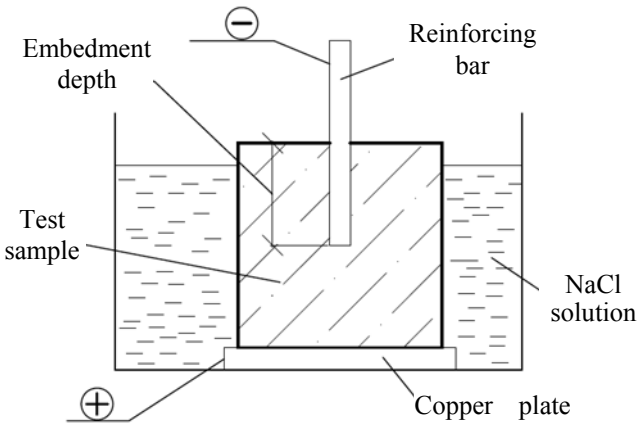

Fig. 4. Schematic representation of the electrochemical system used to induce corrosion of the reinforcing bar

To model the properties of bonding, the database was arbitrarily divided into three parts: training, monitoring and testing. At the same time, 5 % of the experimental data were used for testing, another 5 % for monitoring, and the remaining 90 % for network training. As a result of monitoring, the risk of re-training of the network was reduced. The training database was used to develop a predicting model, while a testing database was used to monitor the repeatability and reliability of the proposed NN models.

Overview of soft computing methods

Soft computing is a set of methods that uses tolerances for inaccuracy and uncertainty, and to achieve acceptability, reliability, and low cost in solutions. Fuzzy logic, neurocomputing and probabilistic reasoning are the main components of soft computing. The field of application of soft computing is quite extensive. These technologies are used to solve engineering problems, to perform financial assessments, to conduct medical diagnostics, etc. Methods of soft computing derived from the philosophy of artificial intelligence imitate the human mind.

The most popular methods of soft computing are artificial neural networks.

Neural networks (NN)

The neural network (NN) is a functional modeling of biological sensory structures of the central nervous system. It can demonstrate a number of characteristics of the human brain, such as the accumulation of experience and the solution of new problems based on the knowledge gained. In neural networks (NNs), there are many cells and connections between inputs and outputs. These connections between the neurons get the

value of the transfer, which is called the weight. Weights can be updated for each new fragment of information. After implementing the scales, the existing training system is easily updated with data that will be received later. NNs are systems consisting of a set of simple processing elements operating in parallel, whose functions are determined mainly by the connection scheme.

These systems are capable of performing high-level functions, such as adaptation or training, as well as lower-level functions, such as pre-processing data for various kinds of inputs. For the development of NNs, mathematical theories of teaching, information processing and control, as well as knowledge of the functioning of the biological nervous system, were used.

At the same time, the *nnstart* tool was used to simulate the neural network, which was also used for soft calculations in MatlabV.R2014a.

If a problem arises, the neural network is used to compare the data of the numeric inputs with the set of numeric data of the outputs. Nftool is used to create and train a network, and evaluate its performance using a root-mean-square error and regression analysis. A two-layer network with direct connection, sigmoid hidden objects and linear solutions that can be satisfied arbitrarily with multidimensional mapping problems, taking into account consistent data and a sufficient number of neurons in its hidden layer. The network was prepared using the Levenberg-Marquardt feedback algorithm. An artificial neuron consists of three main components: weight, displacement and activation function. Each neuron receives inputs I_1, I_2, ..., I_n, attached by weight w_i that indicate the connection power for this input. Each input is then multiplied by the corresponding weight of the neural connection. Evasion can be defined as the type of connection weight with a constant non-zero value added to the summation of weighted inputs (2). A generalized operation of an algebraic matrix is represented in Eq. (3). It is necessary to clearly express mathematical operations in an artificial neuron.

$$U_k = \sum_{j=1}^{n} w_k I_j + \text{Bias}_k ; \tag{2}$$

$$U_k = \begin{bmatrix} w_{11} & w_{12} & \cdots & w_{1n} \\ w_{21} & w_{22} & \cdots & w_{2n} \\ \cdot & \cdot & \cdots & \cdot \\ \cdot & \cdot & \cdots & \cdot \\ \cdot & \cdot & \cdots & \cdot \\ w_{m1} & w_{m2} & \cdots & w_{mn} \end{bmatrix}_{m\times n} \begin{bmatrix} I_1 \\ I_2 \\ \cdot \\ \cdot \\ \cdot \\ I_n \end{bmatrix}_{n\times 1} +$$

$$+ \begin{bmatrix} \text{Bias}_1 \\ \text{Bias}_2 \\ \cdot \\ \cdot \\ \cdot \\ \cdot \\ \text{Bias}_m \end{bmatrix}_{m\times 1} = \begin{bmatrix} U_1 \\ U_2 \\ \cdot \\ \cdot \\ \cdot \\ \cdot \\ U_m \end{bmatrix}_{m\times 1} . \tag{3}$$

Since the *nftool* uses normalized values in the range [–1, 1], the input parameters are determined using Equation 3. In addition, the results obtained are also in the normalized form. Equation 4 and the normalization coefficients a and b for the outputs are used in the de-normalization process and to obtain the control.

$$\beta_{\text{norm}} = a\beta + b, \tag{4}$$

where β is actual input parameter or output values, β_{norm} is the normalized value of the input parameters or outputs in the range from [–1, 1]; a and b are the normalization coefficients given in the following equations (5) and (6). As a result of the normalization process, the smallest numerical value in the array becomes –1, while the highest value becomes equal to 1.

$$a = \frac{2}{\beta_{\max} - \beta_{\min}}; \tag{5}$$

$$b = \frac{\beta_{\max} + \beta_{\min}}{\beta_{\max} - \beta_{\min}}, \tag{6}$$

where $\beta_{\max}$, $\beta_{\min}$ are maximum and minimum actual values of inputs or outputs, respectively.

The coefficients of normalization of both input and output variables are presented in Table 2.

In the NN architecture, at the input level, there are six nodes corresponding to the six prediction factors, eight nodes in the hidden layer and one in the output layer corresponding to the ultimate bond strength τ_b between reinforcement and concrete. Therefore, to build a NN-based model, the architecture of 6-8-1 NN was obtained (Fig. 5). The NN model used in this study can be simply expressed by Eq. (7). The details of the input and the layers, the activation function (hyperbolic tangent), and the bias are given in equations (7)–(10). It should be emphasized that all numerical variables must be normalized to the range [–1, 1] before entering NN. Therefore, it is necessary to enter the normalized values in the mathematical operations specified for the

Table 2

Normalization coefficients for the database

Normalization parameters	Input and output variables						
	I_1, MPa	I_2, mm	I_3	I_4, mm	I_4, mm	I_5,%	I_6, MPa
β_{max}	52.1	147.5	2	25	500	80	31.7
β_{min}	22.13	15	1	12	35.9	0	1.3
a	0.066733	0.015094	2	0.153846	0.004309	0.025	0.065789
b	– 2.47681	– 1.22642	– 3	– 2.84615	– 1.15471	– 1	– 1.08553

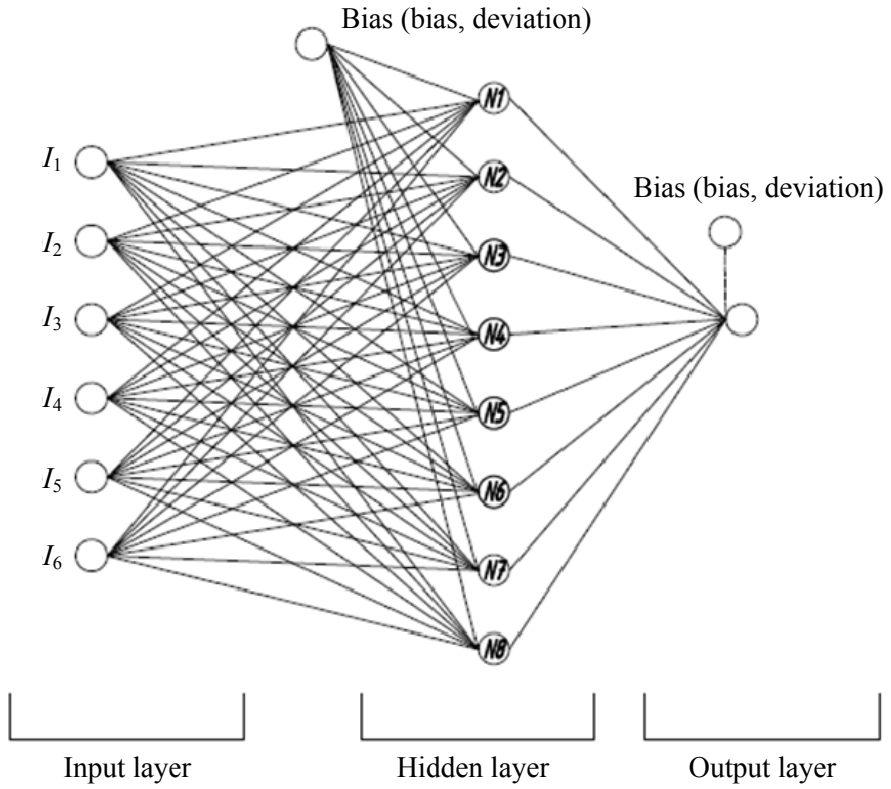

Fig. 5. The NN architecture for the proposed model

NN model. It should also be taken into account that the final result obtained from equation (10) is in the normalized form, which must be de-normalized according to equation (4) and the values of the normalization factors given in Table 2.

$$\tau_b = \text{Bias}_{\text{output layer}} + \sum_{j=1}^{n} w_k F(U_k), \quad (7)$$

where $\text{Bias}_{\text{output layer}}$ = –0.72598625301132214 and $f(x)$ (Hyperbolic tangent) is an activation function.

$$\tau_b = -0.72598625301132214 - 0.73052205364589862 \tan h(U_1) + 0.43372098218006 \tan h(U_2) -$$
$$- 0.378948852713141 \tan h(U_3) + 0.546753081298744 \tan h(U_4) + 0.743044141180237 \tan h(U_5) -$$
$$- 0.287177258041315 \tan h(U_6) + 0.506892739633613 \tan h(U_7) + 0.511933571886970 \tan h(U_8), \quad (8)$$

where τ_b is ultimate bond strength between reinforcement and concrete, MPa, $\tan h(x)$ is the activation function (hyperbolic tangent) found by the following equation (9), and U_1, U_2, ..., U_8 can be calculated from formula (10).

$$\text{tg } h = \frac{2}{1 - e^{-2x}} - 1; \quad (9)$$

$$\begin{bmatrix} -1.867124673755 & -1.970456141181 & -4.648227350451 & 5.676001648574 & 1.327520472019 & -1.755465506282 \\ 0.2503064224871 & -1.260742854080 & 0.8921461740089 & 8.357372886823 & 4.390412668468 & 9.4675705191697 \\ -9.368186441120 & -5.493604583006 & 6.9059256572452 & 3.107102687849 & -5.58700784565 & 23.154702386087 \\ -3.726007098251 & -0.756975200048 & -12.82896288242 & 2.770087904822 & -5.89548833694 & -26.32416136369 \\ 1.7968070762203 & -2.049238735028 & -0.305519465914 & -1.49625722378 & 1.135559385340 & -2.283551791593 \\ 7.1715088540923 & -2.34698114822 & 5.02649043026052 & 0.344211422189 & -5.77532613965 & 4.173420772519 \\ -0.32006490132 & 0.697003679279 & 5.29615191586122 & 4.261154643924 & -5.84236595555 & 17.71885018913 \\ 24.1402334064 & -4.97536745629 & -2.64334234274495 & 4.684149012532 & -0.257163855197 & -25.5886645048 \end{bmatrix}_{m\times n} \times$$

$$\times \begin{bmatrix} I_1 \\ I_2 \\ I_3 \\ I_4 \\ I_5 \\ I_6 \end{bmatrix}_{n\times 1} + \begin{bmatrix} 4.06873241040918 \\ 0.311490468158442 \\ 17.9741558487695 \\ -12.5797898530226 \\ 3.10449572735974 \\ 0.470455925563070 \\ 5.74408786804873 \\ 1.54391398316535 \end{bmatrix}_{m\times 1} = \begin{bmatrix} U_1 \\ U_2 \\ U_3 \\ U_4 \\ U_5 \\ U_6 \\ U_7 \\ U_8 \end{bmatrix}_{m\times 1}. \quad (10)$$

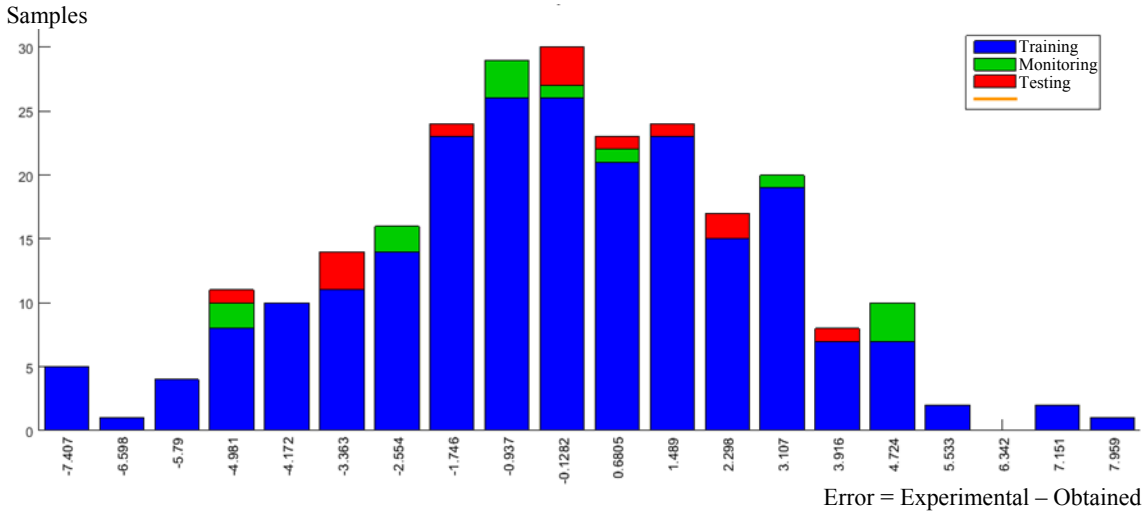

Fig. 6. Error histogram

A comparison of the prediction results obtained with the NN model and the experimental data obtained as a result of the conducted adhesion tests is shown in Fig. 6. To achieve these indicators, it took 83 stages. From Fig. 7 it is obvious that the nature of the learning occurred spasmodically with the gradual accumulation of "knowledge", decreasing the error. Correlation coefficients 0.973 and 0.916 were achieved for the control and test database, respectively. Based on the work done, it can be concluded that the NN model is reliable (Fig. 8).

Conclusion

In this paper we presented a study of the ultimate bond strength τ_b of reinforced concrete elements exposed to various factors. The proposed formulations are based on the most reliable method of soft computing – an artificial neural network (NN). To construct the analytical model, the available experimental data collected by various authors were used. Based on the analysis of the results presented in this study, we can draw the following conclusions.

It is shown that soft computing techniques can be tools to bring empirical evidence ultimate bond strength τ_b of samples subject to different levels of corrosion. All predicted values were reliable and comparable to those observed. Therefore, the proposed network can be viewed as a useful model with a satisfactory ability to predict.

It is noted that for low levels of experimental values τ_b up to 4.5 MPa the mean error between the predicted and actual values was the highest for the model compared to other intervals τ_b.

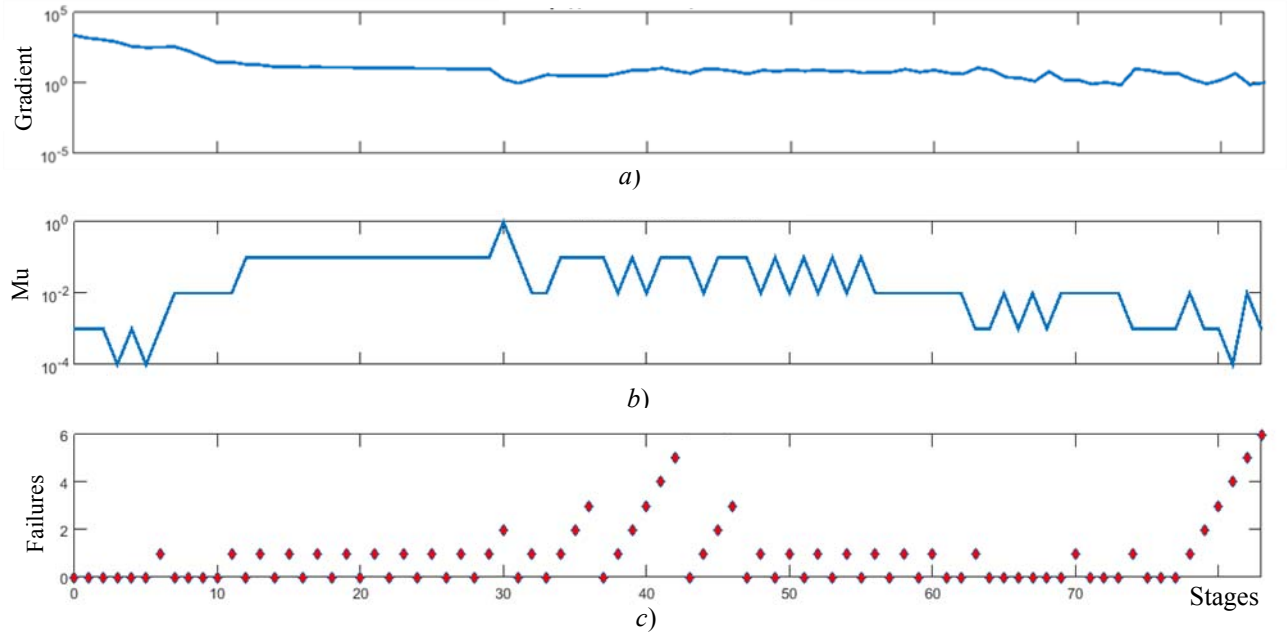

Fig. 7. State of the artificial neural network in the training process for 83 stages:
a – Gradient = 1.0385; *b* – Mu = 0.001; *c* – Maximum number of verification *s* = 6

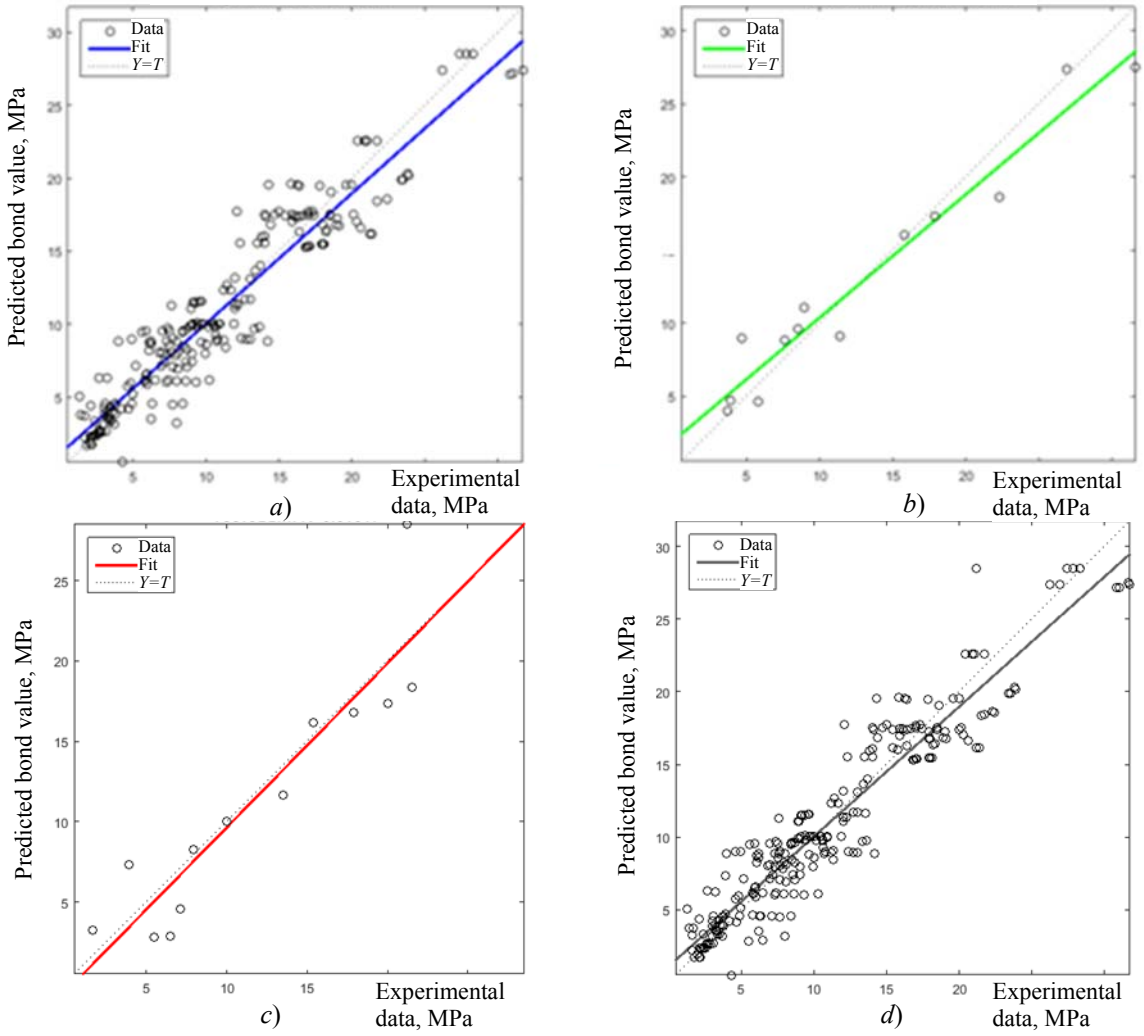

Fig. 8. Model regression analysis:
a – Training: *R* = 0.94478, Regression equation – *x* = 0.89*y* + 1.1; *b* – Monitoring: *R* = 0.97385, Regression equation – *x* = 0.84*y* + 2.0; *c* – Testing: *R* = 0.91617, Regression equation – *x* = 1.0*y* – 0.56; *d* – Model: *R* = 0.94721 Regression equation – *x* = 0.89*y* + 1.1

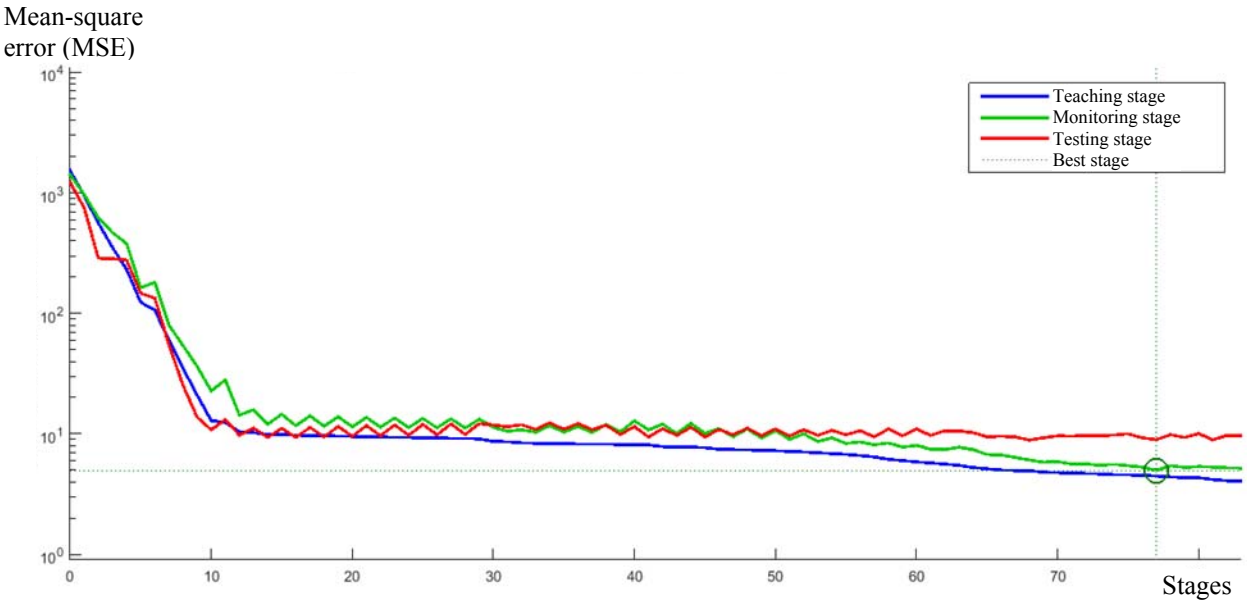

Fig. 9. Results of network training
(The best verification value of 4.9794 occurred at the 77th stage)

One of the reasons for the deviations may be the inconsistency of the authors in the methodology in testing and making the samples, which were noticeable at high corrosion levels and low strength values of the concrete. According to the observed correlations, the reliability of the proposed model can be considered satisfactory for actual values τ_b exceeding 4.5 MPa.

The correlation coefficient for the training database was 0.947. In addition, to test the databases, correlation coefficients of 0.947 for the first, 0.973 and 0.916 for the latter were achieved (Fig. 8). Despite the fact that the database for testing was not used for training, a high level of prediction was obtained, related to a low mean absolute error percentage and high correlation coefficients. This indicates that the developed model is reliable.

Statistical analysis based on MSE values also showed that the proposed formulations of NN had relatively lower errors (Fig. 9). Observing the general trend in the evaluation of efficiency, it was found that the NN model can be considered as a more preferred prediction model from the existing at the moment.

Since the NN is not capable of making calculations without computer technology, its application for a manual calculation is considered laborious. However, the use of the NN model becomes indispensable when it becomes necessary to predict higher accuracy. At the same time, the use of a computer effectively eliminates the difficulties that arise in computing. The solution is to computerize the NN model with a simple spreadsheet. Thus, this will overcome this insignificant drawback.

References

1. Amleh L., Ghosh A. Modeling the effect of corrosion on bond strength at the steel–concrete interface with finiteelement analysis. *Can J Civ Eng,* 2006, vol. 33, pp. 673-682.

2. Berto L., Simioni P., Saetta A. Numerical modeling of bond behaviour in RC structures affected by reinforcement corrosion. *Eng Struct,* 2008, vol. 30, pp. 1375-1385.

3. Migunov V.N. Ovchinnikov I.I., Ovchinnikov I.G. *Eksperimental'no-teoreticheskoe modelirovanie armiro-vannykh konstruktsij v usloviyakh korrozii* [Experimental theoretical modeling of reinforced structures under corrosion conditions]. Penza, PGUAS, 2014. 362 p. (Rus.)

4. Alekseev S.N., Ivanov F.M., Modry S., Shissl' P. *Dolgovechnost' zhelezobetona v agressivnykh sredakh* [Durability of reinforced concrete in corrosive environments]. Moscow: Strojizdat, 1990, 320 p. (Rus.)

5. Veselov A.A. Raschet dliny zadelki armatury periodicheskogo profilya v betone [Calculation of the reinforcing length of the periodic profile in concrete]. In *Statika i dinamika slozhnykh stroitel'nykh konstruktsij: mezhvuz. sb. tr.* [Statics and dynamics of complex building structures: interuniversity. Col.of pap.], Leningrad: LISI, 1980, pp. 148-155. (Rus)

6. Topcu I.B., Boga A.R., Hocaoglu F.O. Modeling corrosion currents of reinforced concrete using ANN. *Automat Constr.*, 2009, vol. 18(2), pp.145-152.

7. Lim C.H., Yoon Y.S., Kim J.H. Genetic algorithm in mix proportioning of high performance concrete. *Cem Concr Res,* 2004, vol. 34(3), pp. 409-420.

8. Fairbairn E.M.R., Silvoso M.M., Filho R.D.T., Alves J.L.D. Ebecken NFF Optimization of mass concrete construction using genetic algorithms. *Comput Struct*, 2004, vol. 82(2-3), pp. 281-299.

9. Adhikary B.B., Mutsuyoshi H. Prediction of shear strength of steel fiber RC beams using neural networks. *Constr Build Mater,* 2006, vol. 20(9), pp. 801-811.

10. Duan Z.H., Kou S.C., Poon C.S. Prediction of compressive strength of recycled aggregate concrete using artificial neural networks. *Constr Build Mater*, 2013, vol. 40, pp. 1200-1206.

11. Ashour A.F., Alvarez L.F., Toropov V.V. Empirical modeling of shear strength RC deep beams by genetic programming. *Comput Struct*, 2003, vol. 81(5), pp. 331-338.

12. Goh A.T.C. Prediction of ultimate shear strength of deep beams using neural networks. *ACI Struct J,* 1995, vol. 92(1), pp. 28-32.

13. Sadowski L. Non-destructive investigation of corrosion current density in steel reinforced concrete by artificial neural networks. *Arch Civ Mech Eng,* 2013, vol. 13(1), pp. 104-111.

14. Sadowski L. Non-destructive evaluation of the pulloff adhesion of concrete floor layers using rbf neural network. *J Civ Eng Manag,* 2010, vol. 19(4), pp. 550-560.

15. Sakla S.S.S., Ashour A.F. Prediction of tensile capacity of single adhesive anchors using neural networks. *Comput Struct,* 2005, vol. 83, pp. 1792-1803.

16. Dahou Z., Sbartai Z.M., Castel A., Ghomari F. Artificial neural network model for steel-concrete bond prediction. *Eng Struct,* 2009, vol. 31(8), pp. 1724-1733.

17. Golafshani E.M., Rahai A., Sebt M.S., Akbarpour H. Prediction of bond strength of spliced steel bars in concrete using artificial neural network and fuzzy logic. *Constr Build Mater,* 2012, vol. 36, pp. 411-418.

18. Stolyarov Ya.V. Vvedenie v teoriyu zhelezobetona [Introduction to the theory of reinforced concrete], Moscow-Leningrad: Strojizdat, 1941, 447 p. (Rus.)

19. Bajkov V.N., Sigalov E.E. Betonnye i zhelezobetonnye konstruktsii: Obshhij kurs [Concrete and reinforced concrete structures: Basic course], Moscow: Strojizdat, 1991, 768 p. (Rus.)

20. Garai T. Issledovanie ankerovki armatury v betone [Investigation of anchoring of reinforcement in concrete]. In *Issledovanie prochnosti ehlementov zhelezobetonnykh konstruktsij* [*Investigation of the strength of reinforced concrete structures*]. Sb.tr. NIIZHB, Moscow: Gosstrojizdat, 1959, issue 5, pp. 78-109. (Rus)

21. Kholmyanskij M.M. *Kontakt armatury s betonom* [Contact of reinforcement with concrete], Moscow: Strojizdat, 1981, 184 p. (Rus.)

22. Kholmyanskij M.M. *Raschet tsentral'no armirovannykh prizmaticheskikh ehle-mentov na stseplenie* [Calculation of centrally reinforced prismatic elements for bond strength]. In Sb.tr. NIIZHB, Moscow: Gosstrojizdat, 1961, issue 4, pp. 122-153. (Rus.)

23. Kholmyanskij M.M., et al. Stseplenie sterzhnevoj armatury periodicheskogo profilya s betonom [Bonding of bar reinforcement with a periodic profile of concrete]. In *Stseplenie armatury s betonom* [Coupling of reinforcement with concrete], Moscow, 1971, pp. 31-37. (Rus.)

24. Kholmyanskij M.M. Zadelka armatury v betone [Fixing reinforcement in concrete]. *Beton i zhelezobeton* [Concrete and Reinforced Concrete], 1965, vol. 11, pp. 21-25. (Rus.)

25. Kol'ner V.M., Aliev SH.A., Gol'dfajn B.S. Stseplenie s betonom i prochnost' zadelki sterzhnevoj armatury periodicheskogo profilya [Concretion with concrete and strength of the insertion of reinforcing bar of the periodic profile]. *Beton i zhelezobeton* [Concrete and Reinforced Concrete], 1965, vol. 11, pp. 25-27. (Rus.)

26. Kholmyanskij M.M. Tekhnicheskaya teoriya stsepleniya armatury s betonom i ee primenenie [The technical theory of reinforcement coupling with concrete and its application]. *Beton i zhelezobeton* [Concrete and Reinforced Concrete], 1968, vol. 12, pp. 10-18. (Rus.)

27. Kholmyanskij M.M. Metodika ehksperimental'noj issledovaniya stsepleniya armatury s betonom [Methods of experimental study of reinforcement coupling to concrete]. *Metodika laboratornykh issledovanij deformatsij i prochnosti betona, armatury i zhelezobetonnykh konstruktsij* [Methods of laboratory studies of deformation and strength of the concrete, rebar and concrete constructions], Moscow, 1962, pp. 138-147. (Rus.)

28. Tevelev Yu.A. Zadelka armatury v betone pri peremennom stseplenii po dline zony ankerovki [Fixation of reinforcement in concrete with variable bond along the length of the anchoring zone]. *Stseplenie armatury s betonom* [Coupling of reinforcement with concrete], Moscow, 1971, pp. 14-21. (Rus.)

29. Kholmyanskij M.M. Nadarejshvili G.F., Zajtsev V.V. O primenenii zakona stsepleniya pri issledovanii mekhanicheskogo vzaimodejstviya armatury periodicheskogo profilya i betona [On the application of the law of cohesion in the study of the mechanical interaction of reinforcement of a periodic profile and concrete]. *Stseplenie armatury s betonom* [Coupling of reinforcement with concrete], Chelyabinsk, 1968, pp. 27-29. (Rus.)

30. Kholmyanskij M.M., Kol'ner V.M., Gol'dfajn B.S. Stseplenie s betonom sterzhnevoj armatury periodicheskogo profilya [Coupling of concrete with bar reinforcement of the periodic profile]. *Stseplenie armatury s betonom* [Coupling of reinforcement with concrete], Chelyabinsk, 1968, pp. 46-47. (Rus.)

31. Tevelev Yu.A. K voprosu rascheta na stseplenie pri peremennom zakone stsepleniya po dline zadelki [To the problem of bond calculating under the variable law of evaluation of the length of the seal]. *Stseplenie armatury s betonom* [Coupling of reinforcement with concrete], Chelyabinsk, 1968, pp. 34-35. (Rus.)

32. Oatul A.A. Osnovy teorii stsepleniya armatury s betonom [Basics of the theory of coupling of reinforcement with concrete], *Issledovaniya po betonu i zhelezobetonu. Sb.tr. CHPI* [Studies on concrete and reinforced concrete. ChPI Col. of papers], Chelyabinsk, 1967, issue 46, pp. 6-26. (Rus.)

33. Oatul A.A. Predlozheniya k postroeniyu teorii stsepleniya armatury s betonom [Proposals on the construction of the theory of the coupling of reinforcement with concrete], *Beton i zhelezobeton* [Concrete and Reinforced Concrete], 1968, vol. 12, pp. 8-10. (Rus.)

34. Tsekhmistrov V.M. Raschet napryazhenij i deformatsij pri vydergivanii armatury iz betonnoj prizmy, opertoj tortsom (obrazets na vydergivanie) [Calculation of stresses and deformations when pulling reinfrocement from a concrete prism supported by an end face (pullout test)], *Issledovanie po betonu i zhelezobetonu. Sb. tr. CHPI* [Studies on concrete and reinforced concrete. ChPI Col. of papers], Chelyabinsk, 1967, issue 46, pp. 27-43. (Rus.)

35. Oatul A.A., Ivashenko Yu.A. Ehksperimental'noe issledovanie stsepleniya armatury s betonom na rastyanutykh obraztsakh pri kratkovremennom, povtornom i dlitel'nom dejstvii nagruzki [Experimental study of reinforcement of bond to concrete on stretched samples under short-term, repeated and long-term load action], *Issledovaniya po betonu i zhelezobetonu. Sb. tr. CHPI* [Studies on concrete and reinforced concrete. ChPI Col. of papers], Chelyabinsk, 1967, issue 46, pp. 44-71. (Rus.)

36. Pasepshik V.V. Issledovanie vnutrennego treshhinoobrazovaniya v tsentral'no armirovannom korotkom rastyanutom obraztse [Investigation of internal cracking in a centrally reinforced short stretched sample], *Issledovaniya po betonu i zhelezobetonu. Sb. tr. CHPI* [Studies on concrete and reinforced concrete. ChPI Col. of papers], Chelyabinsk, 1967, issue 46, pp. 72-84. (Rus.)

37. Oatul A.A., Kutin Yu.F. Ehksperimental'noe opredelenie differentsirovannogo zakona stsepleniya sterzhnevoj armatury s betonom [Experimental definition of the differentiated law of coupling of core reinforcement with concrete], *Issledovaniya po betonu i zhelezobetonu. Sb. tr. CHPI* [Studies on concrete and reinforced concrete. ChPI Col. of papers], Chelyabinsk, 1967, issue 46, pp. 72-84. (Rus.)

38. Pasepshik V.V. Primenenie metoda konechnykh ehlementov v teorii stsepleniya armatury s betonom [The application of the finite element method in the theory of reinforcement coupling with concrete], *Issledovaniya po betonu i zhelezobetonu. Sb. tr. CHPI* [Studies on concrete and reinforced concrete. ChPI Col. of papers], Chelyabinsk, 1974, issue 149, pp. 127-132. (Rus.)

39. Tsekhmistrov V.M. Eksperimental'nye issledovaniya zakonov stsepleniya s betonom sterzhnej [Experimental studies of the bond laws of concrete with bars], *Issledovaniya po betonu i zhelezobetonu. Sb. tr. CHPI* [Studies on concrete and reinforced concrete. ChPI Col. of papers], Chelyabinsk, 1974, issue 149, pp. 142-148. (Rus.)

40. Oatul A.A., Pyl'neva T.M. Predlozheniya po postroeniyu teorii polzuchesti stsepleniya armatury s betonom [Proposals on the construction of the theory of creep-coupling of reinforcement with concrete], *Zhelezo-betonnye konstruktsii* [Reinforced concrete structures], Chelyabinsk, 1969. pp. 49-61. (Rus.)

41. Almussallam A.A., Al-Gahtani A.S., Aziz A.A., Rasheeduzzafar Effect of reinforcement corrosion on bond strength. *Constr Build Mater*, 1996, vol. 10(2), pp. 123-129.

42. Auyeung Y., Balaguru P., Chung L. Bond behavior of corroded reinforcement bars. *ACI Mater J.* 2000, vol. 97(2), pp. 214-220.

43. Shima H. (2002) Local bond stress-slip relationship of corroded steel bars embedded in concrete. In: *Proceeding of the third international symposium on bond in concrete,* Budapest, Nov 2002 Materials and Structures, pp. 153-158.

44. Zhao Y., Jin W. Test study on bond behavior of corroded steel bars and concrete. *J Zhejiang Univ* (*Engineering Science Edition*), 2002, vol. 36(4), pp. 352-356 (in Chinese)

45. Fang C., Lundgren K., Chen L., Zhu C. Corrosion influence on bond in reinforced concrete. *Cem Concr Res*. 2004, vol. 34(11), pp. 2159-2167.

46. Horrigmoe G., Sæther I., Antonsen R., Arntsen B. Laboratory investigations of steel bar corrosion in concrete. Background document SB3.10. Sustainable bridges: assessment for future traffic demands and longer lives. A project co-funded by the European Commission within the Sixth Framework Programme, 2007

47. Chung L., Kim Jh.J, Yi S.T. Bond strength prediction for reinforced concrete members with highly corroded reinforcing bars. *Cem Concr Compos.* 2008, vol. 30(7), pp. 603-611.

48. Yalcıner H., Eren O., Serhan S. An experimental study on the bond strength between reinforcement bars and concrete as a function of concrete cover, strength and corrosion level. *Cem Concr Res*. 2012, vol. 42(5), pp. 643-655.

49. Migunov V.N. Ovchinnikov I.G. Dlitel'nye ehksperimental'nye issledovaniya vliyaniya prodol'nykh treshhin v zashhitnom sloe betona na izmenenie dolgovechnosti, kratkovremennoj zhyostkosti i prochnosti vnetsentrenno szhatykh s malym ehkstsentrisitetom stroitel'nykh obychnykh zhelezobetonnykh ehlementov [Long-term experimental studies of the effect of longitudinal cracks in the protective layer of concrete on the change in durability, short-term stiffness and strength of eccentricity of eccentric construction of ordinary conventional reinforced concrete elements]. *Izv. vuzov. Stroitel'stvo* [University Bulletin. Civil Engineering]. 2010, issue 2, pp. 125-130. (Rus.)

ABSTRACTS IN RUSSIAN

Термодинамическая шкала дисперсности кристаллических тел

Ю. В. Левинский[1], М. И. Алымов[1, 2]*

[1] *ФГБУН «Институт структурной макрокинетики и проблем материаловедения им. А. Г. Мержанова РАН», Россия, 142432, г. Черноголовка, Московская область, ул. Академика Осипьяна, д. 8;*
[2] *ФГБУН «Институт металлургии и материаловедения им. А. А. Байкова РАН», Россия, 119334, г. Москва, Ленинский проспект, 49*

* Тел.: +7 496 52 46 376. *E-mail*: alymov@ism.ac.ru

Аннотация

Принято, что основную часть избыточной свободной энергии дисперсной системы составляет ее избыточная свободная поверхностная энергия, а избыточную свободную энергию компактного тела – свободная энергия, определяемая плотностью дислокаций 10^{12} $см^{-2}$. Единицей измерения предлагается считать безразмерный термодинамический критерий дисперсности кристаллических тел D_L. Предложена термодинамическая шкала дисперсности кристаллических тел.

Ключевые слова

Шкала измерения; дисперсность; размер частиц; дефекты; термодинамические свойства; свободная энергия.

Получение титано-хромового карбида из системы $CaCrO_4/TiO_2/Al/C$ методом СВС-металлургии

П. А. Милосердов*, В. А. Горшков, В. И. Юхвид, О. М. Милосердова

[1] *ФГБУН «Институт структурной макрокинетики и проблем материаловедения им. А. Г. Мержанова РАН», Россия, 142432, г. Черноголовка, Московская область, ул. Академика Осипьяна, д. 8*

* Тел.: +7 946 52 46 229. *E-mail*: yu_group@ism.ac.ru

Аннотация

Изучены закономерности горения и автоволнового химического превращения высокоэкзотермических смесей $CaCrO_4/Al/C$ и $CaCrO_4/TiO_2/Al/Ca/C$. Показано, что смесь способна к горению в широком диапазоне содержания в ней углерода, варьирование состава смеси позволило получить литые огнеупорные соединения хрома с различными составом и структурой. Добавление оксида титана привело к снижению температуры горения и, соответственно, отрицательно сказалось на параметрах синтеза и качестве целевого продукта. Высокоэкзотермическая добавка CaO_2 + Al значительно повысила температуру горения смеси и расширила пределы горения и фазоразделения. Получен продукт, состоящий преимущественно из целевой фазы $Ti_{0,8}Cr_{0,2}C$ и включений фаз Cr_2AlC (MAX-фазы) и Cr_7C_3.

Ключевые слова

Хромат кальция; карбиды; литые материалы; синтез горением; СВС-металлургия; титано-хромовый карбид.

Упрочнение взрывом и его применение в производстве крестовин железнодорожных стрелочных переводов

А. А. Дерибас[1], А. А. Штерцер[2]*, Е. Е. Зубков[3]

[1] *ФГБУН «Объединенный институт высоких температур РАН», Россия, 125412, Москва, ул. Ижорская, 13, стр. 2;*
[2] *ФГБУН «Институт гидродинамики им. М. А. Лаврентьева», Сибирское отделение РАН, Россия, 630090, Новосибирск, пр-т акад. Лаврентьева, 15;*
[3] *АО «Новосибирский стрелочный завод», Россия, 630025, Новосибирск, ул. Аксенова, 7*

* Тел: +7 913 901 1678. *E-mail*: asterzer@mail.ru

Аннотация

Рассматриваются особенности упрочнения взрывом (**УВ**), связанные с воздействием ударной волны на металл. Представлены свойства стали Гадфильда после УВ. Показано, что промежуточный слой сухого песка между зарядом взрывчатого вещества и обрабатываемым металлом обеспечивает усиление ударной волны, что дает возможность проводить УВ с использованием порошкообразных взрывчатых веществ с низкой плотностью и скоростью детонации. Дано описание промышленной технологии упрочнения крестовин железнодорожных стрелочных переводов. Показано, что УВ увеличивает срок службы этих изделий на 20–30 %.

Ключевые слова

Упрочнение взрывом; ударная волна; сталь Гадфильда; крестовина железнодорожного стрелочного перевода; твердость.

Разрушение материалов кварцевых световодов при ударно-волновых и лучевых нагрузках

В. П. Ефремов[1]*, А. В. Уткин[1,2]

[1] *ФГБУН «Объединенный институт высоких температур РАН», Россия, 125412, Москва, ул. Ижорская, 13, стр. 2;*
[2] *ФГБУН «Институт проблем химической физики РАН», Россия, 142432, Московская область, г. Черноголовка, пр-т акад. Семенова, 1*

* Тел: +7 495 485 09 63. *E-mail*: dr.efremov@gmail.com

Аннотация

Нарушение световой проводимости световода, транспортирующего интенсивное лазерное излучение, приводит к появлению яркосветящейся лазерной плазмы. Плазма начинает двигаться навстречу излучению, необратимо повреждая световод. В зависимости от интенсивности потока возможны различные скорости распространения повреждения по световодам навстречу излучению – это либо «горение» световодов, либо «оптическая детонация». Оба процесса «горение» и «оптическая детонация» световодов разрушают световую проводимость кварцевых световодов по всей длине. Скорость распространения «горения» зависит от плотности энергии и составляет несколько метров в секунду. Детонационно-подобный режим разрушения распространяется со скоростями несколько километров в секунду. Для моделирования процесса такого разрушения необходимы ударно-волновые данные материалов кварцевых световодов. В данной работе впервые проведено экспериментальное изучение особенностей распространения фронта ударных волн в материалах сердцевины оптических световодов во взрывных экспериментах. Для изучения детонационно-подобного режима распространения лазерного разряда изучали экспериментальные (модельные) световоды, изготовленные в Научном центре волоконной оптики РАН, и промышленный световод связи (одномодовый световод SMF-28e фирмы Corning). В ударно-волновом эксперименте подтвержден двухволновой профиль распространения ударной волны. В материалах световода обнаружена аномальная сжимаемость за фронтом ударной волны. Снижение скорости звука составило около 1 км/с.

Ключевые слова

Лазерно-поддерживаемая детонация; одномодовый световод; лазерная плазма.

Особенности волнообразования при сварке взрывом через тонкий промежуточный слой

Б. С. Злобин, В. В. Киселев, А. А. Штерцер*, А. В. Пластинин

ФГБУН «Институт гидродинамики им. М. А. Лаврентьева», Сибирское отделение РАН,
Россия, 630090, Новосибирск, пр-т акад. Лаврентьева, 15

* Тел.: +7 913 901 1678. *E-mail*: asterzer@mail.ru

Аннотация

В ходе экспериментов по сварке взрывом сталей с низкой пластичностью через тонкий промежуточный слой из пластичного металла обнаружено, что размер волн, возникающих в зоне соединения, может быть различным, даже если условия соударения и соударяющиеся материалы одинаковы. В то же время наблюдаемые значения длин волн λ лежат в диапазоне между λ_{max} и λ_{min}, которые зависят от скорости точки контакта v_c, угла соударения γ, твердостей HV_1, HV_2 и плотностей ρ_1, ρ_2 соударяющихся пластин. Предложены формулы для расчета границ диапазона длин и амплитуд наблюдаемых волн.

Ключевые слова

Сварка взрывом; промежуточный слой; волнообразование; модель Ландау; длина волны; амплитуда волны.

Спарк-плазменное спекание керамических композитов на основе β-сиалона из порошков, полученных методом СВС

К. Л. Смирнов[1]*, Е. Г. Григорьев[1], Е. В. Нефедова[2]

[1] *ФГБУН «Институт структурной макрокинетики и проблем материаловедения им. А. Г. Мержанова РАН»,*
Россия, 142432, г. Черноголовка, Московская область, ул. Академика Осипьяна, д. 8;
[2] *ФГАОУ ВО «Национальный исследовательский ядерный университет «МИФИ»,*
Россия, 115409, Москва, Каширское шоссе, д. 31

* Тел.: +7 496 524 6267. *E-mail*: kosm@ism.ac.ru

Аннотация

Исследовано спарк-плазменное спекание (**СПС**) керамических композитов на основе β-сиалона из порошков, полученных методом СВС: β-Si_5AlON_7, h-BN, β-SiC и TiN. Определены оптимальные условия процесса СПС, обеспечивающие получение керамических композитов с высокой относительной плотностью (более 95 %) и прочностью при изгибе до 400 МПа при содержании от 0 до 30 масс. % h-BN, от 0 до 40 масс. % β-SiC и от 0 до 40 масс. % TiN.

Ключевые слова

Самораспространяющийся высокотемпературный синтез; спарк-плазменное спекание; керамические композиты; сиалон; нитрид бора; нитрид титана; карбид кремния

Синтез керамики на основе пирохлора $Y_2Ti_2O_7$ в режиме СВС

Т. В. Баринова*, В. Ю. Баринов, И. Д. Ковалев, Н. В. Сачкова

ФГБУН «Институт структурной макрокинетики и проблем материаловедения им. А. Г. Мержанова РАН»,
Россия, 142432, г. Черноголовка, Московская область, ул. Академика Осипьяна, д. 8

*Тел: +7 496 52 463 04. *E-mail:* tbarinova@ism.ac.ru

Аннотация

Исследовано влияние добавок Fe и (Al + SiO_2) на режим горения, пористость, фазовый состав и структуру синтезируемых керамических матриц на основе структуры пирохлора состава $Y_2Ti_2O_7$. Показано, что введение порошка Fe не оказывает влияния на фазовый состав керамик. Присутствие алюминия в шихте привело к образованию фаз граната

$Y_3Al_5O_{12}$ и перовскита $YAlO_3$. В присутствии выбранных добавок горение шихтовых заготовок проходило в управляемом стационарном режиме, образцы керамики сохраняли форму и размеры шихтовой заготовки, имели литую структуру, но введенные добавки не способствовали существенному снижению пористости получаемой керамики. Керамики с открытой пористостью менее 10 % получены при приложении осевого усилия в 0,1–0,3 кН на продукт после полного прохождения процесса горения.

Ключевые слова

Самораспространяющийся высокотемпературный синтез; минералоподобные матрицы; пирохлор; высокоактивные отходы.

Базовые модели объемного синтеза композитов на основе титана

А. Г. Князева

ФГБУН «Институт физики прочности и материаловедения Сибирского отделения РАН», Россия, 634055, Томск, пр-т Академический, 2/4;
ФГАОУ ВО «Национальный исследовательский Томский политехнический университет», Россия, 634050, Томск, пр-т Ленина, 30

* Тел: +7 3822 286 831. *E-mail*: anna@ispms.ru

Аннотация

Показаны возможности моделей объемного синтеза с прогнозом конечного состава. Представлены простейшие модели синтеза композитов на основе титана. В моделях учитывается плавление с постепенным образованием жидкой фазы в заданном температурном интервале. Предполагается, что управление процессом осуществляется за счет изменения скорости нагрева и исходного состава смеси. Модели реализованы численно. Продемонстрировано, что конечный фазовый состав во всех ситуациях оказывается неравновесным.

Ключевые слова

Синтез композитов; численное моделирование; детальная кинетика; неравновесный состав.

Твердотельный фазовый переход наноалмаза при нагреве и облучении

В. П. Ефремов, Е. И. Закатилова*

ФГБУН «Объединенный институт высоких температур РАН», Россия, 125412, Москва, ул. Ижорская, 13, стр. 2

* Тел: +7 495 485 09 63. *E-mail*: ei.zakatilova@mail.ru

Аннотация

Проанализированы данные по разрушению монокристалла алмаза и детонационного наноалмаза (**ДНА**) при радиационном облучении. Определена доза облучения, при которой происходит графитизация в монокристалле алмаза. Установлено влияние размера частиц ДНА на характер повреждений при облучении.

Проведено экспериментальное исследование тепловой стабильности детонационных наноалмазов при атмосферном давлении в динамической среде аргона в диапазоне температур от 30 до 1500 °С со скоростью тепловой обработки 2 и 10 °С/мин. Обнаружена высокая стойкость ДНА при температуре выше 1500 °С. Исследование с помощью рентгеноструктурного анализа показало, что твердотельный фазовый переход в ДНА происходит около 1000 °С. Исследование на электронном микроскопе сохраненных образцов показало влияние скорости нагрева на параметры порошка ДНА. Полученные данные по тепловой стабильности рекомендованы для усовершенствования метода ионно-плазменного нанесения покрытия на поверхность стальных деталей.

Ключевые слова

Детонационные наноалмазы; синхронный термический анализ; тепловая стабильность; твердотельный фазовый переход; радиационные повреждения.

Инициирование и горение механоактивированных смесей алюминия и оксида меди

А. Ю. Долгобородов[1–4 *], Б. Д. Янковский[1], В. Г. Кириленко[2], А. Н. Стрелецкий[2,3], С. Ю. Ананьев[1,3], И.В. Колбанев[2], Г. А. Воробьева[2], А. А. Шевченко[2,4]

[1] *ФГБУН «Объединенный институт высоких температур РАН», Россия, 125412, Москва, ул. Ижорская, 13, стр. 2;*
[2] *ФГБУН «Институт химической физики им. Н. Н. Семенова РАН», Россия, 119991, Москва, ул. Косыгина, 4;*
[3] *ФГАОУ ВО «Московский физико-технический институт (государственный университет)», Россия, 141701, Московская обл., г. Долгопрудный, Институтский пер., д. 9*
[4] *ФГАОУ ВО «Национальный исследовательский ядерный университет «МИФИ», Россия, 115409, Москва, Каширское шоссе, д. 31*

* Тел: +7 495 483 22 95. *E-mail*: aldol@ihed.ras.ru

Аннотация

Проведена оптимизация условий механоактивации смеси Al + CuO в целях получения наиболее мощного энерговыделения при химическом взаимодействии компонентов. Для активации смесей использовались вибрационная и планетарная шаровые мельницы. Результаты влияния механоактивации на скорость горения контролировались с помощью высокоскоростной фотосъемки процесса горения пористых образцов (плотность 50 – 30 % от максимальной) в стеклянных трубках диаметром 5,5 мм. Инициирование горения проводилось электроискровым способом с контролируемой амплитудой импульса тока. Определены зависимости периода индукции и скорости распространения фронта горения в зависимости от пористости смесей и амплитуды инициирующего импульса. При низком уровне тока инициирующего импульса наблюдался нестационарный пульсирующий режим горения. Результаты в целом показали преобладающий характер фильтрационного механизма распространения горения в исследованных смесях.

Ключевые слова:

Термитные смеси; механоактивация; скорость горения.

Исследование влияния комплексного модификатора на основе углеродных нанотрубок на процессы структурообразования цементного камня

Ю. Н. Толчков[1*], З. А. Михалева[1], А. Г. Ткачев[1], О. В. Артамонова[2], М. А. Каширин[2], М. С. Ауад[3]

[1] *ФГБОУ ВО «Тамбовский государственный технический университет», Россия, 392000, г. Тамбов, ул. Ленинградская, д. 1;*
[2] *ФГБОУ ВО «Воронежский государственный технический университет», Россия, 394006, г. Воронеж, ул. 20-летия Октября, д. 84;*
[3] *ООО «НаноТехЦентр», Россия, 392000, г. Тамбов, ул. Советская, д. 51*

[*]Тел: +7 915 664 44 88; *E-mail*: Tolschkow@mail.ru

Аннотация

Анализируется влияние углеродных нанотрубок, которые используются в качестве основного компонента модифицирующей комплексной нанодобавки, на кинетику гидратации цемента, фазовый состав и прочностные характеристики цементного камня. Повышение прочностных характеристик цементного камня, модифицированного комплексным наномодификатором, обусловлено ускорением процесса гидратации цемента, формированием оптимальной микроструктуры цементного камня, в котором уже в начальные сроки твердения происходит дополнительное образование низкоосновных гидросиликатов кальция по данным рентгенофазового анализа.

Методом сканирующей электронной микроскопии установлено формирование дополнительно направленной кристаллизации частиц новообразований цементного камня преимущественно с контактами срастания.

Наблюдается ускоренная кинетика набора прочности наномодифицированных образцов, с увеличением предела прочности при сжатии на 20 – 30 % в возрасте 28 суток.

Ключевые слова

Наномодификатор; углеродные нанотрубки; рентгенофазовый анализ; кинетика гидратации цемента; цементный камень .

Обеспечение температурного режима в реакторе для функционализации углеродных нанотрубок

Д. В. Таров*, Т. П. Дьячкова, Е. Н. Туголуков, И. Н. Шубин, В. П. Таров

ФГБОУ ВО «Тамбовский государственный технический университет», Россия, 392000, Тамбов, ул. Советская, д. 106

*Тел: +7 915 660 26 53. *E-mail*: postmaster@kma.tstu.ru

Аннотация

Рассмотрена проблема обеспечения температурного режима в емкостных устройствах, оборудованных мешалкой, для функционализации углеродных нанотрубок с использованием стеарата титана в нанодисперсной жидкой среде с подачей диоксида углерода. Проведен анализ методов смешивания и настройки температурного режима в реакторе. На основе дифференциальных уравнений теплопроводности разработана математическая модель температурного поля течения, движущегося в режиме идеального перемещения через канал постоянного сечения, образованный поверхностями полутрубки и тела. Расчет температурного поля по текущему временно́му интервалу включает в себя множество решений задач теплопроводности с последующим рассмотрением всех компонентов локального теплового баланса. На основании результатов расчетов построены зависимости изменений температуры нанодисперсной среды в емкостном реакторе от времени начала режима и относительной длины полутрубки.

Ключевые слова

Емкостный реактор; корпус; функционализация; углеродные нанотрубки; температурное поле; математическая модель; допущения; нанодисперсная система.

Новый физический способ локализации наномеханического действия управляемых низкочастотным магнитным полем магнитных наночастиц на механочувствительные биохимические системы

Ал. О. Жигачев [1], Ю. И. Головин[1–3]*, Н. Л. Клячко[2,3]

[1] *ФГБОУ ВО «Тамбовский государственный университет им. Г. Р. Державина», 392000, Россия, Тамбов, ул. Интернациональная, 33;*
[2] *ФГБОУ ВО «Московский государственный университет им. М. В. Ломоносова», 119991, Россия, Москва, ГСП-1, Ленинские горы, 1, стр. 3;*
[3] *ФГБОУ ВО «Национальный исследовательский технологический университет «МИСиС», 119991, Россия, Москва, Ленинский просп., 4*

* Тел.: +7 4752 53 26 80. *E-mail*: nano@tsutmb.ru

Аннотация

Магнитные/суперпарамагнитные наночастицы (**МНЧ**), управляемые внешним магнитным полем (**МП**), имеют большой потенциал для различных биомедицинских применений. МНЧ позволяют оказывать селективное наномеханическое действие на уровне отдельных молекул намеченного типа путем их магнитомеханической актуации в низкочастотном МП. Однако введенные в кровоток МНЧ могут аккумулироваться во многих органах, создавая опасность непредвиденных побочных эффектов, которые могут возникнуть при включении активирующего переменного МП. В настоящей работе предложен новый физический метод и технология локализации воздействия МНЧ на биохимическую систему, основанные на создании градиентного локализующего магнитного поля с нулевой точкой вблизи центра магнитной системы. В этих условиях активирующее переменное МП стимулирует только те МНЧ, которые находятся в близкой окрестности нулевой точки. Вдали от нее, где локализующее МП значительно превышает стимулирующее переменное МП, МНЧ оказываются «вморожены» в это поле и не подвержены действию более слабого активирующего переменного МП. Изучены форма и размер области локализации воздействия в зависимости от характеристик локализующего и активирующего МП.

Ключевые слова

Магнитные наночастицы; негреющее низкочастотное магнитное поле; локализация; магнитомеханическое воздействие.

Оценка и моделирование прочности сцепления корродированной арматуры в железобетонных элементах

В. П. Ярцев*, А. Н. Николюкин, Т. М. Плужникова

ФГБОУ ВО «Тамбовский государственный технический университет», Россия, 392032, ул. Мичуринская, д. 112, корп. Д

* Тел.: +7 4752 63 03 80. *E-mail*: kzis@nnn.tstu.ru

Аннотация

Одной из решающих причин потери несущей способности железобетонных конструкций считается нарушение сцепления между арматурой и бетоном в результате структурной деградации (коррозии) металлических элементов. Вследствие этого возникает необходимость в изучении поведения корродированной арматуры в железобетонных элементах. Цель исследования – разработка аналитического описания конечной адгезионной прочности сцепления стержневой арматуры в железобетонных изделиях, подверженных различным уровням коррозии. Методика моделирования основана на искусственных нейронных сетях.

Ключевые слова

Аналитическая модель; прочность сцепления; коррозия; экспериментальная база данных; арматура; бетон; искусственные нейронные сети.

ДЛЯ ЗАМЕТОК